8-21-2017

Diamond Radiator Fabrication, Characterization and Performance for the GlueX Experiment

Brendan Pratt
University of Connecticut - Storrs, bpratt18@gmail.com

Diamond Radiator Fabrication, Characterization and Performance for the GlueX Experiment

Brendan Pratt, PhD

University of Connecticut, 2017

The GlueX Experiment conducted in Newport News, VA requires a 9 GeV beam of linearly polarized photons to access the physics of gluonic excitations. Coherent bremsstrahlung (CB) was chosen as the radiation technique for its high intensity and degree of linear polarization. The CB radiator must be of sufficient crystal quality and have appropriate material properties for operating in a 12 GeV electron beam. Diamond, due to its high Debye temperature, was chosen as the CB radiator. Due to multiple scattering of the electron through the crystal, the central region of the radiator is constrained to a thickness of 20 μm. The overall crystal quality must be high in order to reduce the photon beam emittance for proper collimation of unpolarized photons. To meet this specification, the diamond must not have a whole-crystal rocking curve greater than the electron beam emittance, on the order of 20 μrad. This work describes the development of a novel laser ablation technique for differentially thinning single-crystal CVD diamond plate to meet the strict GlueX requirements. Transmission mode x-ray rocking curve measurements are presented which are used to characterize the diamond radiator lattice structure (mosaic spread) before and after laser ablation. Finally, an analysis of the ρ vector meson decay channel $\gamma p \to \pi^+\pi^- p$ is discussed and used to extract the product of the beam asymmetry and polarization of the photon beam as well as spin-density matrix elements (SDMEs) in the helicity reference frame. The observables measured from this analysis are strongly correlated to the performance of the diamond radiator used to produce the linearly polarized photon beam.

Diamond Radiator Fabrication, Characterization and Performance for the GlueX Experiment

Brendan Pratt

B.A., University of Connecticut, 2008

M.S., University of Connecticut, 2013

A Dissertation

Submitted in Partial Fulfillment of the

Requirements for the Degree of

Doctor of Philosophy

at the

University of Connecticut

2017

2017

APPROVAL PAGE

Doctor of Philosophy Dissertation

Diamond Radiator Fabrication, Characterization and Performance for the GlueX Experiment

Presented by

Brendan Pratt, B.A., M.S.

Major Advisor _____

Richard Jones

Associate Advisor _____

Thomas Blum

Associate Advisor _____

Andrew Puckett

University of Connecticut

2017

DEDICATION

I dedicate this dissertation to my family. My parents, Catherine and Daniel, are the foundation upon which my life stands. My mom was the first person to suggest I apply to grad school and I would not be writing this if not for her belief in me. To my brothers, Justin and Jared, whose support and encouragement kept me grounded. To James O'Brien, Matt Neubelt, Alex Barnes, Liana Hotte and Fridah Mokaya, my friends who kept my head above water. To Julie and Keith for raising a wonderful daughter and embracing me into their family. To my wife, Maddie, the single most important thing to come out of my time at UConn; I love you and could not have done this without you. Finally, I dedicate this dissertation to Japhy Ryder Pratt.

ACKNOWLEDGMENTS

I would not say that any part of this degree was particularly easy. If you told me at the age of 20 that I would be completing a PhD. program in physics I would have laughed and told you, "I'm not the graduate student type." And yet, here I am: a product of hard work and a network of supportive and caring people who helped me along the way. I would like to express my profound gratitude for these individuals.

What is a grad student without their research group? My lab mates, Igor Senderovich, Tolga Altinoluk, Zhiewei Zhang, Zhihai Zhu, Alex Barnes, Jim McIntyre and Fridah Mokaya, have all helped me in their own way. All the countless "quick questions" and "can I see how you did that?" added up to not only a collaboration, but to lasting friendships. I would also like to thank the entire GlueX collaboration that impacted my growth as a physicist.

Dr. Jones – our fearless leader – has been my mentor in the field of physics. From spending weekends in the lab together to getting this thesis written, he has been a model of hard work and persistence. I know all that I have learned from him will carry me far beyond graduate school.

I would also like to thank the faculty and staff of the University of Connecticut's physics department. Dr. Dave Perry and Alan Chasse kept me grounded, infusing practical know-how with a splash of much needed humor that cannot be learned in a classroom. Special thanks to Dr. Barry Wells who was kind enough to share his lab space with my 30 year-old laser and me; this project would not have gotten off the ground without him. Finally, I would like to thank Dr. Edward Eyler for donating the original excimer laser to our research group. Although it caused me many headaches, the initial work I was able to accomplish with this laser got me into grad school.

TABLE OF CONTENTS

CHAPTER PAGE

LIST OF FIGURES

LIST OF TABLES

TABLE PAGE

CHAPTER 1

Introduction

1.1 Introduction

Protons were once believed to be elementary particles. Early elastic scattering measurements of the proton form-factor revealed internal structure [1]. The proton is categorized as a hadron which is a composite particle comprising of quarks held together by the strong force. There are two families of hadrons, those particles containing three quarks (baryons) and the lighter particles containing only two (mesons). Further measurements made during the 1960s mapped the spectrum of these light hadronic states and led to the development of the quark model. Within this framework, bound states of a quark and anti-quark ($q\bar{q}$) form a meson and bound states of three quarks (qqq) are called baryons. It was later discovered that these quarks are, in fact, dynamical objects, which led to the development of quantum chromodynamics (QCD).

QCD was modeled after the very successful theory of quantum electrodynamics (QED) to describe the interactions between quarks and gluons. Similar to how charged particles interact via photon exchange, quarks, with their three color charges, interact via gluon exchange. The gluons themselves carry color charge and can interact with quarks and each other, which is very different from the chargeless photon of QED. This gives rise to the possibility of bound states of quarks and gluons, or gluons alone, to exist. Not only are the standard mesonic and baryonic states possible, but others known as gg or ggg (glueballs), gluonic excitations $q\bar{q}$g (hybrid mesons), $q\bar{q}q\bar{q}$ (tetraquarks) and $qqqq\bar{q}$ (pentaquarks) should exist as well. Hybrids mesons are the combination of quark model ($q\bar{q}$) with an excitation of the gluonic field, which can be represented schematically as $qq\bar{q}$. Another interesting experimental fact of QCD is that quarks and gluons do not exist themselves as free particles. This stems from the requirement that only color singlet combinations exist as free particles

in nature, such as $q\bar{q}$ or qqq states. These new states are very interesting because this is the only case of a theory where the gauge particle can play the role of a constituent.

The GlueX experiment was designed and constructed to search for hybrid mesons and is discussed in more detail in a later section. This document presents experimental work in light-meson spectroscopy with the GlueX experiment and describes my particular contribution to this work. The following sections provide the relevant theoretical background and context for the experimental work described in the chapters to follow.

1.2 Theoretical Background

1.2.1 The Constituent Quark Model

The Quark Model was the first successful model for the classification of the large number of particles discovered beginning in the 1950s. It described the observed mesons as bound states of fermionic hadron constituents called quarks (q) and anti-quarks ($\bar{q}$). The early version of the quark model initially included the up (u) and down (d) quarks but was eventually expanded after the discovery of heavy and long-lived hadrons to include the strange (s), charm (c), bottom (b), and top (t) quarks. Quarks were also classified in terms of their electric charge, with u,c,t having charge $+2/3e$ and d,s,b having charge $-1/3e$. Aside from electric charge, the quarks also carry color charge which comes in three varieties: red, blue, green and their anti-colors: anti-red (cyan), anti-green (magenta), and anti-blue (yellow).

As stated previously, the confining property of the strong force within the quark model restricts hadrons to be comprised of quarks and anti-quarks which form color-neutral objects. A possible combination includes a three-quark state (baryons) one of each color (red, green, blue) or one of each anti-color (cyan, magenta, yellow). A second combination involves a two quark state which is a quark-anti-quark pair with color cancellation by color-anti-color (i.e. red:cyan, green:magenta, blue:yellow).

Quark-model mesons ($q\bar{q}$) have a set of rules for allowed values of J^{PC} for a fermion-anti-fermion bound state where J is the total momentum, P is parity and C is charge conjugation. As fermions, each quark has spin 1/2 which can be aligned parallel (S = 1) or anti-parallel (S = 0) to each other with relative orbital angular momentum (L). The total angular momentum of the meson is given by $\vec{J} = \vec{L} + \vec{S}$. Parity for a fermion-antifermion state of good orbital angular momentum L is $P = (-1)^{L+1}$ and charge conjugation $C = (-1)^{L+S}$. Using these rules, the low-lying nonet with $\vec{L} = 0$ and $\vec{S} = 0$ leads to a $J^{PC} = 0^{-+}$. This nonet is called the pseudoscalar nonet, and includes the π, K, η, and η' mesons. Having $\vec{L} = 0$ and $\vec{S} = 1$ leads to $J^{PC} = 1^{--}$ which are called the vector mesons and includes the ρ, K^*, ω and ϕ mesons. The combination $\vec{L} = \vec{S} = 1$ creates three nonets: scalar ($J^{PC} = 0^{++}$), axial vector ($J^{PC} = 1^{++}$) and tensor ($J^{PC} = 2^{++}$).

Any non-quark-model state, regardless of quantum numbers, is considered an exotic state. The low-lying glueballs posses J^{PC} numbers that are the same as $q\bar{q}$ and are difficult to identify due to mixing with conventional meson states. It can be seen that the J^{PC} rules lead to a set of forbidden combinations which are not allowed for $q\bar{q}$ systems including $J^{PC} = 0^{--}$, 0^{+-}, 1^{-+}, 2^{+-}, ... These *exotic hybrid mesons* have non-quark-model quantum numbers, and so they must either have additional $q\bar{q}$ pairs in their wavefunction, or else additional constituent gluons must be incorporated into the wave function to make the quantum numbers add up. Combinations such as these are referred to as *smoking gun* exotics. The fact that these forbidden combinations were not initially observed was a good sign for the quark model. If however, a meson with these quantum numbers were to be observed, it would clearly indicate that there are non-$q\bar{q}$ degrees of freedom within the meson. Experimental hints pointing to the existence of hybrid mesons are described in the following section.

1.2.2 Gluonic Excitations and Confinement

The strong force between quarks, as described by QCD, changes as the distance between them increases. At short distances, quarks are in the regime of asymptotic freedom where perturbative techniques are applicable and describe experimental observations. As the distance between quarks grows, the system enters the confinement regime where perturbation techniques cannot be used. Instead, only non-perturbative lattice QCD calculations or QCD-inspired models can be looked to by experiment for guidance.

QCD is different from QED due to the gluons (the force carrier) carrying color charge whereas in QED the force carriers (photons) are electrically neutral. This phenomenon is illustrated in Fig. 1.1 and shows how the force between two electrically charged particles is proportional to the inverse squared of the distance between them. Between the quark and an anti-quark, however, the color field lines do not fill all of space, and remain constant as the distance increases [2]. These *flux tubes* have an associated potential which is linear with distance and it would take infinite energy to separate the quarks to infinity.

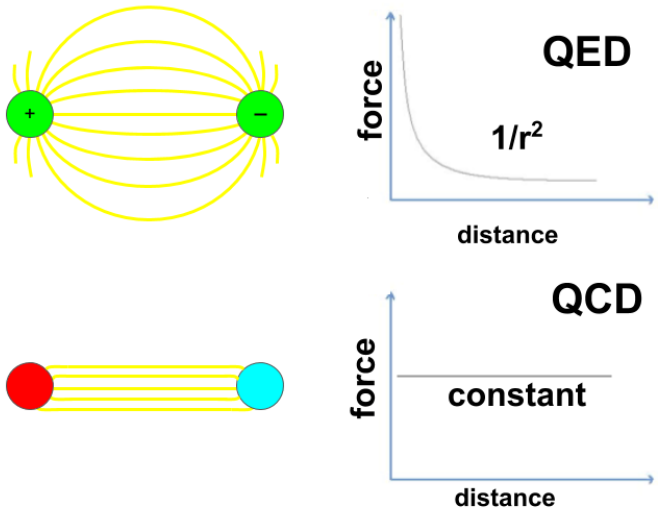

Figure 1.1: Top: The electric field lines between two electric charges and the corresponding dependence of electric force on the distance between the charges. Bottom: The color field lines between two quarks and the corresponding dependence of force on distance (bottom).

Lattice QCD calculations support the concept of flux tube formation between quarks and anti-quarks when the distance between them is on the order of 1 fm or greater [3]. One such calculation is shown in Fig. 1.2 and details the energy density of the color field between a quark and an anti-quark separated by a distance of 1.2 fm. The peaks correspond to the positions of the quarks. The same figure also shows the corresponding potential between the quarks as a function of their separation. It can be seen that, at small distances, the ground state has a potential which follows the expected $1/r$ dependence from 1-gluon exchange, but rises linearly at distances beyond 1 fm. The idea of flux tubes was first introduced by Yoichiro Nambu in the 1970's to explain the observed linear relationship between mass-squared and angular momentum for states belonging to a single Regge trajectory [4]. Y. Nambu showed that the linear dependence could be derived from a simple model of a meson as a relativistic string with fixed mass per unit length, terminated at either end by a massless quark and-quark. This picture describes conventional mesons as a quark anti-quark pair with the flux tube in its ground state. Hybrid mesons (mesons which have both quark and gluonic degrees of freedom) arise when the flux tube is excited, undergoing oscillations transverse to the quark anti-quark axis. In this picture, the flux tube is excited to two degenerate states as it spins clockwise or counter-clockwise around the $q\bar{q}$ line.

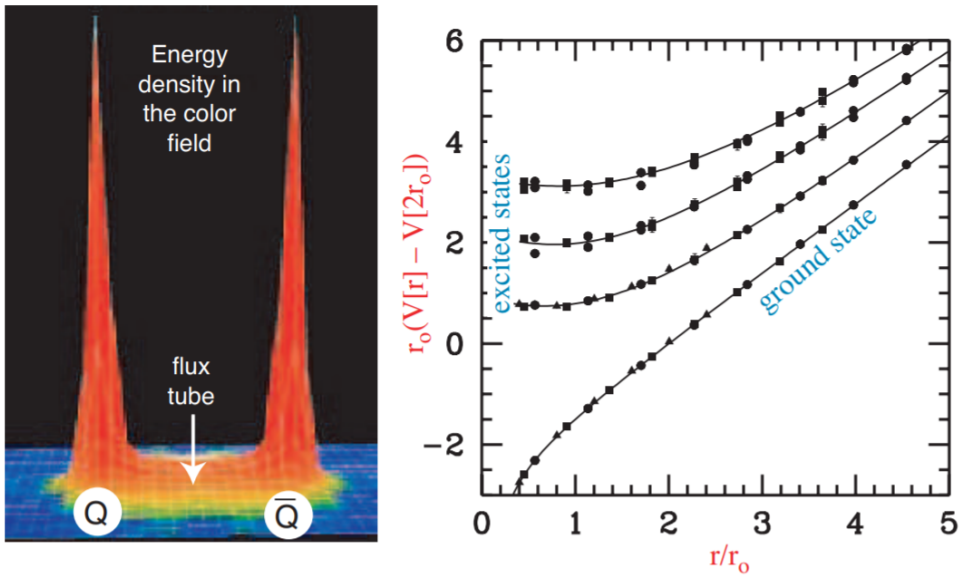

Figure 1.2: Left:The energy density in the color field between a quark and an anti-quark as calculated by lattice QCD. The peaks in energy are at the quark-antiquark positions. This calculation is for heavy quarks in the quenched approximation. Right: The corresponding potential between the quarks and the ground state potential has a 1/r dependence at small distances and is linear for large distances.

Both lattice QCD and flux tube models are consistent with $J = 1$ being the lowest-lying excitation of the flux tube [5] [6] [7]. Linear combinations of the clockwise or counter-clockwise rotations are parity and charge-conjugation eigenstates which lead to two possible excitations for the flux tube: $J^{PC} = 1^{-+}$ or $J^{PC} = 1^{+-}$. If a state with the quark-antiquark pair in configuration $S = L = 0$ ($J^{PC} = 0^{-+}$) is combined with the excited flux tube's $J^{PC} = 1^{-+}$ or $J^{PC} = 1^{+-}$, the result is a hybrid meson with $J^{PC} = 1^{++}$ or $J^{PC} = 1^{--}$. These quantum numbers are allowed by the quark model. However, a $q\bar{q}$ in the $S = 1$ and $L = 0$ configuration ($J^{PC} = 1^{--}$) the resulting hybrid meson can have $J^{PC} = [0, 1, 2]^{+-}$ for the flux tube with $J^{PC} = 1^{-+}$ and $J^{PC} = [0, 1, 2]^{-+}$ for the flux tube with $J^{PC} = 1^{+-}$. Only three of the six possible combinations are in fact exotic: $J^{PC} = 0^{+-}$, $J^{PC} = 1^{-+}$ and $J^{PC} = 2^{+-}$. These will not mix with the $q\bar{q}$ and therefore will have a unique signature that can be measured. We call this the *smoking gun signature* for the *exotic hybrid mesons*. Other higher-order QCD hypotheses are possible for mesonic states with exotic quantum numbers,

such as tetraquarks and molecules. Resolving this ambiguity requires the study of the mass orderings and decay systematics of the states.

The production of mesons happens when an incoming probe interacts with the target particle where one possible result of the scattering can be the excitation of the flux tube. Using a $q\bar{q}$ probe in $L = 0$ and $S = 0$, for example a π or K, production of exotic hybrids are not favored as shown by the previous example. However, if the $q\bar{q}$ has $L = 0$ and $S = 1$ such as a vector meson, several exotic hybrids are expected to be produced at a mass of about 2 GeV/c^2. This mass scale arises naturally if we expect the mass difference between the conventional mesons (ground state mesons) and hybrid mesons to be given by the level spacing between the ground state of the flux tube and the first excited transverse mode. This difference is given by π/r where r is the quark separation.

1.2.3 Photoproduction of Exotic Hybrids

This section explains the fundamental reasoning and requirements for a photon beam to effectively produce the *smoking gun* signature for gluonic excitations. It is helpful to compare the effectiveness of the π, K probe to that of a photon. The π, K probe is a $q\bar{q}$ meson with spins anti-aligned, that is $S = 0$. The photon, on the other hand, can be viewed within the vector dominance model as a virtual $q\bar{q}$ with spins aligned, $S = 1$. In each case, the relative orbital angular momentum is equal to zero ($L = 0$) and the flux tube connecting the quarks is in its ground state. The two different approaches are illustrated in Fig. 1.3, the left being the π probe and the right the photon probe. If the probe scatters and results in an excitation of the flux tube, one expects exotic hybrid mesons to be suppressed in the π-induced interactions relative to those produced by a photon beam of comparable energy.

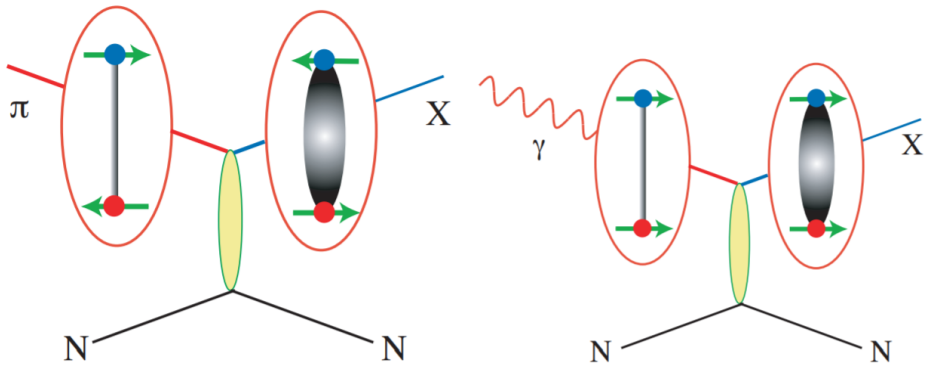

Figure 1.3: Left: Using a π probe the incoming quarks have $L = 0$ and $S = 0$, resulting in excited flux tubes and hybrid mesons X with non-exotic quantum numbers. Right: Using a photon probe the incoming quarks have $L = 0$ and $S = 1$, which results in the possibility of producing hybrid mesons with exotic quantum numbers.

1.2.4 Why Linearly Polarized Photons?

There are three essential reasons for using linearly polarized photons for production of exotic hybrid mesons. Linearly polarized photons can provide information about the spin of the mesons they produce. For example, consider the photoproduction of a vector meson which decays into two pseudoscalar mesons, such as $\rho \to \pi\pi$. Suppose the production mechanism produces the vector with the same helicity as the incident photon. The wave function in the rest frame of the two-pseudoscalars ($\pi\pi$) is described by

$$Y_1^m(\theta, \phi) \propto \sin\theta \cdot e^{im\phi} \tag{1.1}$$

Recall the relationship between linear and circular polarization. A left-handed-circularly polarized photon ($|L\rangle$) has quantum number $m = -1$ and a right-handed-circularly polarized photon ($|R\rangle$) has $m = 1$. They are related to the linearly polarized states, $|x\rangle$ (in the production plane) and $|y\rangle$ (perpendicular to the plane of production) by:

$$|x\rangle = \frac{1}{\sqrt{2}}(|L\rangle + |R\rangle) \tag{1.2}$$

$$|y\rangle = \frac{i}{\sqrt{2}}(|L\rangle - |R\rangle) \tag{1.3}$$

Also recall that states of linear polarization are eigenstates of parity. So, for circularly polarized photons ($m = 1$ or $m = -1$), the square of the amplitude in Eq. 1.1 carries no ϕ information while, for in-plane photons, there is a $\cos^2\phi$ dependence and, for out-of-plane a $\sin^2\phi$ dependence in the decay angular distribution.

Another very important reason for using linearly polarized photons for the production of exotic hybrid mesons is the utility of linear polarization for separating natural and unnatural parity exchange processes. This is best illustrated using a specific example, consider a vector particle ($J^P = 1^-$) which was produced by the exchange of a scalar particle ($J^P = 0^+$ -natural parity exchange) or a pseudoscalar particle ($J^P = 0^-$ -unnatural parity exchange). The goal is to determine whether the vector is produced by natural (amplitude A_N) or unnatural (amplitude A_U) parity exchange. In the center-of-mass of the vector particle, the momentum vectors of the beam photon and exchange particle are collinear. For circularly polarized photons, the value of m of the vector is the same as that of the photon. The orbital angular momentum between the photon and exchange particle is $L = 0$ or $L = 2$ for natural parity exchange and $L = 1$ for unnatural parity exchange via parity conservation. Simple addition of angular momenta states that circularly polarized photons having a $m = +1$, means the total amplitude is $A_N + A_U$ whereas for $m = -1$ the total amplitude is $A_N - A_U$. Using circularly polarized photons only the sum or the difference of the two exchange amplitudes can only be measured and not the individual components. Using linearly polarized photons along the x-direction, we can extract A_N using Eq. 1.2 and similarly for polarization along the y-direction, A_U is extracted using Eq. 1.3.

A final example will be given to demonstrate how linearly polarized photons can be used to filter exotics. Consider the example of a ρ, π system with $I = 1$ has $C = +$ (where I is isospin and C is charge-conjugation). Suppose one can determine that the productions is dominated by a single exchange particle of a given naturality, perhaps by selecting a limited range in $|t|$ where this exchange dominates. A produced $C = +$ particle with spin one can have natural parity ($J^{PC} = 1^{-+}$ - exotic) or unnatural parity ($J^{PC} = 1^{++}$ - non-exotic). For

the case of natural parity exchange the in-plane polarization selects the $J^{PC} = 1^{-+}$ wave while out-of-plane polarization selects $J^{PC} = 1^{++}$. The reverse is true for unnatural parity. In this situation, the linear polarization is used to select the naturality of the produced particle after specifying the naturality of the exchange particle. In the previous example, the naturality of the produced particle was specified and the linear polarization was used to select the naturality of the exchanged particle.

1.3 Photon Beam

1.3.1 Coherent Bremsstrahlung

The photon source used in the GlueX experiment must be capable of energy at least 80% of the 12 GeV electron beam and have a high degree of linear polarization at intensities up to $10^8\gamma/s$. The energy resolution for individual photons in the beam should be as high as possible, which means it should be on the order of the electron beam energy spread. Ideally, the photon source would also keep low energy photon contamination to a minimum and require a minimum of down-time for maintenance. Coherent bremsstrahlung (CB) was chosen as the method of producing photons of the highest possible energy, flux and degree of linear polarization from electrons of $12GeV$.

In the coherent bremsstrahlung (CB) process, ultra-relativistic electrons scatter from a crystal oriented such that their momentum transfer ($\mathbf{q}$) to the crystal matches a reciprocal lattice vector. Rather than a single atom absorbing the entire momentum $\mathbf{q}$, the entire crystal lattice recoils coherently in the scattering process, so that zero energy is transferred with the momentum to the electron [8].

In order to satisfy the coherence condition, the recoiling crystal must remain in its internal ground state; if any phonons are created in the process then the coherence is destroyed. For this reason, no matter how perfect the crystal, there is always some admixture of coherent and incoherent production happening in any physical situation. In contrast to the ordinary

(incoherent) bremsstrahlung process, coherent bremsstrahlung is linearly polarized [8], and is concentrated in narrow regions of the continuum energy spectrum. The black line shown in Fig. 1.4 shows the CB spectrum as a function of the photon beam energy.

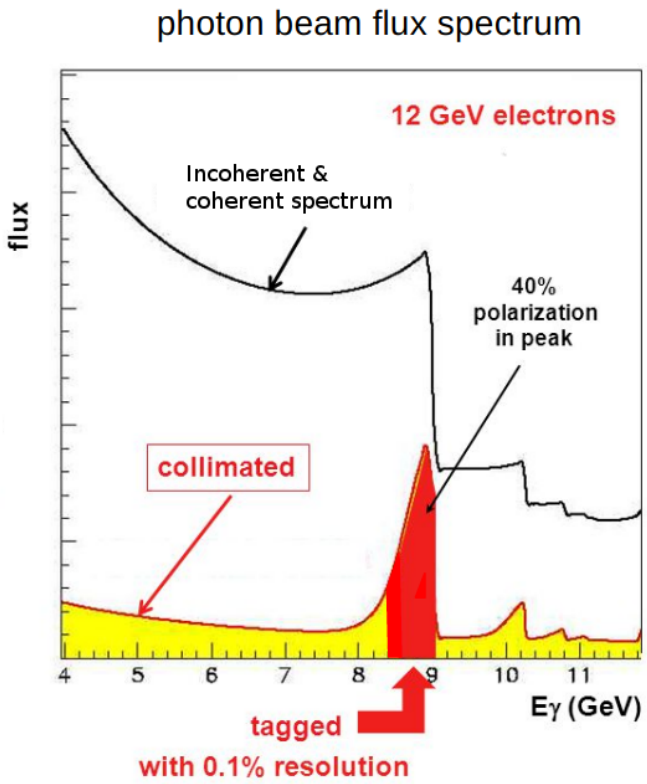

Figure 1.4: Bremsstrahlung spectrum before and after collimation. The sharp peak around 9 GeV is from the coherent enhancement.

This is very useful for nuclear experiments because, with collimation, a nearly monochromatic high energy photon beam can be generated, and linear polarization is provided as a bonus. The kinematics of bremsstrahlung confines most of the intensity of the photon beam to forward angles within m/E radians of the incident electron direction and is true for both incoherent and coherent components. However, a peak in the coherent component corresponding to a single reciprocal lattice vector has two-body kinematics and there is a well-defined relation between the emission angle and the energy of the photon emitted in the lab. Emission angles of 0° yields photons with maximum energy, with energy decreasing with increasing angle. This explains the shape of the coherent peaks as seen in Fig. 1.4,

the sharp right-hand edge corresponding to 0° emission angle and the tail to lower energies corresponding to emission at higher angles.

The incoherent component has essentially no correlation between photon energy and emission angle. This is due to the fact that it comes from a sum over momentum transfers at all angles. This means that collimating away all photons beyond some angle $\theta_{max} < m/E$ uniformly attenuates the incoherent energies, preserving all of the coherent photons from the maximum energy for the given peak down to some cutoff. The size of the virtual spot at the collimator is determined by the emittance of the electron beam combined with an upper limit of 20 μrad on the angular spread of the beam at the radiator. The value 20 μrad was chosen to match the spread in the beam incidence angle to the mosaic spread of the CB radiator because it is the combination of the two that limits the definition of the coherent peak [9]. The author's primary focus was the development of these crystal CB radiators.

1.3.2 Choice of Radiator

The coherent process relies on having well separated **q** values in reciprocal lattice space and a low probability for phonon production in the recoil crystal. These impose stringent limits on the choice of target, favoring targets with high symmetry and a high Debye temperature. A high Debye temperature is important for three main reasons. The first is because the cross section for CB from a discrete crystal momentum vector **q** contains a factor $e^{-q^2/4M\theta_D}$. This factor reflects the diminishing effect of position fluctuations of atoms in the crystal lattice on CB. For large Debye temperature θ_D, this factor is near unity for the low-order crystal momenta. Also, the Debye temperature of a crystal is, roughly speaking, a measure of the stability of the crystal structure and its ability to survive significant radiation doses. Finally, the crystal will be heated by the incident electron beam and will be normally operating in vacuum well above the ambient temperature. A high Debye temperature means that the crystal can operate over a large range of temperatures without degrading in performance as a radiator [9].

Diamond turns out to have the highest Debye temperature of any simple crystal, nearly 2200 K. It also has well isolated reciprocal lattice vectors at low order, and has a low atomic number which locates the peak in the atomic form factor very close to the lowest order **q** vector. Not only this, but diamond is also the material with the highest thermal conductivity and radiation hardness, which makes it ideal for use as a target in an intense electron beam. For all of these reasons, diamond is the unique material of choice for a CB target. By changing the orientation of the crystal, the energy of the CB enhancements in the photon spectrum can be shifted around, so that the maximum photon flux is achieved at the desired energy. The GlueX experiment requires the photon source be capable of producing photons with 75% of the electron beam energy (12 GeV) and having an average polarization of 40%.

1.3.3 Crystal Thickness

Due to multiple scattering of the electron beam as it passes through the radiator, there is an upper limit for the thickness of a crystal radiator. This effect causes the divergence of the electron beam to grow, meaning the photon beam spot size at the collimator face is enlarged thereby degrading the degree to which collimation attenuates the incoherent component over the coherent part. On the other hand, the crystal must have some minimum thickness so that it can achieve the full coherent gain. It turns out that in the coherent bremsstrahlung process, for a 12 GeV beam energy and a 6 GeV coherent photon, the coherence length is only 18 nm, or about 50 unit cells for diamond [9]. The coherence length then imposes no practical limit on how thin the diamond radiator should be.

To understand the effects from multiple scattering, it is best to show the calculated spectra for various radiator thicknesses [9]. Fig. 1.5 shows the photon spectrum generated using two different radiator thicknesses, one at 10^{-4} radiation lengths and the second 10^{-3} radiation lengths. The 10^{-3} is scaled down by a factor of 10 to aid in the comparison. It is assumed in the calculation that there is a 3.4 mm collimator 80 m downstream of the radiator. Loss in normalized intensity and broadening of the left edge of the peak is due

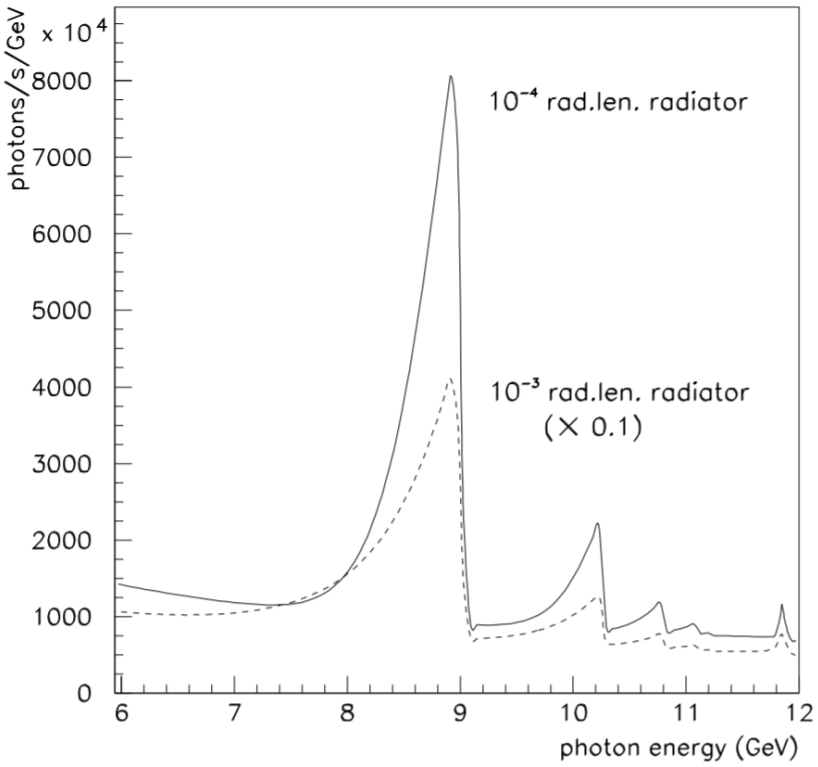

Figure 1.5: The energy spectrum for a collimated coherent bremsstrahlung source from a 1μmA electron beam at 12 GeV using two different thickness diamond radiators. A 3.4 mm collimator is assumed to be located 80 m from the radiator and typical values for beam emittance and crystal quality are also assumed.

to the enlarging of the photon beam spot on the collimator face from multiple scattering of the electron beam in the crystal prior to radiation. A 10^{-4} diamond radiator is 15 μm thick. The second constraint for the diamond radiators for the GlueX experiment is that these crystal be of thickness between 10 μm and 20 μm.

The author's primary contribution to the GlueX experiment was in the development and characterization of the diamond radiators used to produce the 9 GeV coherent bremsstrahlung photon source. The following sections describe GlueX's experimental setting and the work involved in creating these radiators within the GlueX requirements outlined above.

1.4 The GlueX Experiment

GlueX is a photonuclear experiment currently running at the Thomas Jefferson National Laboratory in Newport News, Virginia. The experiment's goal is to search for mesons with gluonic excitations using a beam of linearly polarized photons with energies between 8.4 and 9.0 GeV. These photons are produced when 12 GeV electrons from the CEBAF (shown in Fig. 1.6) pass through a thin monocrystalline diamond target called a radiator.

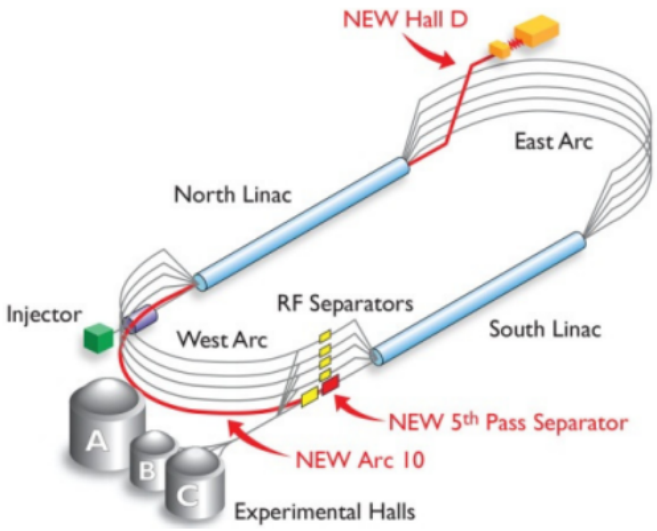

Figure 1.6: Continuous electron beam accelerator facility (CEBAF) at the Thomas Jeffereson National Laboratory and the newly constructed experimental Hall D.

1.5 Tagging Spectrometers

Emerging from the radiator, the photon beam continues downstream where it is collimated before entering the experimental hall (Hall D) and is incident on a liquid hydrogen target within the GlueX spectrometer as shown in Fig. 1.12. Back at the radiator, the electrons used to create the photon beam pass afterwards through a large dipole magnet which deflects the main beam into a beam dump. Those electrons which radiated a significant portion of their energy into a hard photon bend with a smaller radius in the dipole field and exit the magnet early, where they pass into an array of scintillation detectors that measure their time

and position with high accuracy. Their placement with respect to the dipole magnet can be seen in Fig. 1.7.

Through the precise knowledge of the dipole field, the momentum of the post-bremsstrahlung electrons is inferred from their position at the exit edge of the magnet to high precision. These detectors vary in their momentum range and resolution. A large array of coarse-grained counters called the Tagger Hodoscope measures electrons over the range 3.0 - 11.8 GeV with full width at half maximum (FWHM) resolution that varies between 15 and 30 MeV.

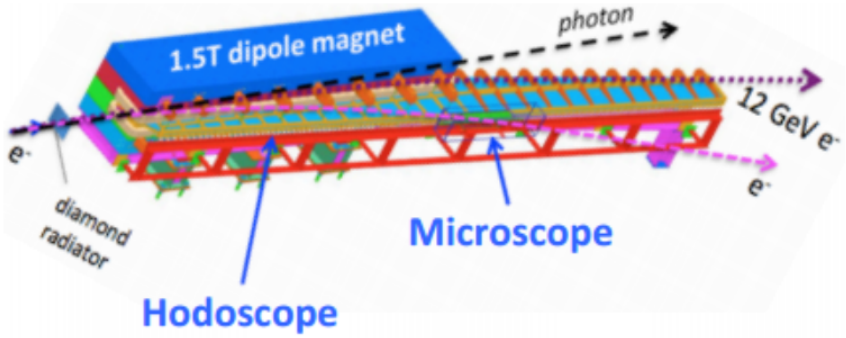

Figure 1.7: Illustration of tagger hodoscope (TAGH) and tagger microscope (TAGM).

Around the region of the primary coherent peak, the Tagger Microscope covers an energy range of 8.4 - 9.0 GeV with a finer resolution of 10 MeV FWHM [9]. The energy of the beam minus the energy of the recoil electron gives the energy of its correlated photon via energy conservation. In its temporal structure, the beam is divided into narrow buckets a few ps long, separated by 4 ns. The tagger scintillators identify which beam buckets contain a photon within the narrow energy window subtended by that scintillator. This technique using timing to determine the energy of photons one by one in a broadband photon beam is known as photon tagging. A top down view of the post-bremsstrahlung electron trajectory and relative position of the tagger microscope is depicted in Fig. 1.8.

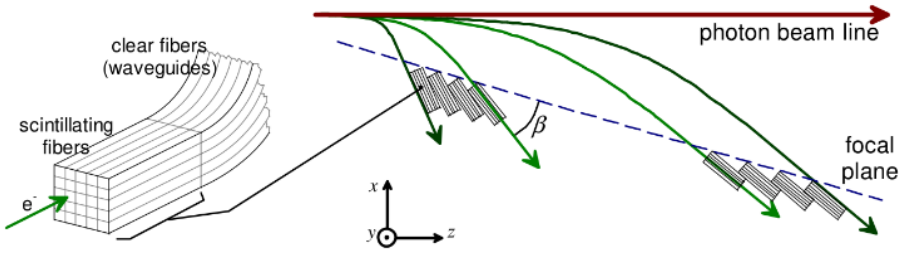

Figure 1.8: Diagram of the geometry of the scattered electron trajectories in the tagger magnet, and their passage through the scintillators in the tagger microscope.

1.5.1 Collimation

Even with diamond as a radiator, without any collimation the CB photon beam is at best a 40:60 mixture of coherent:incoherent components. However, the coherent component is concentrated at lower momentum transfer relative to the electron beam than the incoherent. Narrow collimation can be used to reduce the incoherent flux in the beam to a negligible level. The effect of this collimation can be seen in Fig. 1.4 as an enhancement in the CB spectrum. The GlueX beamline incorporates a collimator with an aperture of only 1.7 mm radius at a distance 76 m from the radiator, a half-angle of only 22 μrad. In order for such a narrow collimation to be effective, the divergence of the electron beam back at the radiator must be much less than this. Fortunately, the CEBAF electron beam has a very small emittance at 12 GeV, less than 5 mm.μrad, leading to a divergence angle $\theta_0 < 10$ μrad at the radiator. Prior to radiating a photon, the incident electron traverses on average half the thickness of the radiator, and in so doing, its divergence increases due to multiple scattering in the material. Imposing the condition that the net divergence at the point of radiation not exceed $\sqrt{2}$ of its value prior to entry to the crystal, this leads to the requirement that the radiator can be no thicker than 20 μm.

The position of the electron beam is controlled by the CEBAF operators who can steer the beam up until the diamond radiator. An active collimator was installed just before the primary tungsten collimator to sample the position of the photon beam just before it

enters the experimental hall. The active collimator is constructed of eight tungsten wedges, each machined to have a series of needle-like columns protruding from a solid base. Both horizontal and vertical axis have four of these wedges, two inner and two outer, symmetrically positioned about the aperture. A misaligned photon beam incident on one of the wedges creates a shower of knock-on electrons, the signal from which is amplified and analyzed to reconstruct the position of the beam relative to the center. This position feedback loop aids the CEBAF operators to position the electron beam on the radiator such that the resulting photon beam is correctly centered on the narrow collimator. An exploded CAD rendering of the active collimator can be seen in Fig. 1.9.

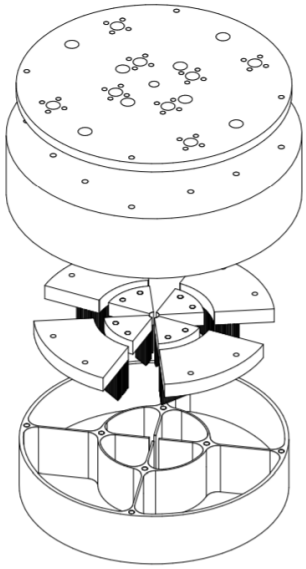

Figure 1.9: CAD rendering of active collimator.

1.5.2 Triplet Polarimeter

After the beam has exited the collimator it passes through a detector called the triplet polarimeter (TPOL) which is used to measure the photon polarization. A depiction of the triplet polarimeter can be seen in Fig. 1.10. The detector works via triplet photoproduction ($\gamma\ e^- \rightarrow e^-\ e^+\ e^-$) when photons incident on a beryllium foil interact with an electron in

the target to produce an e^+ e^- pair via pair production which continue down stream in the forward direction. The recoil electron is detected by the triplet polarimeter, comprised of an $S3$, double-sided silicon strip detector with 32 azimuthal sectors on the ohmic side and 24 concentric rings on the junction side shown in Fig. 1.10b. The TPOL has 768 resolvable angular regions which are used to measure the azimuthal distribution of the recoil electron [10]. The polarization of the photon beam is determined by fitting the angular distribution of the recoil electron measured by the TPOL and extracting polarization as one of the fit parameters. Polarized photons have a total cross section (σ) which follows Eq.

$$\sigma = \sigma_0[1 + P\Sigma \cos 2\phi] \tag{1.4}$$

where σ_0 is the cross section of the unpolarized photons, P is the photon polarization and Σ is the beam asymmetry [10]. A similar approach will be discussed in a later chapter for extracting beam asymmetry values via the angular distribution of the $\gamma p \to \pi^+\pi^- p$ decay.

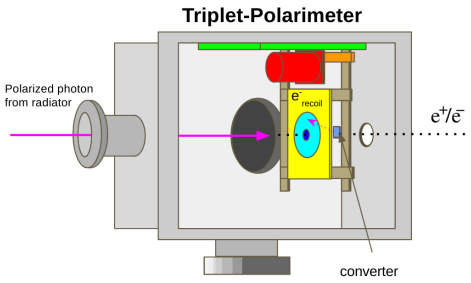

(a) 1.10a

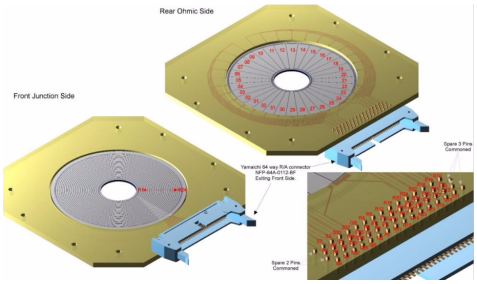

(b) 1.10b

Figure 1.10: Left: Illustration of the triplet polarimeter and photon beam path. Right: Rendering of the S3 silicon strip detector used to measure the angle of the recoil electron.

1.5.3 Pair Spectrometer

The total beam intensity is measured by a detector called the pair spectrometer (PS) which is positioned after the TPOL. The e^- e^+ pair created from the TPOL converter continue and travel into a 1.8 T dipole magnet. The magnet bends and separates the paths of the two oppositely charged particles, projecting them onto a hodoscope which is divided into

fine and coarse counters as shown in Fig. 1.11. The fine counters are comprised of 145 scintillator/wave-length shifting fibers which couple to silicon photomultipliers (SiPMs) and measure the exact timing and energy information of the incident e^- or e^+. The coarse component of the PS is made up of 16 scintillating counters coupled to photomultiplier tubes, positioned symmetrically on either side of the beam axis. The PS was constructed to measure photon beam energies between the 6.0 and 12.5 GeV with a resolution of about 30 MeV.

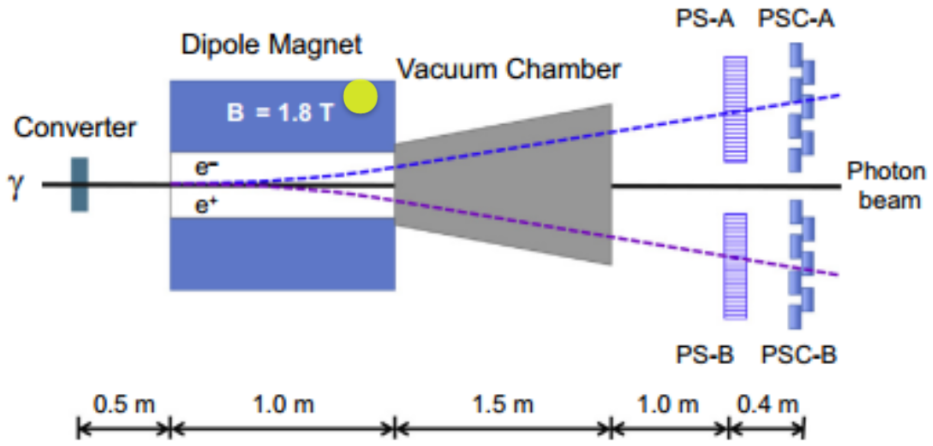

Figure 1.11: Illustration of the Pair Spectrometer

1.6 The GlueX Detector

The collimated CB photon beam enters Hall D where it reaches its final destination, a 30 cm long liquid hydrogen target, roughly 2.4 cm in diameter, liquid hydrogen target surrounded by the GlueX spectrometer as seen in Fig. 1.12. Immediately surrounding the target is the Start Counter (SC) which is comprised of 30 scintillating fiber strips oriented parallel to the beam axis, which are the first detector elements to see particles coming from beam interactions in the target, and form a principle component of the experimental trigger. Together with several other detector subsystems, the target and SC are installed within a 2.2 T solenoid magnet which produces the high magnetic field needed to measure charged particle momentum and

suppresses low energy electromagnetic background created by the photon beam interactions in the target.

Forward charged particles and the forward moving gammas emitted at angles below roughly 10° are tracked by the Forward Drift Chambers (FDC) and Forward Calorimeter (FCAL) respectively. Particles and gammas created at larger angles are measured by the Central Drift Chamber (CDC) and the Barrel Calorimeter (BCAL). The timing of the forward particles is measured by the Time-of-Flight (TOF) detector and aids in particle identification (PID). There are plans for installing a FDIRC (forward detection of internally reflected Cherenkov) detector in the future to increase the ability to perform PID. Each of these components will be described in greater detail in the following sections.

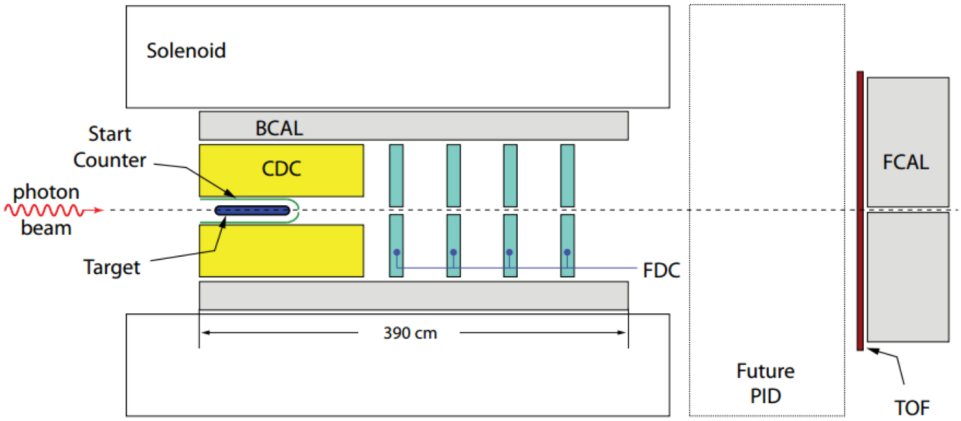

Figure 1.12: Cross section of the GlueX Spectrometer detailing the position of each subdetector.

1.6.1 Start Counter

Charged particles leaving the liquid hydrogen (LH2) target are first detected as they pass through one of the 30 scintillating paddles of the SC, depicted in Fig. 1.13. The scintillation produced from a charged particle travels the length of the light guide and is measured by SiPMs. Each paddle is coupled to four SiPMs, the signals from which are summed. The SC

has nearly 4π coverage for particles that originate inside the target and can detect particles at a net rate of 10^8 γ/s.

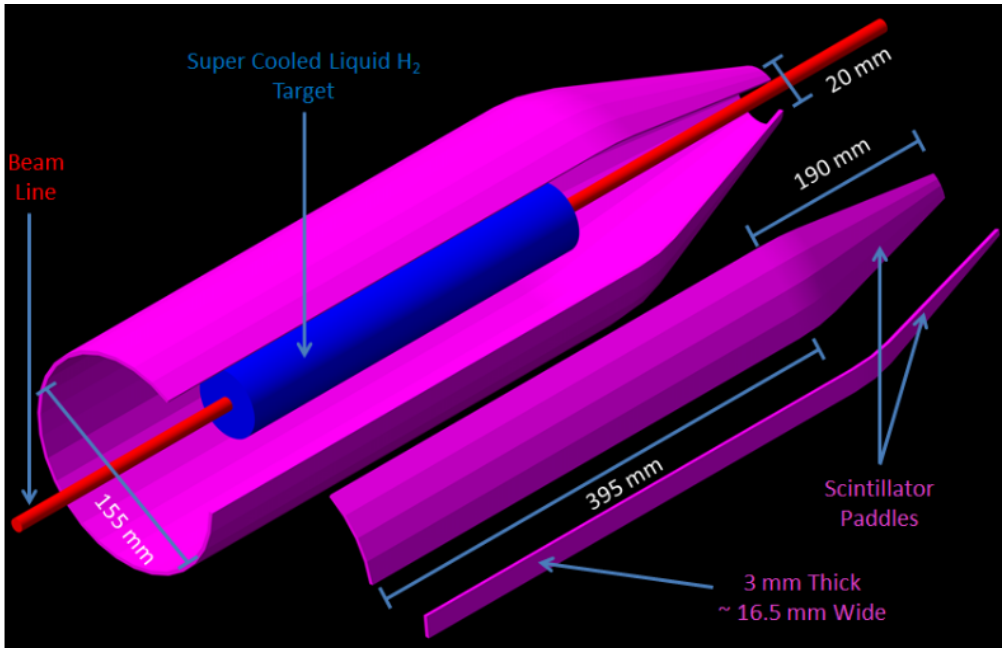

Figure 1.13: Rendering of the Start Counter and the liquid hydrogen target it surrounds.

1.6.2 Tracking

Charged particles exiting the LH2 target are bent by the large solenoid's magnetic field. These particles travel along helical paths whose axis is parallel to the magnetic field and whose radius varies with the particle momentum. Particles with $\theta > 10°$ (where θ is the polar angle and the incident beam direction is the z axis) pass through the CDC which is constructed from straw tubes [11]. Each tube is filled with a gas mixture and has a wire on its central axis held at high voltage running the length of the tube. Inside the tube a uniform electric field is created between the anode wire (having a diameter of 20 μm) and the inner wall of the tube, which functions as a cathode. As the particle travels through a tube, it ionizes the gas medium, creating free electrons which drift toward the positive high-voltage wire. The charge is then measured and a "hit" event is recorded.

The CDC is constructed with a total of twenty-eight layers of these tubes as shown in Fig. 1.14, twelve running axially along the direction of the beam path, eight mounted with a twist angle +6° and eight twisted in the opposite direction at -6° [11]. As the particle passes through the CDC, it hits straws in each of these axial and stereo layers and the coordinates of the track can be reconstructed at many points along the track with a resolution of 150 μm radial and 1.5 mm axial. The CDC also measures a particle's rate of ionization energy loss per distance traveled, known as dE/dx. Comparison of the track momentum, measured by the curvature in the magnetic field, with its velocity measured using dE/dx, yields a measure of the mass of the particle that produced the track. This measurement is particularly useful for tracks at large angles and low momentum which leave tracks in the CDC without hitting the BCAL.

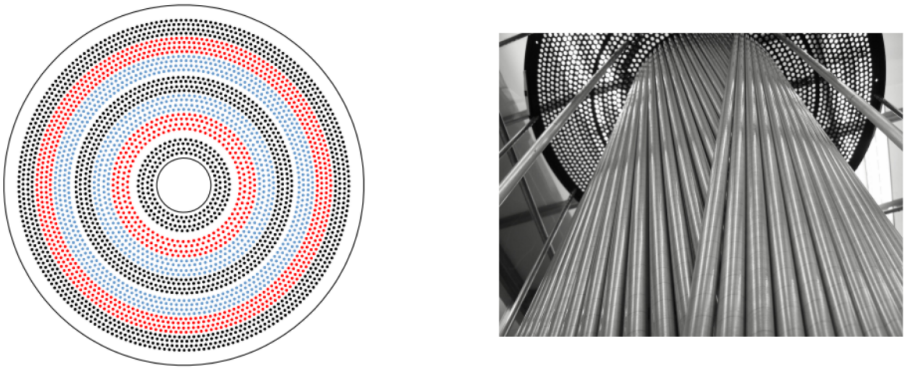

Figure 1.14: Left: Diagram of the Central Drift Chamber layering scheme. Tubes in black are running axially, tubes in red are at an angle of +6° and tubes in blue are at an angle of -6°. Right: Picture of the alternating CDC straw orientations in two adjacent stereo layers.

Particles traveling in the forward direction are tracked by four forward drift chamber (FDC) packages each containing six cells positioned transverse to the beam axis as shown in Fig. 1.15. The operating principle of the FDC is similar to the CDC in that a series of anode (sense and field wires) and cathodes are contained in a mixture of argon and CO_2 gas and utilize ionization drift for signal generation and position measurement. Each cell contains a single layer of wires sandwiched between a U cathode strip and a V cathode strip which are skewed at an angle of ±15° as shown in Fig. 1.16. By alternating the angles of U and V

strips, unique identification of each particle's crossing point. The FDC is used to measure (x, y) position of forward charged particles and dE/dx information with a resolution of 250 μm.

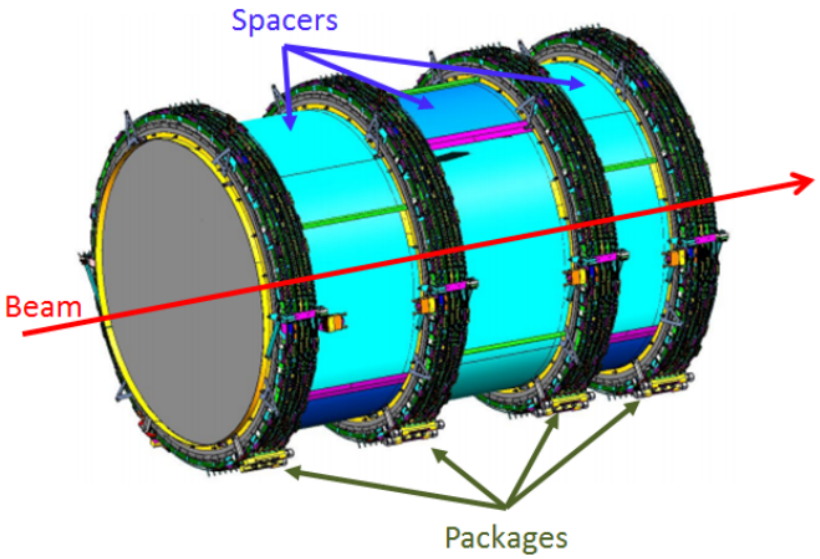

Figure 1.15: Rendering of the Forward Drift Chamber.

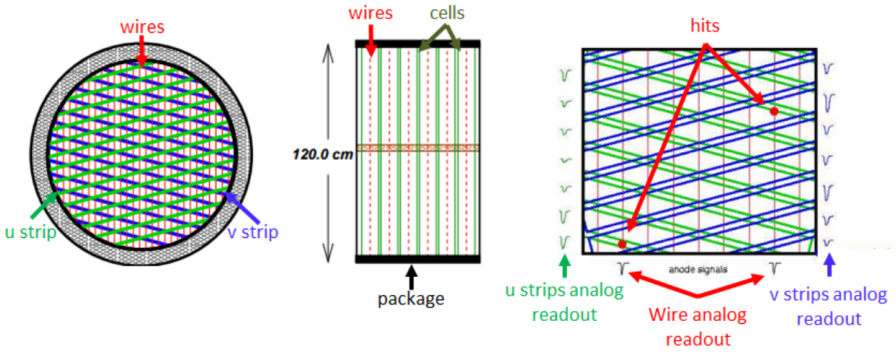

Figure 1.16: Cell wiring of the FDC. The U and V cathode strips are angled at +75° and 75° from the vertical wire.

1.6.3 Calorimetry

Particle energy is measured by the Barrel Calorimeter (BCAL) and the Forward Calorimeter (FCAL). The BCAL wraps around the CDC and FDC as shown in 1.12 and measures particles produced at angles between $11° < \theta < 126°$ as shown in Fig. 1.17a. The BCAL is subdivided into 48 azimuthal modules which have alternating layers of lead and scintillating fibers running axially along the beam path [12]. The particles which pass through the BCAL interact with the lead, creating showers which then pass through the scintillating material creating light signals which are read out at the two ends of the module by SiPMs. The BCAL has an energy resolution (σ_E/E) of 5.4% $\sqrt{E} \oplus$ 2.3%, a position resolution (σ_z) of $1.1mm/\sqrt{E}$ and time difference resolution ($\sigma_{\Delta t/2}$) of $70ps/\sqrt{E}$.

Outside of the solenoid magnet, the FCAL measures forward moving particles which emitting from the target at an angle $\theta < 11°$. The detector is built with $28004 \times 4 \times 45cm^3$ $F8-00$ lead glass blocks stacked in a circular array with each module coupled to a 12 stage FEU 84-3 PMTs and a custom built IU Cockcroft-Walton bases. The FCAL works by the same electromagnetic showering process as the BCAL, except that the light emitted by energetic charged particles in lead glass is due to the Cherenkov effect instead of scintillation. The FCAL has an energy resolution (σ_E/E) of 5.6% $\sqrt{E} \oplus$ 3.5%, a position resolution of $6.4mm/\sqrt{E}$ and time resolution (σ_t) of approximately 0.4 ns for 100 mV.

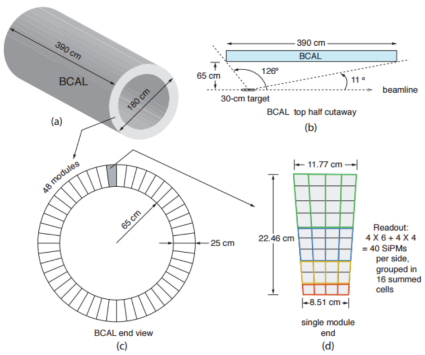

(a) 1.14a

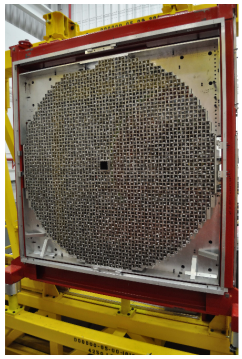

(b) 1.14b

Figure 1.17: Left: View of the BCAL and sub components. Right:Image of the FCAL.

1.7 Particle Identification

The Time of Flight (TOF) detector is located 550 cm downstream of the LH2 target center, just before the FCAL as shown in Fig. 1.12. It consists of an array of 2.54 cm thick, 6 cm wide scintillating paddles, coupled to 30 cm long light guides. Signals generated from charged particles passing through the scintillating paddles are read out by a series of PMTs. The TOF covers an area of $252 \times 252 cm^2$ and has a $12 \times 12 cm^2$ central hole which allows the photon beam to continue through the FCAL to the beam dump [13]. The TOF is divided into two planes of 84 paddles orthogonal to the beam axis, one that runs in the vertical direction. Hits in the TOP provide charged track multiplicity and time of flight information with respect to the track start time from the SC. The TOF provides PID information by measuring the velocity of charged particles. Its geometrical design allows for the measurement of particles which have a polar angle of $1^\circ < \theta < 11^\circ$.

There are future plans to install a FDIRC (forward detection of internally reflected Cherenkov) detector in the space between the FDC and the TOF. The FDIRC will greatly enhance GlueX's ability to perform PID and reduce experimental backgrounds. The detector will be constructed from 48 synthetic quartz blocks [14] taken from the decommissioned DIRC detector used in the BaBar experiment and can be seen in Fig. 1.18b.

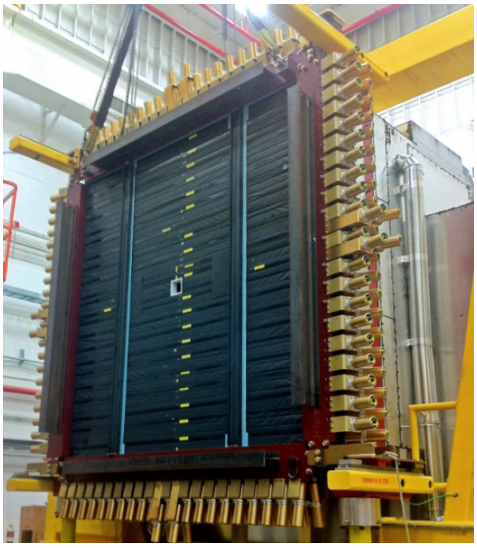

(a) Time of Flight

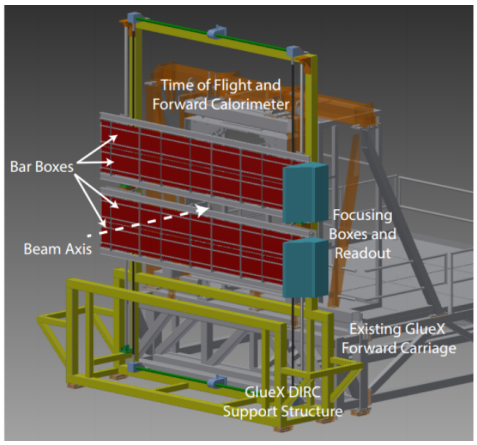

(b) FDIRC

Figure 1.18: Left:Time of Flight (TOF). Right: FDIRC (forward detection of internally reflected Cherenkov.

CHAPTER 2

Diamond Radiator Fabrication

Current techniques for thinning large-area diamond monocrystals to thicknesses of 20 μm are limited. One promising technique employs a chemically assisted lapping process which coats micron-sized grit particles with a special etching chemical to soften the diamond surface and remove atomic layers a few at a time [15]. While this technique works without the high pressures used in traditional diamond-grit polishing that can cause deep damage to the crystal, it is very slow (1-2 hours per micron) and only works if one is willing to accept a uniform thickness over the entire target surface. Using this method to thin a diamond from an initial thickness of 500 microns would take weeks of continuous grinding, and at the end of the process there are significant risks of cracking the crystal either while lapping the ultra-thin diamond or removing it from the lapping plate. Our research group pursued this approach in collaboration with a commercial firm with expertise in this area and were able to produce a small number of thin diamonds, one as thin as 10 microns. However, another problem with these samples was discovered when their crystal properties were studied using X-ray diffraction.

The one property of the diamond crystal that is essential to its function as a coherent radiator is that it be a uniform single crystal, free of mosaic structure. Defects such as dislocations and vacancies exist in any crystal, but if their density is low enough they do not disrupt the long-range order of the crystal. However, when the crystal is made very thin, the stress that builds up around them can relieve itself by physically bending and warping the crystal. To the electron beam, this behaves just like a mosaic structure in the crystal. As discussed previously, the requirement for GlueX is that the mosaic spread across the face of the entire diamond crystal must be less than 20 μrad.

X-ray rocking curves (discussed in a later section) taken at the Cornell High Energy Synchrotron Source (CHESS) revealed that all of the diamonds from any source that our group had available for study, whatever the milling process used to thin them, suffered from

severe bending/warping if it was less than about 50 microns in thickness [16]. The conclusion from these studies was that residual defects within the diamond structure, however few and far between, are sufficient to warp the diamond plate from its regular planar geometry as soon as the thickness is reduced below about 50 microns. The only way to avoid this and achieve the 20 μrad specification was to keep the thickness larger than 50 microns. A research group at Brookhaven National Laboratory (BNL) published results using a focused high-power UV laser to mill diamond via a process known as ablation [17]. Lasers with wavelengths above the band gap of diamond (213 nm) can excite electrons between the diamond carbon atoms from a bound state to an ionized state [17]. The top 100 nm of the diamond surface at the focal spot is instantly vaporized, emitting a plume of carbon-based plasma normal to the surface of the diamond crystal. By scanning the diamond across the focal spot, a sequence of overlapping spots is built up that results in uniformly milling the sample surface. The short duration (10 ns) and short absorption length (50 nm) of the laser pulse ensure that the pulse energy is absorbed in the upper 100 nm of the diamond and does not result in deep energy deposition in the bulk of the crystal. Most importantly, this technique allows the diamond to be thinned differentially, creating a central window of 20 μm thickness while retaining the full thickness around the edges for stiffness and support. This would never be possible with an abrasive technique.

The laser ablation technique on diamond was developed extensively here at UConn by the author, using a Lambda Physik EMG 101 excimer laser operating at a wavelength of 193 nm as the light source. An xyz computer-controlled stage was constructed to sweep the diamond (under a vacuum of roughly 600 mtorr) across the laser focus. The bulk diamond crystal before machining was typically of size 7.1 x 7.1 x 0.250 mm^3. A series of laser pulses was applied to a rectangular region in the center of the diamond, milling a thin window down to the required thickness and leaving untouched a zone around the perimeter which is called the *frame*. Tests of these framed targets at CHESS have shown that they can meet the 20 μrad requirement on the mosaic spread in the central region.

After the diamonds have been ablated, they must be installed in the GlueX Tagger Hall at JLab. The author has designed and machined a mounting system to hold the diamonds in the goniometer used to orient the crystals in the electron beam. The design and construction of the diamond ablation facility at the University of Connecticut, the x-ray characterization of target samples and initial measurements of the CB photon beamline have been the author's primary contribution to the GlueX experiment, and is the primary focus of this thesis. The components of the experimental setup shown in Figure 2.1 are discussed in detail in the sections below.

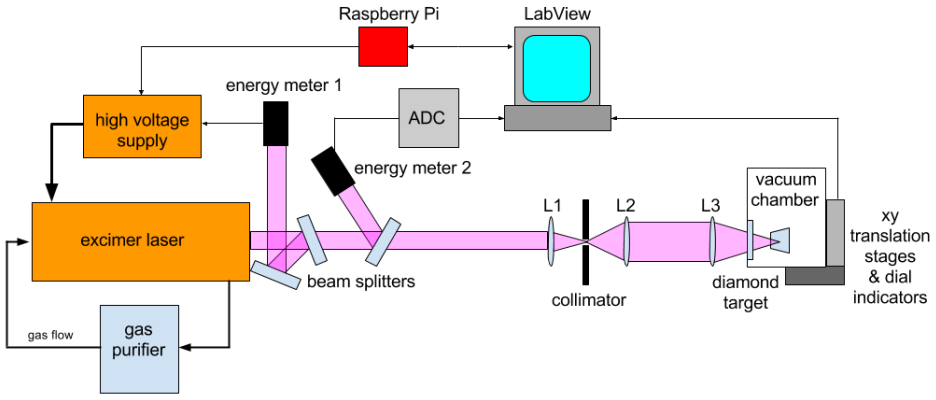

Figure 2.1: Illustration of the UConn setup used to ablate diamond.

2.0.1 Excimer Laser

A Lambda Physik EMG 101 argon fluorine (ArF) excimer laser with an operating wavelength of 193 nm was used to ablate single-crystal CVD diamond. The laser was capable of delivering 120 mJ per pulse at a maximum repetition rate of 50 Hz with pulse duration of 20 nanoseconds. The transverse intensity profile of the beam was an asymmetrical flat top Gaussian with horizontal FWHM of 22 mm and vertical FWHM of 6 mm.

Excimer lasers produce UV light via the spontaneous/stimulated emission from an excited complex comprised of a halogen and noble element in the presence of a buffer element (fluorine, argon and helium respectively). These pseudo-molecules are created inside the

laser cavity by large electric fields and live for only a short period of time before photo-emission occurs creating the desired laser pulse [18] [19]. Afterwards, the halogen and noble gases undergo a refractory period during which they cannot be re-excited. The internal mechanics of the Lambda Physik EMG 101 excimer laser provides a continuous flow of fresh lasing medium into the laser cavity via a circulating fan. Figure 2.2 depicts the cross section of a typical excimer laser and illustrates the path of the laser gas medium.

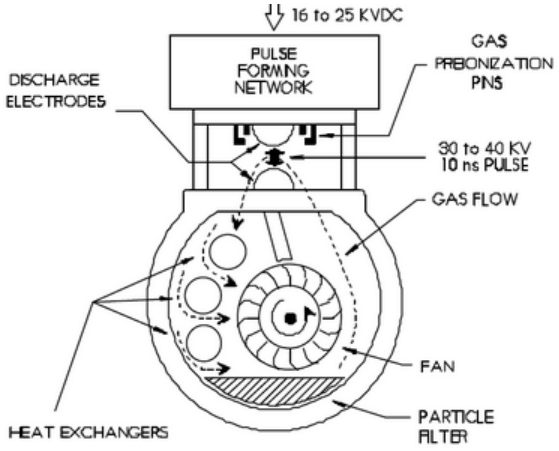

Figure 2.2: An illustration depicting the internals of a typical excimer laser.

As shown, after the laser gas undergoes emission it passes over a series of heat exchangers. At repetition rates greater than 3 Hz a cooling unit must be switched on which passes 30° C water through these heat exchangers. Once the hot gas is cooled it passes through particulate filters and is sent back into the laser tube to begin the cycle again. As this process continues the halogen component of the lasing medium reacts with the non-passivated metal released by the discharge of the laser cavity's pre-ionization pins and other containments within the laser cavity. This contamination of the halogen gas reduces the average pulse energy of the laser until no lasing occurs and the gas mixture must be completely replaced. For the purposes of laser ablating diamond, the laser gas medium was replaced when the average pulse energy dropped below 50 mJ.

Lambda Physik specified that this model laser was capable of firing 400,000 pulses on a single fill of the gas mixture before the pulse power drops to 50% of its maximum value.

Assuming the laser starts at a maximum power of 120 mJ the laser would produce 480,000 pulses before it reached the minimum pulse energy of 50 mJ and had to be refilled. A $7.2 \times 7.2 \times 0.25$ mm^3 diamond thinned with a central region of dimensions $6.7 \times 6.7 \times 0.02$ mm^3 would require approximately 4.5×10^5 pulses per single complete pass over the diamond (assuming 0.5 $\frac{mm}{s}$ motor speed in x direction, 50 Hz laser repetition rate, and 0.01 mm motor step in y axis between sweeps in x). An average cut depth of 38 μm per complete pass would require a total of over 2.6 x 10^6 pulses to reach the final depth of 20 μm, roughly 7 complete laser gas fills.

The ablation setup has methods to compensate for fluctuations in average laser energy so that the diamond surface remains smooth to within $\pm$ 0.5 μm (these methods will be discussed in detail in a later section). However, even with these corrections, allowing the average laser energy to vary by 50% over the course of a single pass results in non-uniform ablation across the diamond which is too great to compensate for. It was desirable to extend the lifetime of the laser gas medium so that average power remains constant over at least a single pass. Ideally, the laser would have a gas life time which exceeds the total number of pulses required to bring the diamond sample to 20 μm.

An Oxford $GP-2000$ cryogenic gas purification system and Millipore particulate filter were installed in a closed loop with the laser cavity as shown in Figure 2.1. The gas purifier system pumps the laser gas medium through a liquid nitrogen cold trap removing contaminments generated during the lasing process, extending the laser gas life time by over an order of magnitude. The plot below shows the average pulse energy as a function of pulses, after the gas purifier and particulate filter were installed.

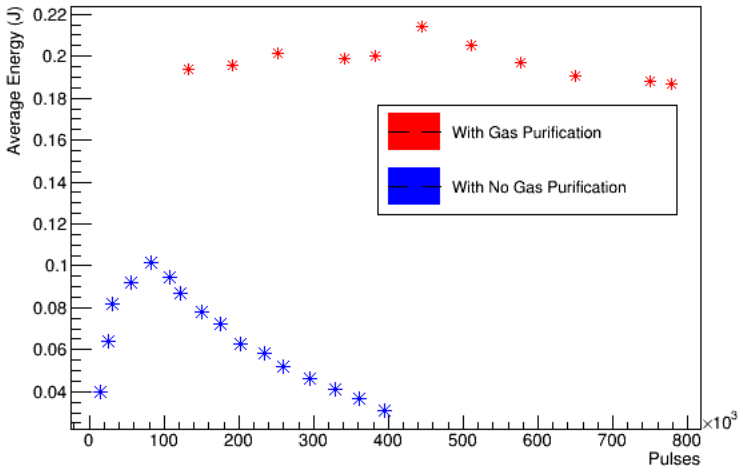

Figure 2.3: Average laser pulse energy measured as a function of total pulses fired.

Figure 2.3 shows the comparison between running the laser with (red) and without (blue) the gas purification system. Using the gas purifier in line with the laser cavity resulted in an order of magnitude increase in number of total pulses per gas refill. Also, the average output energy of the laser increased significantly due to filtration of halogen spoiling containments inside the laser cavity. In some cases only a single fill was required to ablate a diamond from start to finish, greatly reducing the surface variation on the diamond radiator and the cost of running the machine. Without the use of the gas purification system it would not have been possible to produce viable radiators for GlueX with any kind of repeatable procedure using this setup.

2.0.2 Laser Beamline

Figure 2.1 illustrates the arrangement of the ablation setup. A series of quartz plates are positioned next to the beam exit port of the laser so that a small sample of the beam (<5%) is reflected onto two separate energy meters labeled energy meter 1 and energy meter 2. Energy meter 1 is part of the laser's on board energy feedback system which is used to

control the output energy and stabilize the pulse-to-pulse variation to within 5%. Energy meter 2 measures each laser pulse incident on the diamond target during the ablation process.

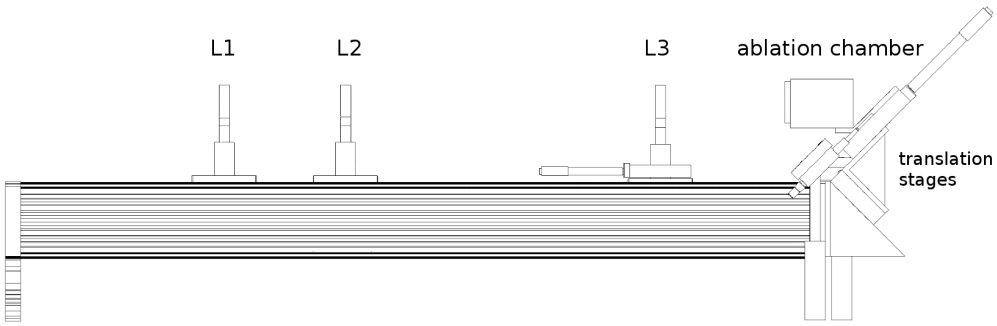

Figure 2.4: Scaled illustration of laser ablation beam line including lenses L1, L2 and L3

The laser beam then passes through a series of lenses as shown in Figure 2.4. Lenses L1 and L2 are positioned with overlapping focal spots so that the output of L2 is a highly parallel, expanded beam. This was to remove large non-Gaussian tails from the beam transverse intensity distribution.

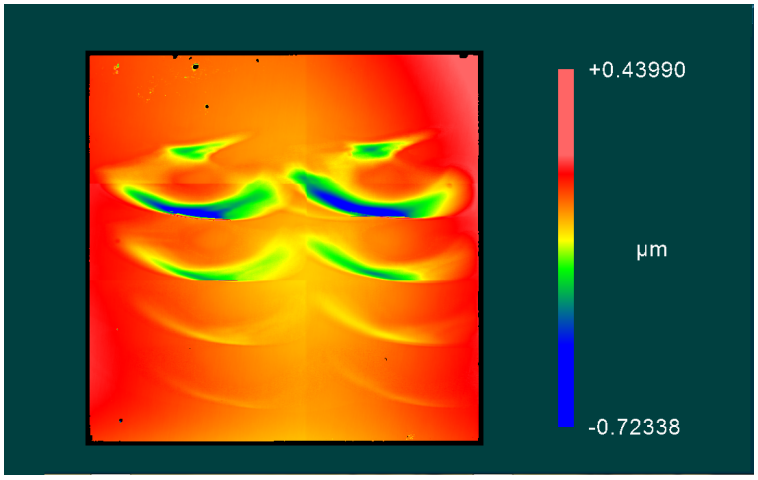

(a) 2.5a

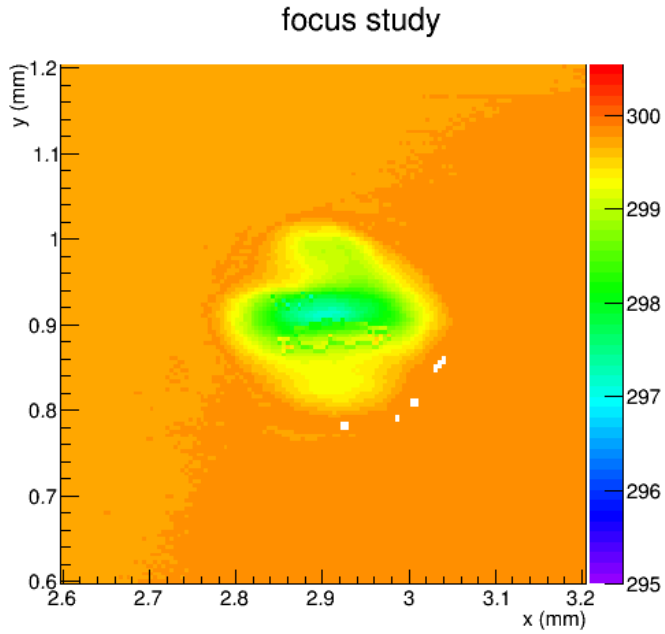

(b) 2.5b

Figure 2.5: Zygo interferometer images taken of diamond surface ablated with a sequence of a few pulses without (left - 8 spots) and with (right - 1 spot) the beam expansion optics.

Figure 2.5a shows two columns of broad asymetric patterns in a diamond sample cut before the beam expander (lens L1 + L2) were added to the setup, for a varying number of laser pulses. Notice the significant distortion of the profile imprinted on the diamond surface in the diamond after ablation. If the focal spot that created these patterns was rastered over an entire diamond it would result in a radiator with large surface variations rendering it unusable for GlueX. The focus of the laser defines the cutting tool with which the diamond is shaped. An ill-defined focus will ablate non-uniformly as the diamond is rastered across it, making it extremely difficult to cut uniformly to 20 μm thickness without cracking the thin diamond membrane. The geometry of the focus also determines the fluence (laser energy per cm^2) incident on the diamond surface. A tightly focused beam spot increases the available fluence, therefore increasing the rate of ablation. It is therefore very important to include the beam expander in the optics. With this in place, the next step was to measure the waist of the beam after L3 in the three lens system.

The final focusing lens (L3) is mounted on a translation stage which has a maximum travel of 12mm and minimal achievable incremental movement of 0.10 μm. Adjusting L3 changes the focal position of the lens thereby changing the total fluence on the diamond. This greatly affects both the cutting rate and surface structure left after rastering over the diamond. A beam spot that is too large will not have enough energy per square centimeter to ablate the diamond surface. However, a beam spot too small will require many more steps in the vertical axis to cover the entire diamond. A beam spot with dimensions close to the minimal incremental movement of the translation stages may introduce surface variation (eq. horizontal ridges) as the beam is rastered over the diamond.

Mapping the Laser Focus

Knowledge of the focal shape created from the optical configuration described above was critical for achieving control over the rate of ablation and the overall surface roughness of the ablated diamond. The focal length of L3 was mapped using a gold-tungsten (gt)

wire harp scan in both the vertical and horizontal axis. Two mounts were machined from aluminum as shown below in Figure 2.6.

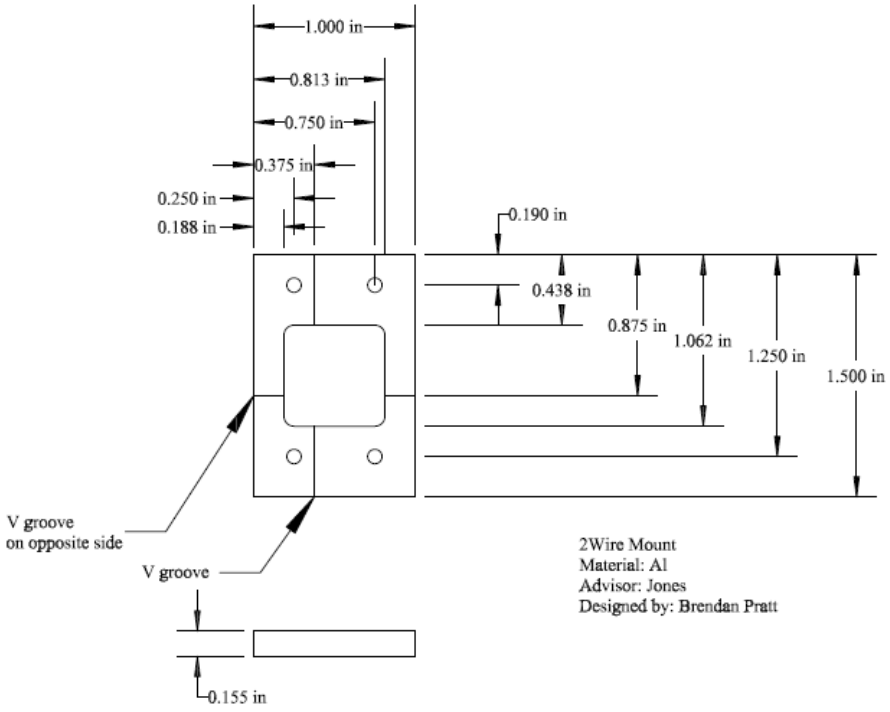

Figure 2.6: CAD rendering of mounting fixture used for measuring the focal spot in both x and y planes.

Each mount was machined with horizontal and vertical v-grooves which were positioned so that their crossing point defined the same spatial coordinates in X,Y,Z (with respect to the four reference pins that held it in the mount) as the corner reference point on the aluminum mount used to hold the diamond target during ablation. The design allowed the harp scan mounts to be used to define the origin of the beam spot if desired. The entire mount was then anodized to insulate it from the gt wire as well as the ablation chamber itself. As the laser irradiates the gt wire, electrons are freed via the photoelectric effect and a positive current flows through the wire which can be measured. Fig. 2.7 shows a typical pulse generated from the gt wire while it is being pulsed with the laser.

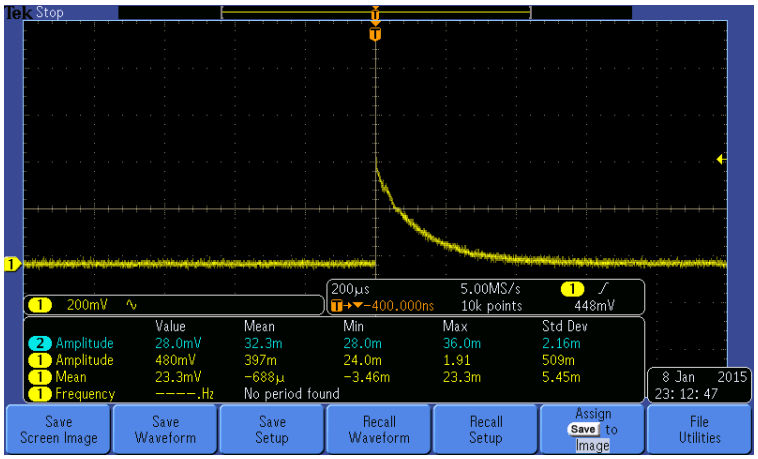

Figure 2.7: Current response of gold-tungsten wire pulsed by 193nm laser.

The total current produced is dependent on the flux of UV light intercepted by the wire and therefore proportional to the x or y projection of the local intensity of the beam as the wire. Scanning the wire through the beam waist creates a series of pulses from the gt wire that rise and fall in amplitude, the peak defining the coordinate of the laser pulse maximum for that particular position of L3. An integrating circuit was designed and constructed to sense the current flowing on the gt wire and generate an output pulse proportional to the total charge. The diagram for the circuit is below in Figure 2.8.

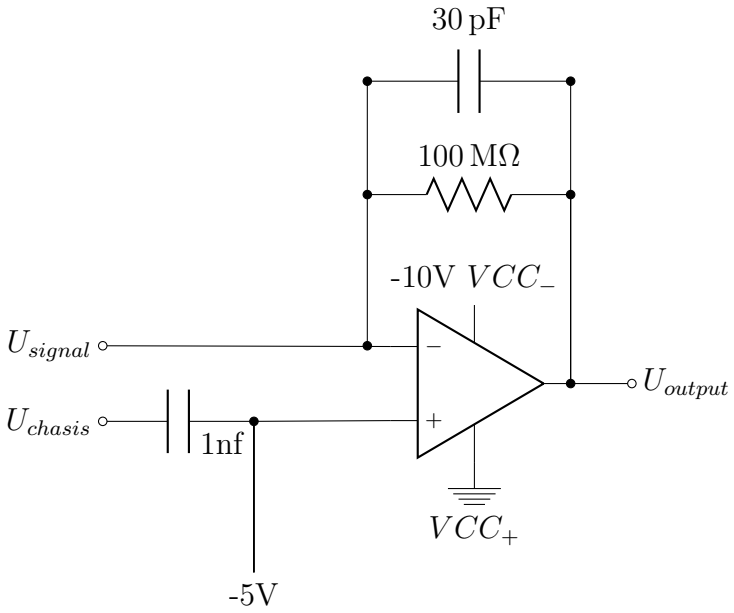

Figure 2.8: Schematic of integrating circuit used for focal study.

The scans were done in pairs of 2d projections xz (called x-scans) and yz (called y-scans). Between the scans the wire frame was swapped out because separate frames were used for the vertical (x-scan) and horizontal (y-scan) wires. The 2d scans consisted of an inner loop over the transverse coordinate, and an outer loop over z. The transverse coordinate range was 2mm and the z coordinate range was 12mm. The LabView application that was used to run the scans saved the output from each step in the outer loop. Each pass was performed for a single value of z, and swept over the full 2mm range in x or y.

The output of the integrating circuit was connected to an ADC which was sampled continuously over that the whole time period the scan was taking place. These data were written to a text file and analyzed with modules written in ROOT and Python to create 2D images of the scan data. The first set of data was taken over a limited range in z that covers the empirical focal point of L3 and therefore the z-dependence is difficult to discern. However, the transverse shape of the focus is well measured and shown in Figure 2.9.

Each pixel in the plots represents one laser pulse, with the color representing the pulse height integral. The lower-most row should be ignored because the scanning program was not yet fully synchronized to the raster pattern. The widths of the focal spot in x and y are shown in the RMS values of the fits in Fig. 2.10. The values in x and y are roughly the same, 65 μm vs 48 μm respectively. The peak in the y distribution looks much narrower because the range spanned by the y-scan in this case is wider than what was used for x. After this, the same scan range in x and y of 2 mm was used. The scans were completed again over the entire range of the z translation stage (12 mm) so that the divergence of the beam could be measured.

The plots in Fig. 2.11 show the data. In Figure 2.11 the region above z = 6 mm is increasingly filled with a uniform background. The dropout in the signal around row $z = 6.5$ mm in Fig. 2.11a seems to have caused a small offset in x for rows above $z = 6.5$ mm. This effect appears only in the high-background region beyond the focal point, so no attempt was made to correct for this offset. To verify that the background is real and not just a

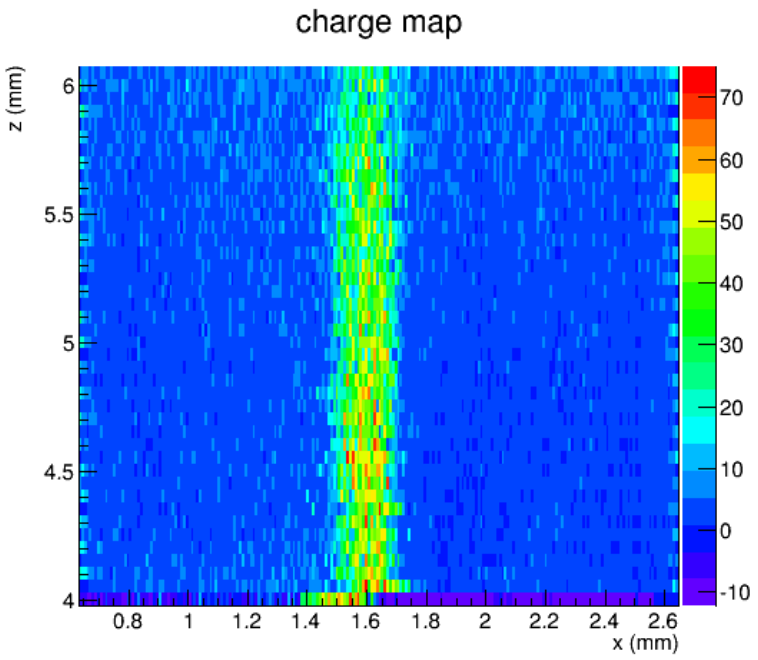

(a) 2.9a

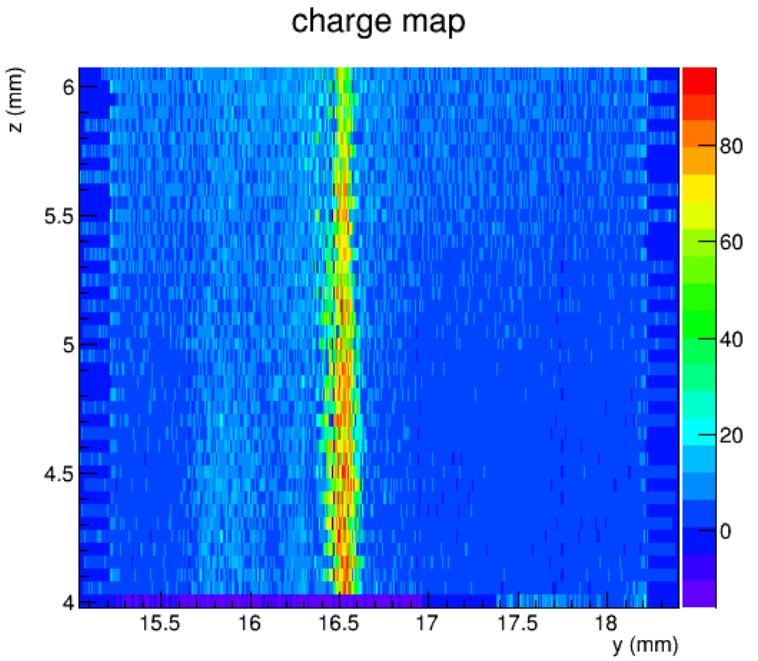

(b) 2.9b

Figure 2.9: Color maps of the two orthogonal scans of beam focal region, where the color represents the charge per pulse seen on the wire in arbitrary units.

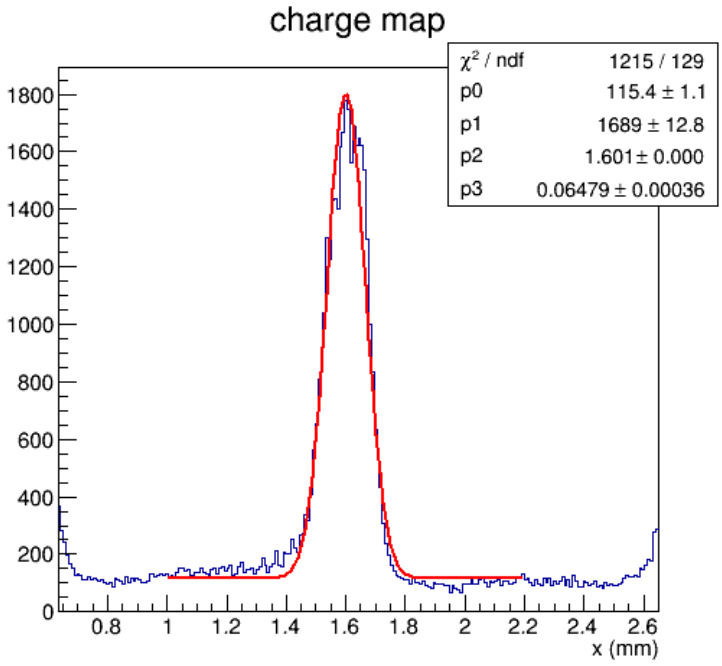

(a) 2.10a

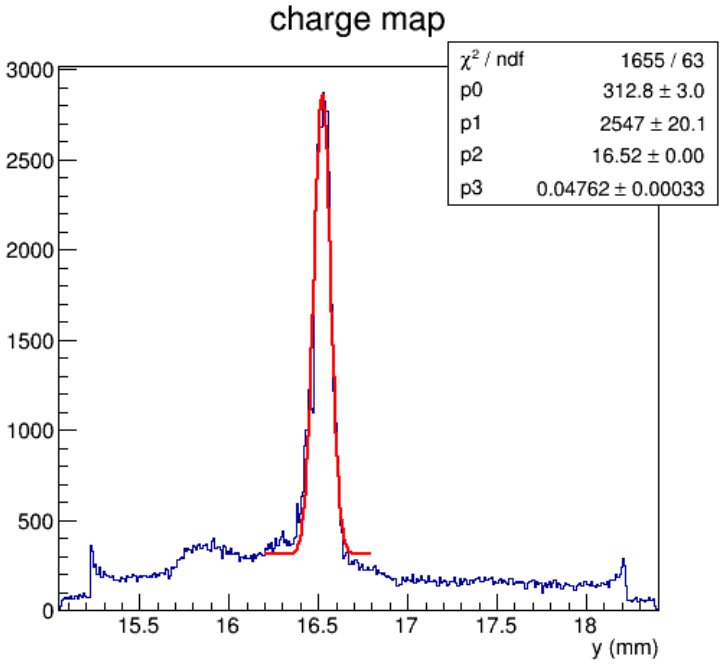

(b) 2.10b

Figure 2.10: Projections of the color maps shown in Figure 2.9 onto the transverse axis with Gaussian fits to central peak over a flat background.

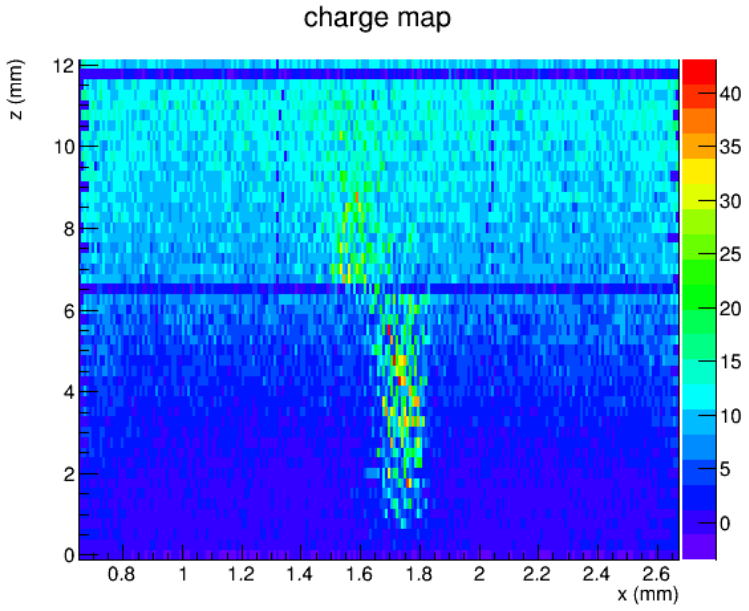

(a) 2.11a

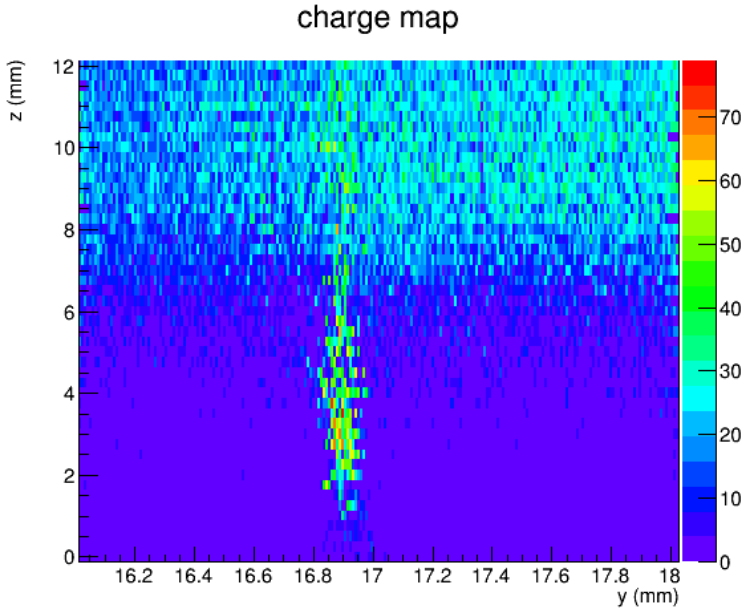

(b) 2.11b

Figure 2.11: Color maps of the two orthoganol scans of beam focal region, where the color represents the charge per pulse seen on the wire in arbitrary units.

systematic shift of the baseline level or an analysis bug, a primitive sum of the total adc sum for each row in the scan was taken. These sums are shown in Figure 2.12 as a function of the z coordinate of the scan row. The effect is clearly seen in the raw pulse data. To better understand the diffuse background that appears past the plane of focus, a collimator was set up at the zero-crossing between the two lenses in the beam expander (L1 and L2). The collimator was made of a sheet of brass that initially had no hole, that was ablated through by the beam to form a hole with the approximate size of the central region of the beam at that point. The hope was that eliminating non-central rays at that point might help to clean up the beam at the ablation point and make it more Gaussian. The charge maps for these scans are shown in Figure 2.13. There was a definite improvement from the collimator in terms of removal of the background, perhaps by as much as a factor 3. From this study it was determined that the collimator should be in place during diamond ablation, just for the purpose of protecting the diamond surface away from the ablation point. There was still a significant background component present at high z, even with the collimator in place. One possibility would be that the aluminum stand on which the wire scanner rests was being ablated, and aluminum ions from the ablation plume were being attracted to the wire. Sitting at a negative potential, it is certainly possible that the ions would drift to the wire. Given the integration time scale of several hundred microseconds after the pulse has passed, it is plausible that this might be causing this effect, or at least part of it.

Ablation Rate in Diamond

The ablation rate of diamond was studied over a wide range of laser energies. This was accomplished by pulsing the laser at a constant rate of 50 Hz while sweeping the diamond across the focal spot at a speed of $0.5\frac{mm}{s}$. After each completed row the diamond was shifted vertically by 10 μm (y translation stage) and the process was repeated until a 6.2x6.2mm^2 area was rastered. For each row, the average laser pulse energy and the row's y-coordinate on the diamond was calculated and recorded . The laser was run without the gas purification

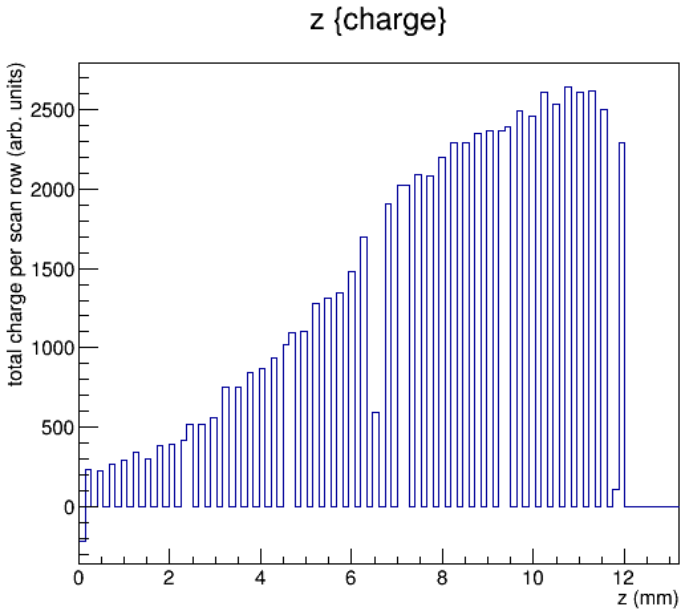

(a) 2.12a

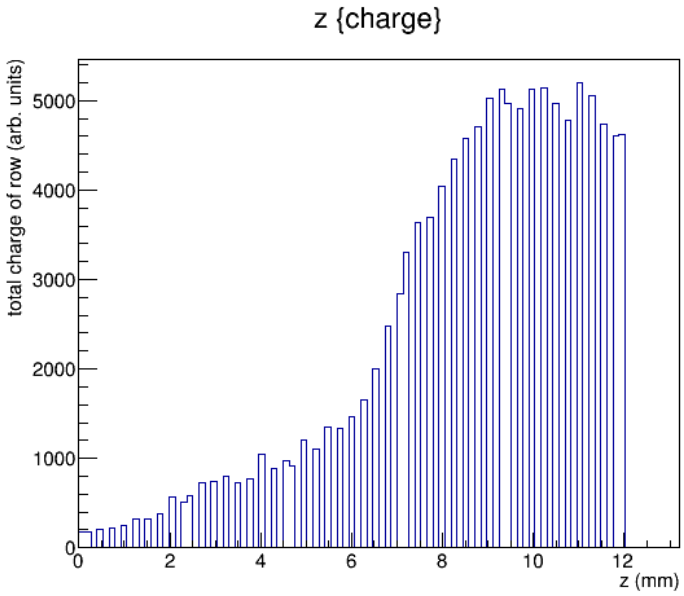

(b) 2.12b

Figure 2.12: Row-wise sums of the total charge seen in each of the lateral scans in Fig. 2.11. The focus seems to lie somewhere in the vicinity of z=4.5mm.

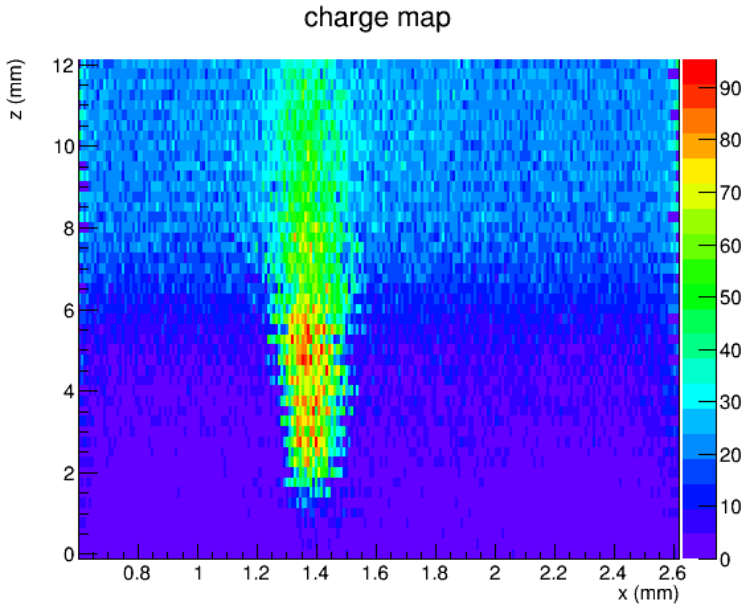

(a) 2.13a

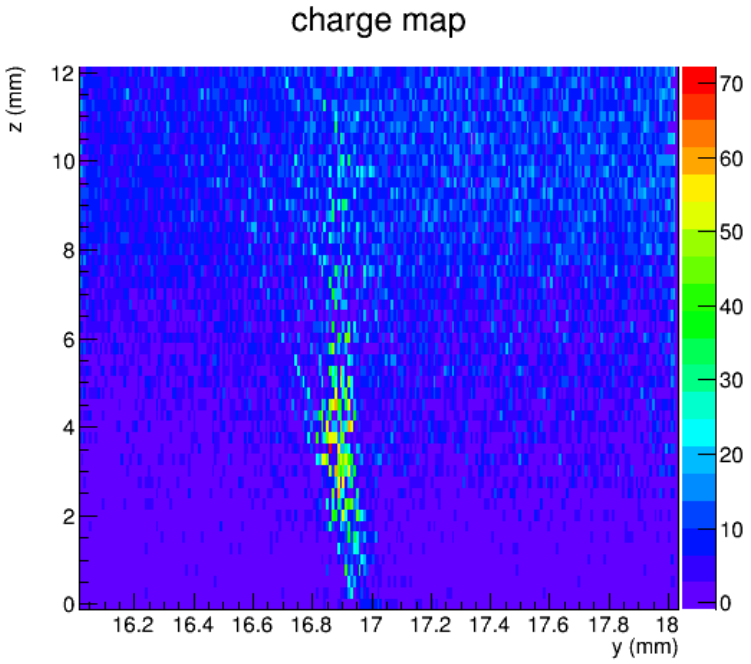

(b) 2.13b

Figure 2.13: Color maps of the two orthoganol scans of beam focal region using a collimator.

system and the laser energy dropped slowly as each row was completed, ensuring the study covered the complete energy range of the excimer laser. The ablated surface of the diamond was measured using a Zygo white-light interferometer and is shown below in Figure 2.14a.

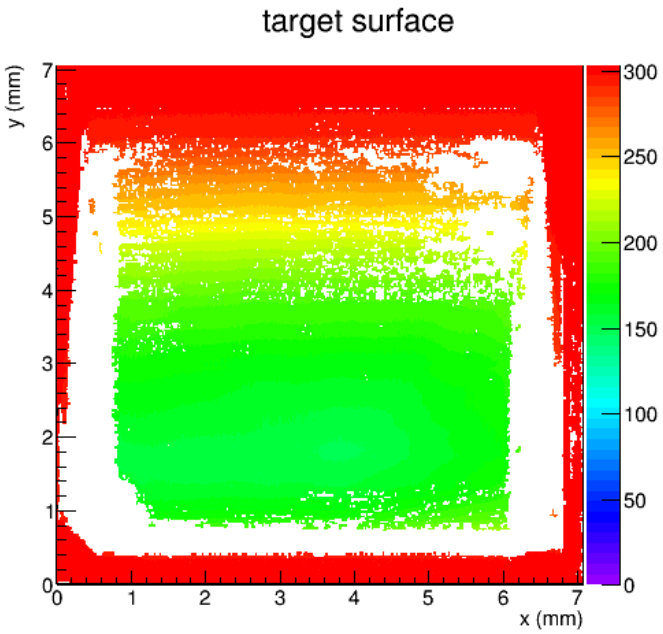

(a) 2.14a

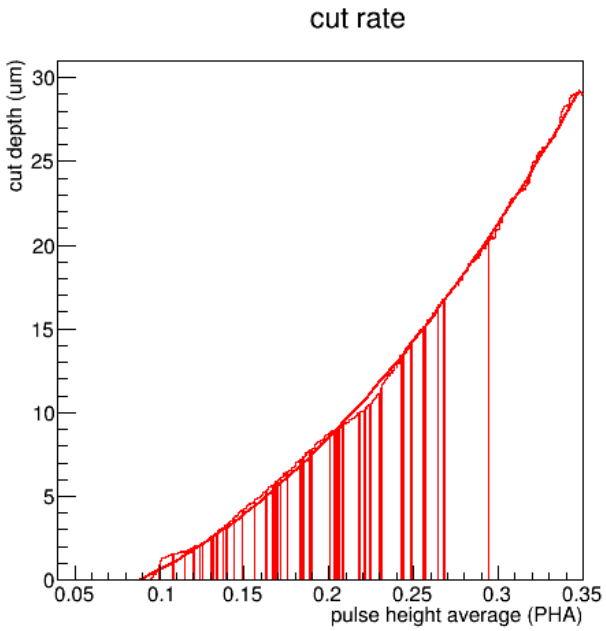

(b) 2.14b

Figure 2.14: Left: Zygo image taken of the diamond after ablation with varying laser energies. Right: Measured ablation rate in diamond as a function of laser energy fit with a second order polynomial

The depth of ablation in the diamond corresponds to the average laser energy deposited for that particular row. The ablation rate was derived from the measured ablation depth

as a function of y (U(y)) using Eq. 2.1 which accounts for the overlap between neighboring laser pulses as well as the fluctuations in laser energy (e_{laser}) from row to row.

$$R(e_{laser}) = \frac{U(y) * \delta x * \delta y}{V_0} \tag{2.1}$$

U(y) is the number of microns removed from the diamond surface after ablation at a particular y coordinate as extracted from the Zygo interferometer, δx and δy are the distances between neighboring pulses (both 10μm) and V_0 was a normalization parameter representing the volume of diamond that is ablated by a single reference laser pulse. The data collected from Figure 2.14a was used in Eq. 2.1 and plotted as a function of the laser energy shown in Figure 2.14b. The fit of Figure 2.14b was made using a second order polynomial and is shown below in Eq. 2.2.

$$R(e_{laser}) = 245.347x^2 + 5.440x - 2.390 \tag{2.2}$$

2.1 Laser Ablation Control during Diamond Radiator Production

During the ablation process the average laser energy was measured for each completed row and the corresponding ablation rate was measured using Eq. 2.2. The ablation rate calculated from the last completed row was used to determine its overlap with the next row of laser pulses. The overlap was adjusted by weighting a standard step size made by the y-translation stage (y-step) by the ratio of the measured ablation rate with a desired rate of ablation as shown in Eq. 2.3.

$$\Delta\text{y} = \frac{R_{measured}}{R_{desired}} \times \text{y-step} \tag{2.3}$$

Stacking laser pulses on top of each other increases the amount of diamond material removed within the region of overlap. This method was used to account for laser energy fluctuations while differentially ablating diamond to achieve $\pm 0.5\mu$m surface variation.

2.1.1 xyz Ablation Chamber

During the ablation process the diamond target was fixed on an aluminum slide inside the ablation chamber with a small amount of thermal grease applied to the back surface of one corner of the diamond, providing thermal conduction between the diamond and the aluminum slide during the ablation process as shown in Figure 2.15.

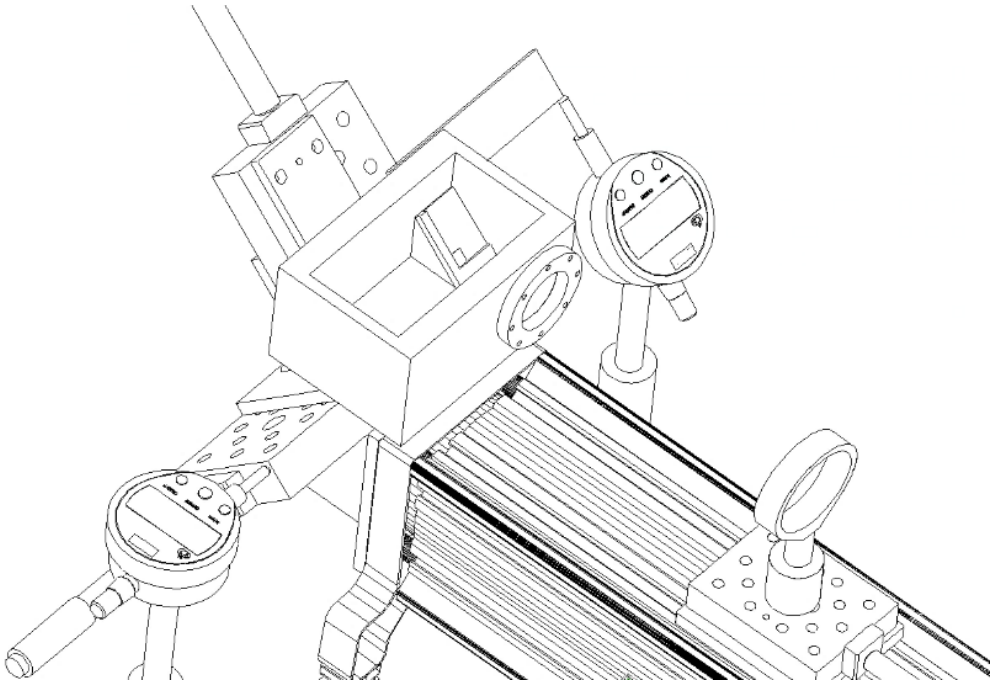

Figure 2.15: Rendering of a diamond mounted in ablation chamber held at an angle of 45°.

The diamond was held at a 45 ° angle with respect to the incident laser pulse so that the resulting plume (which is ejected normal from the diamond surface) does not coat the quartz entrance window with an opaque carbon film. Without this angle, carbon buildup would reduce the UV transmittance of the quartz window and greatly reduce the ablation rate.

Chamber Pressure and Ablation

The chamber was pumped on continuously with a roughing pump during the ablation process. Both the ablation rate and the amount of non-diamond residue left on the ablated surface

are greatly affected by chamber pressure during ablation. Ablation chamber pressures less than 400 mtorr resulted in an increase in black amorphous non-diamond debris left on the sample and a decrease in average cut depth. Ablation chamber pressures above 500 mtorr, but below 1000 mtorr, resulted in a surface with relatively low amounts of amorphous carbon and a high average cut rate (38 μm per full pass). Above about 1 Torr, the ablation rate began to drop again, presumably due to non-linear strong-field absorption of the UV beam by oxygen in the background gas near the region of the focus.

The build-up of amorphous carbon at low chamber pressures is attributed to the chamber's low oxygen content. As the hot carbon plasma is ejected from the diamond surface in the form of the ablation plume it combines with oxygen molecules to form CO or CO_2 if present. In the case of low oxygen, the carbon cools and deposits back onto the diamond as amorphous carbon. This layer of amorphous carbon has a secondary affect when the next laser pulse is incident on the diamond as it absorbs a large percentage of the UV photons, shielding the bare diamond beneath and significantly reducing the ablation rate. Empirically, I found that ablation chamber pressures between 500 and 1000 mtorr contain enough oxygen to capture most of the hot carbon atoms before they deposit back onto the diamond surface.

If the oxygen content inside the ablation chamber is increased to above >1 Torr, up to >1 atmosphere, the diamond is left with an extremely clean surface with no visible amorphous carbon. However, the sharp focus used to ablate the diamond quickly ionizes the atmosphere around it and produces large quantities of ozone (O_3). Ozone is an extremely good UV absorber, and the result is a reduced cutting rate of diamond (<5 μm per pass). Most of the ablation on diamond presented in this thesis was conducted at chamber pressures in the range of 500 - 650 mtorr. The use of a needle valve and electronic flow control meter were employed to control the total pressure variation within $\pm$ 10 mtorr over the course of an entire pass over a $7 \times 7\ mm^2$ diamond.

Translation Stages

As shown in Figure 2.16 the ablation chamber is mounted on two orthogonal translation stages, both with bidirectional repeatability of <1.5 μm and minimum achievable incremental movement of 0.05 μm. The x-stage moves the diamond in the horizontal plane with respect to the lab floor. The y-stage moves at a 45° angle with respect to the lab floor within the same plane as the diamond.

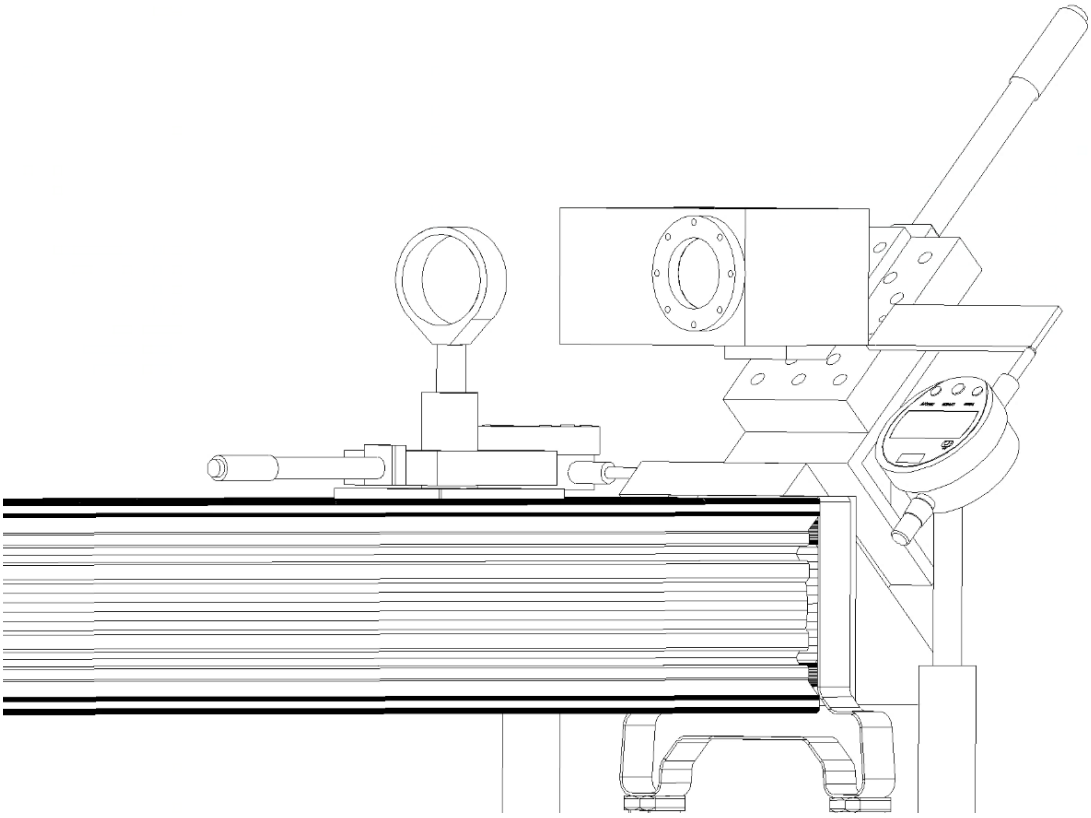

Figure 2.16: Rendering of the ablation chamber, xyz translation stages, digital dial indicators and the final focusing lens L3.

Digital dial indicators with sub-micron resolution were installed to measure the absolute positions of the x and y translation stage and were used in a study to measure the non-linearity of the y-translation stage motor. Non-linearity (movement in the lead screw of the translation stage which does not place the stage at the requested position) of the y-stage is critical due to the row-by-row rastering sequence used to differentially ablate the diamond

sample. Each row has a unique sequence of laser pulses that correspond to an exact position on the diamond and the control of the ablation rate relies on the overlap between these rows.

The dial indicator shown in Figure 2.16 is placed at a 45° angle and makes contact with an aluminum extension mounted to the y-stage. The dial indicator has a rolling bearing attached to its end so that it rides along the extension as the x-translation stage moves back and forth during an ablation sequence. The ablation chamber was moved to a series of y coordinates and the difference between the desired displacement and the displacement measured by the dial indicator was taken, as shown in Figure 2.17a.

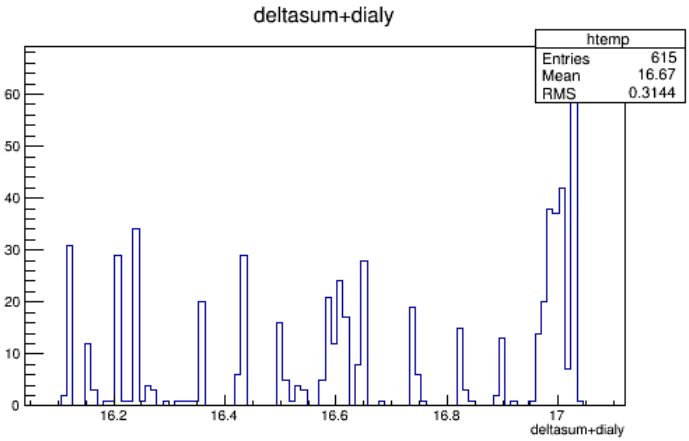

(a) 2.17a

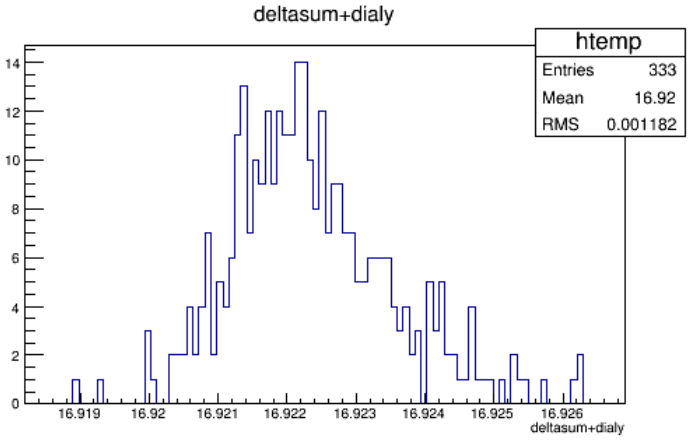

(b) 2.17b

Figure 2.17: Left: The histogram shown displays the difference between the position reported by the y-stage and the position measured by the dial indicator. The x axis in these histograms is plotted in mm. The wide RMS suggests a large non-linearity in the motor. Right: The histogram in shows the same difference after the dial indicator was used to correct for the non-linearity in the y-stage.

The same study was conducted again, but this time the read-back value from the dial indicator was used by the control program to adjust the y-translation motor set point, to require that the y-translation stage fall within 1 μm of the desired position. This was accomplished by creating an internal loop within the LabView software responsible for the movement of the translation stages. At the beginning of the sequence, the y-stage is homed and brought to an origin position. The reading of the dial indicator at the origin is recorded and referenced for all subsequent moves made by the y-stage. After the y-stage moves to

the requested coordinate, the LabView software queries the dial indicator for a position. If the dial indicator value matches the expected value to within 1 μm, the sequence continues. However, if this condition is not satisfied, the y-stage is moved by the difference between the measured and desired position of the dial indicator and the cycle repeats until the position of the y-stage is within 1 μm of the desired coordinate. The histogram shown in Fig. 2.17b has an r.m.s. of approximately 1 μm, illustrating the improvement made to the positional accuracy of the y-stage through the use of the sub-micron dial indicators which were used throughout the ablation of diamond samples presented in this thesis.

2.1.2 Ablation Software

An extensive software package was written at the University of Connecticut by Dr. Richard Jones for the purpose of creating 20 μm diamond radiators. The software worked in conjunction with a Zygo white-light interferometer to produce files which contained a sequence of laser pulses to be placed at specific coordinates on the diamond using the ablation setup described above. A three dimensional model of the diamond was created in the ablator software having the exact dimensions and surface variations of the original unablated sample. A target model was then created with the desired dimensions of the completed radiator. An example of these two models are shown in Fig. 2.18.

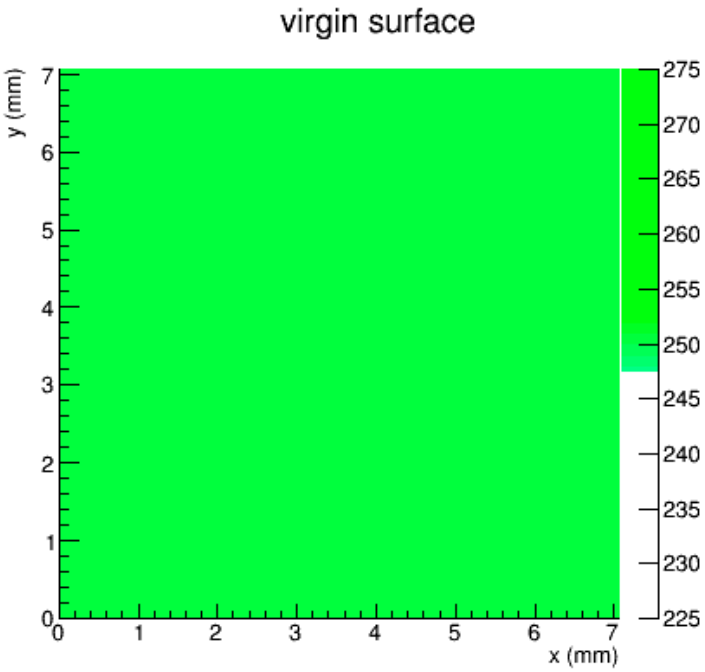

(a) 2.18a

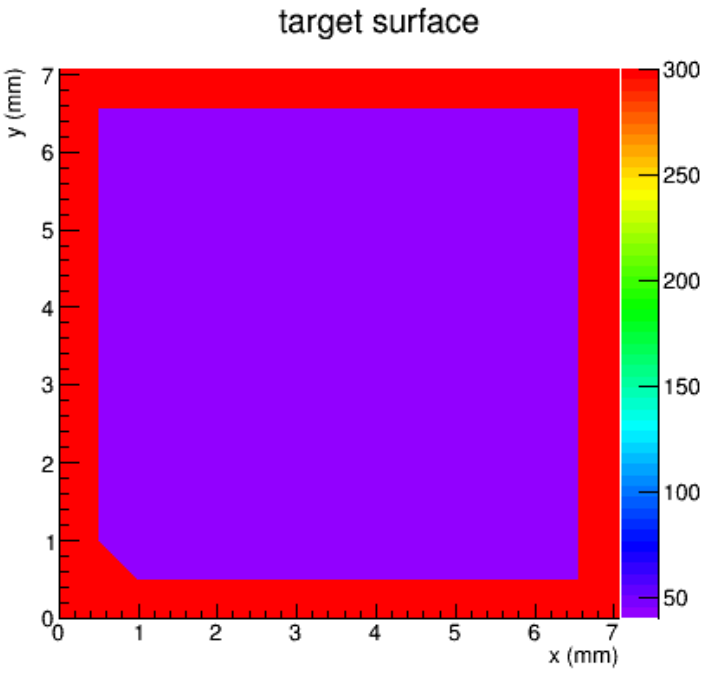

(b) 2.18b

Figure 2.18: Three dimensional models of the diamond sample before ablation (top) and the desired shape afterwards (bottom).

Transforming from Fig. 2.18a to the target shown in Fig. 2.18b was accomplished in software by the deconvolution between the difference of the two three dimensional objects shown in Fig. 2.18 (D) with the modeled beam spot (B), resulting in the raster pattern (R). This relationship is shown in Eq. 2.4.

$$R \otimes B = D \tag{2.4}$$

To solve this, the convolution theorem was implemented so that the Fourier Transform of Eq. 2.4 becomes the following.

$$DFT(R) = DFT(D)/DFT(B) \tag{2.5}$$

This procedure worked well when the measured surface profile D was taken from Zygo images of the virgin diamond. However as soon as the diamond had been cut with the laser, there were regions of the surface that the Zygo could not measure (eq. the steep edges where the reflectivity is poor) leading to a large fraction of the D function whose values is undetermined by measurement. By trial-and-error, an algorithm was developed for filling in the missing regions using a smoothing and interpolating procedure. Once these corrections were implemented to the two parts shown in Fig. 2.18, their discrete Fourier Transforms could be taken. The difference between these DFTs was then divided by the discrete Fourier Transform of the focal spot (which was digitized in the software based on measurements described above). The inverse DFT of this resultant was taken to produce the final raster pattern. This method enables the user to take a diamond at virtually any stage of the ablation process and create a rastering pattern that, when applied using the ablation setup, will closely resemble the target model. An example raster pattern is shown in Figure 2.19 for a diamond that required some reshaping. The content of each pixel represents the position and total number of laser pulses required to ablate the diamond to match the target.

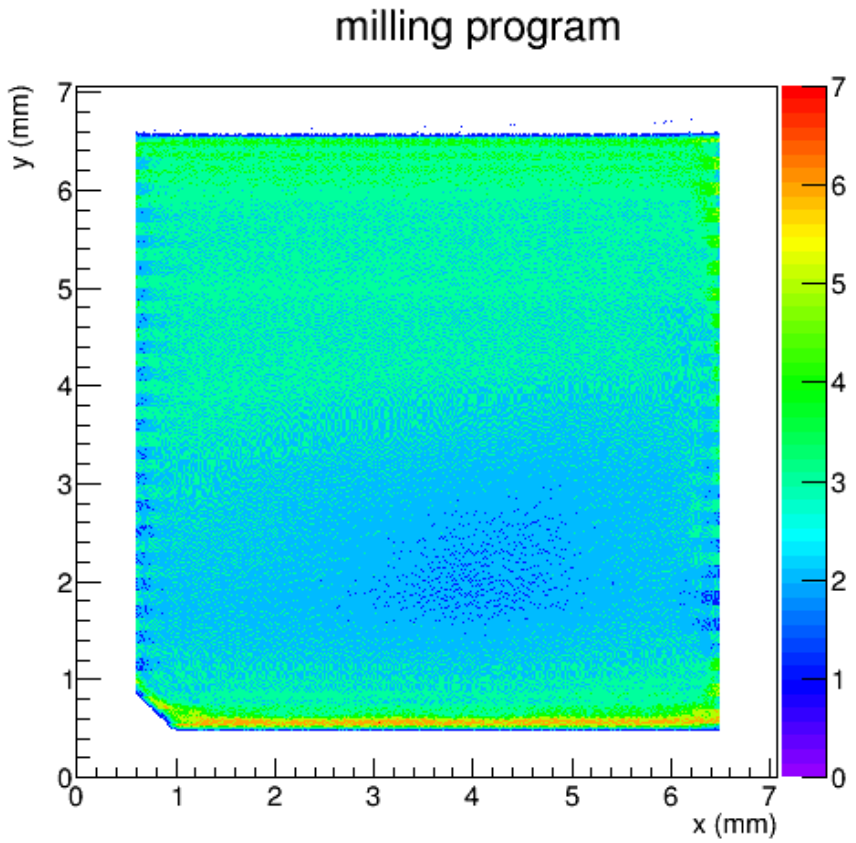

Figure 2.19: Raster pattern generated for sample diamond using the ablator software. The points in the regions of the frame are masked off before the program is passed to LabView for execution by the apparatus

Detrenching

The algorithms used by the ablator program to generate a map of laser pulses that produces a final surface with a desired shape profile assumes that the laser pulses are all identical. In actual fact, this assumption is violated in two ways.

1. The initial string of laser pulses generated after the laser has been off for a few-second period have significantly higher energy than their steady-state average.
2. There are random pulse-to-pulse variations in the laser energy even after the output reaches its steady-state-average.

The effects of (2) tend to cancel out on average and result only in the surface being somewhat rougher than predicted by the model. The effects of (1) are more serious because they all tend to pile up at edges of the cut region, at the ends of the raster pattern where the laser pulse sequence starts and ends. The effect is seen at both ends because of the serpentine motion pattern, and appears as trenches up to 20 μm deep that appear along the left and right boundaries of the cut region.

To account for this effect, the pulse energy is modeled as an exponential decay from an initial level to the steady-state level as shown in Eq. 2.6.

$$E(t) = E_0 * (1 + T_F \times \exp\left(\frac{-t}{T_L}\right)) \tag{2.6}$$

where E_0 is the steady-state pulse energy and t is the time in units of pulse counts (20 ms at 50Hz), where the first pulse appears at time t = 0. The T_F (taper factor) and T_L (taper length) were empirically measured by recording the energy of a series of over 600 laser pulses and fitting the form of Eq. 2.6as shown in Fig. 2.20.

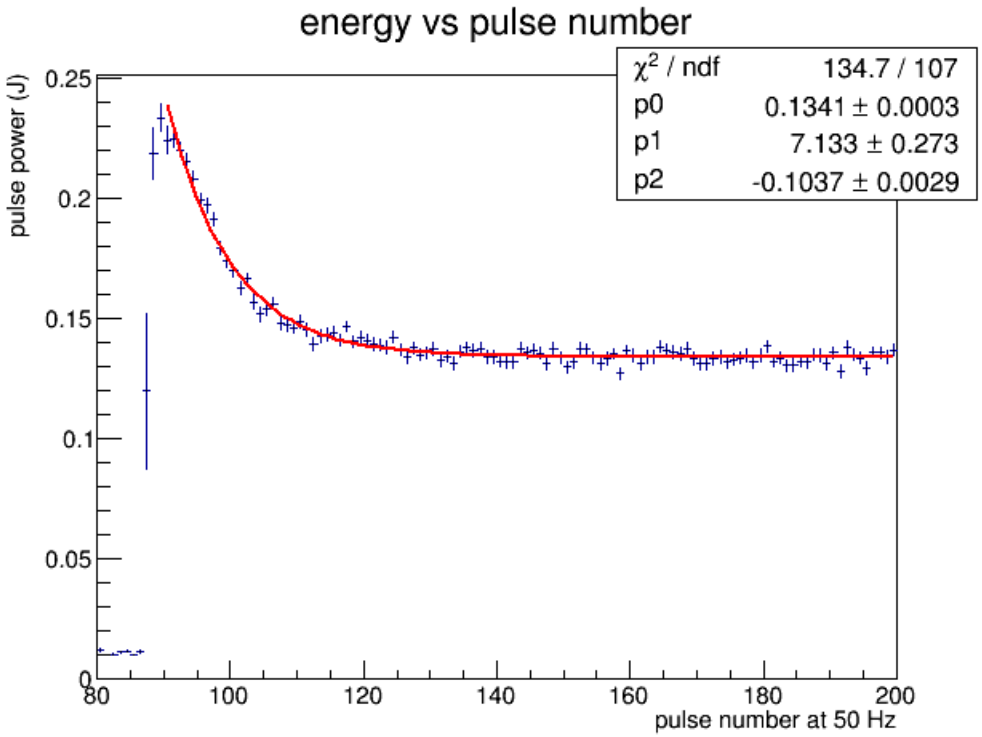

Figure 2.20: Energy (J) of consecutive laser pulses at a repetition rate of 50 Hz. The blue points are data measured using energy meter 2 as shown in Figure 2.1. The red line is a fit to the data using the form of Eq. 2.6. Parameters are shown in the inset.

To correct ("detrench") the program, some assumptions need to be made regarding the sequence in which the program pulses are laid down. They are stored in the program map as a total pulse count per pixel, but in actual fact they are not laid down by sitting at a single pixel and dropping N pulses, then moving to the next pixel. Instead, they are laid down in a series of passes over the entire surface, where each pixel receives one pulse per pass. This allows the control program to move the sample at a fixed motor speed, while the laser is pulsing at a fixed frequency., allowing several hundred pulses to be generated at a time without pausing. Correcting the program to account for the power taper effect requires taking into account that the t = 0 point appears at a different location on each pass. Let r(t) be the pulse repeat count pattern for a given row of the program, and $r_{corr}(t)$ be the effective pulse repeat count that the program will produce after accounting for the power

taper effect.

$$r_{corr}(t) = r(t) \times (1 + T_F) - \frac{T_F}{T_L} \exp\left(\frac{-t}{T_L}\right) \int_0^t r(t') \exp\left(\frac{t'}{T_L}\right) dt' \tag{2.7}$$

To detrench the program, the input program to give $r_{corr}(t)$ for each pixel is taken and the above integral equation is inverted to solve for the r(t) that is needed in order to achieve it. The result is:

$$r(t) = s(t) \times \exp\left(\frac{t}{\tau}\right) \times \exp\left(\frac{-t}{TLength}\right) \tag{2.8}$$

where

$$\tau = T_L \times (1 + T_F)/T_L \tag{2.9}$$

and

$$s(t) = \frac{\int_0^t f'(t') \times \exp\left(\frac{-t'}{\tau}\right) dt'}{(1 + T_F)} \tag{2.10}$$

where

$$f'(t) = \frac{d}{dt} f(t) \tag{2.11}$$

and

$$f(t) = r_{corr}(t) \times \exp\left(\frac{t}{T_L}\right) \tag{2.12}$$

Using the above algorithm the ablator software creates raster files which account for the initial spike in laser energy over the first few pulses. Without this addition to the software it would be impossible to machine a diamond radiator to 20 μm because the trenches created would exceed this thickness and create holes in the thin region.

Laser Triggering

The contents of the raster files are read by a stand-alone pulser program running on a micro-controller called the Trigger Master (TM) which is used to trigger the laser (or not) every 20 ms. The TM GPIO bus is capable of producing 3.3 V logical outputs, whereas a 15 V, 50-100 μs long signal capable of driving 50 Ω is required to trigger the laser. The output signal of

the TM (which is controlled by the pulser program) is connected to the circuit shown below to generate such a triggering signal.

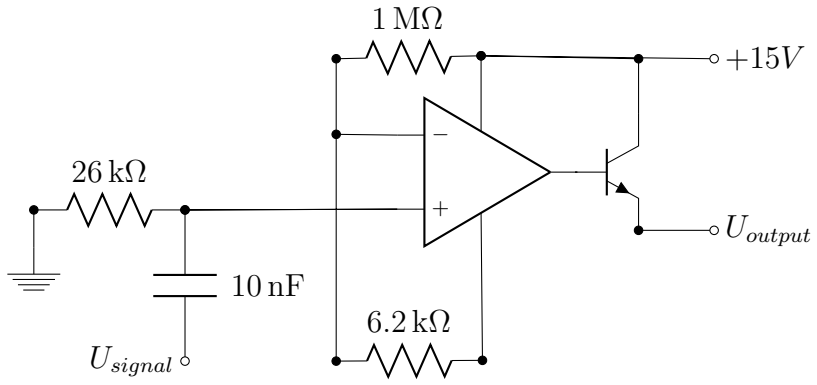

Figure 2.21: Schematic of pulser circuit used to trigger the laser head.

The LabView software (which will be discussed in a later section) issues commands to the motor stages to move at a given speed across the sample, and then sets one of the TM GPIO pins (GO) to a high state. This is the signal that the pulser program should start pulsing at 50 Hz until the fixed number of pulses have been completed. The GO pin should return to a low state around the time that the pulse pattern has completed. After the preset pulse pattern is completed, the GO pin should transition from low to high again to start the next row. The actual sequence of fired/skipped pulses during a single row is encoded in the raster file, one pattern per line. Each pattern is executed at least once, and possibly multiple times as determined by the LabView software. Whenever it is time to advance the next pattern (the next line in the raster file), a second GPIO pin (ADVANCE) on the TM is asserted together with the initial GO pin. The pattern on each line in the input sequence file may be executed in either forward or reverse order, and it is up to the pulser algorithm to generate the pulse sequence in the order that is consistent with the serpentine pattern of motor sweeps across the sample. The first row is always left-to-right. If for some reason the LabView software tells the pulser program (via the ADVANCE pin that is monitored by the TM) to advance past the last line in the sequence file, it is programmed to fall back to the empty pattern where no laser pulses are generated.

The pulser algorithm is designed not to be interruptible in the middle of one row pattern, but at the end of each row it pauses and must see the GO pin go high again before any more pulses are generated. The pulser program also needs to know which direction the motors are moving in, left-to-right or right-to-left. This information is communicated from the LabView software by setting (right-to-left) or resetting (left-to-right) a third GPIO pin (DIRECTION) before the GO edge.

The pulser program additionally monitors the pulse data recorded by the laser's Intelligent Laser Control (ILC) and makes intelligent decisions based on this information. The ILC is given a target pulse energy which it tries to maintain by regulating the high voltage level of the laser head. This is done autonomously except that it can easily fault if the gain of the laser medium drops below a sufficient level. When this happens, the ILC switches off the laser and quits responding to pulses sent from the pulser program. Detection of this situation is accomplished through communication between the ILC and pulser program over a serial RS232 bus. This is wired to a usb-serial adapter on one of the usb ports on the TM. The TM open-source library [20] is used to manage this interface. Initialization takes place when the pulser program first starts up. It opens the communication to the ILC and takes over control from the front panel. This means that the user should not attempt to control the laser from the front panel once the laser is ready to run an ablation pass.

To prepare for initialization, the RESET button on the front panel must be pressed just before starting the pulser software. A full asynchronous handshake is then implemented between LabView and the TM pulser, with LabView sending the GO signal to start the row and the TM returning DONE as the row is completed. The GO signal functions, as described above, to tell the TM when to start pulsing a new row. As soon as the last pulse has been issued by the pulser software, the TM queries the laser for the latest pulse count and checks if it agrees with what it asked for on the last sweep. If the two agree within 10%, the TM raises the DONE GPIO pin and the LabView software knows it should add the calculated Δy (as discussed earlier) and proceed with the next row. Otherwise LabView assumes that

the present row is still incomplete, sets Δy to zero and re-sweeps over the same row in the opposite direction.

For this protocol to work, there needs to be a specific time window within which the TM must assert DONE in order for the row to be considered complete. The transaction time for the completion of the laser pulse query cycle was measured and a delay was added to the end-of-row sequence in the LabView software to make sure the DONE, if present, is seen by LabView in time before the next row begins. As soon as the TM sees the GO for the next sweep, it should reset the DONE if asserted. If the pulse count disagrees with the demanded sequence then something went wrong with the laser during the last sweep. Often this will be a terminal condition that makes the pulser program exit wth an error message, leaving DONE permanently low. However, there is one special case which occurs whenever the ILC fails to regulate the pulse energy and flashes the error message, "PRESET ENERGY TOO HIGH". This is not a fatal error. In this case, the laser is automatically re-enabled, and the unfinished pulses from the incomplete row are redone, then the program continues as usual. If this continues to happen, the operator must decide whether to refill the laser gas (to increase the average laser power) and manually re-enable the laser, and then tell the TM to repeat the last row that failed to complete successfully. After this is done, the program continues as usual.

LabView Ablation Software

Creating a xyz ablation facility with sub-micron resolution required the synchronization of all the individual components discussed in the earlier sections. This is accomplished through a LabView program called AblationStation.vi which controls all of the ablation processes by means of a state machine. When first initialized, all three motors are homed and return to the origin position, which is defined as the position of the x and y motors (as read back from the dial indicators) which places the focal spot directly on the bottom left corner of the diamond. The motor controlling the focal distance of L3 (the z motor) is moved to the

preset value (typically z = 4.5mm) and the pulser.c program is initiated which readies the laser for triggering. The next step in the state machine moves the diamond into the correct starting position for the first row to be ablated. The x motor is given 0.5 mm of extra travel at the beginning of each row to allow the motor to accelerate to its maximum velocity of $3\frac{mm}{s}$. As the x motor advances the diamond toward the starting point for this row, its position is queried every 18μs. Once the x motor position is within the range specified by the raster file, the GO pin is raised via an output pin on the Measurement Computing FS-108 data acquisition module and the pulser.c program begins to trigger the laser with that row's pattern. While the laser is pulsing, a 50 kHz ADC on the FS-108 is recording the laser energy from energy meter 2 (Figure 2.2). When the row is complete, the ADC sequence is read back into LabView and used to compute the average cut depth using Eq. 2.2. The y motor is increased by the Δy amount calculated from Eq. 2.3. If the Δy value was less than the preset value (typically 10 μm), the row is repeated in the opposite direction. Once the total Δy value exceeds the preset value, the next row in the file is read and the sequence begins again. After each move of the y motor, the position is checked by the dial indicators to ensure the position is within 1 μm of the coordinate specified by the the sum of Δy values encountered so far in the run. A step-by-step sequence of what is required to create a series of raster files which can be used to ablate a 300 μm diamond to 20 μm is presented in detail in the Appendix.

CHAPTER 3

Diamond Radiator Characterization

The GlueX experiment requires the diamond radiator to have a mosaic spread of the same order as the electron beam divergence (20 μrad). While it is certainly possible to measure the mosaic spread while the radiator is in the CEBAF electron beam, it is more desirable to have a method for measuring the quality of a radiator before it is installed in the goniometer. Coherent enhancement in the CB photon spectrum and its linear polarization are directly related to the lattice structure of the crystal. Although they are different physical processes, CB and X-ray diffraction share a common dependence on the target crystal structure through the crystal structure factor S($\mathbf{q}$). For a perfect crystal, S($\mathbf{q}$) consists of a regular 3D lattice of delta functions called the reciprocal lattice, whose individual magnitudes are scaled by the atomic form factor.

Distortions from a perfect crystal structure smear out these delta functions in momentum space and reduce their magnitudes. By measuring the intensity of X-rays from a monochromatic, highly parallel beam scattering from diamond crystal, one is able to map out the crystal structure factor for that reciprocal lattice point. As the crystal is rotated through the Bragg angle for the selected wavelength, the range of angles over which the intensity remains high is called the rocking curve width. The ideal rocking curve width for any given lattice vector and X-ray wavelength is set by quantum mechanics, and is called the Darwin width. Any excess rocking curve width over the Darwin width is attributed to a combination of instrumental and mosaic factors. Measuring a r.m.s. width less than 20 μrad automatically guarantees that the mosaic spread is less than 20 μrad and so meets the GlueX requirement.

Rocking curve measurements over the entire area of the radiator (whole crystal rocking curves) were taken at the Cornell High Energy Synchrotron Source (CHESS) and the Canadian Light Source (CLS). Diamonds were measured before and after the ablation process to assess the effects that the thinning procedure has on the crystal quality of the sample.

Measuring the quality of each radiator produced was a significant portion of the author's effort, is discussed in detail in the following sections.

3.0.3 Rocking Curve Measurements of Diamond Radiators

The following rocking curve measurements were carried out at the Cornell High Energy Synchrotron Source (CHESS) C1 beam line in Ithaca, NY. The setup is illustrated in Figure 3.1. The samples were held in a four-axis goniometer between two sheets of stretched mylar. The source of the X-rays was a bending magnet in the circulating 5.5 GeV electron beam located 14.5 m upstream of the goniometer. Without the special X-ray optics that were developed for these measurements, the beam had an angular divergence of approximately 100 μr driven by the 1.5 mm source size. This angular divergence was too large to resolve the 20 μr rocking curve required by the GlueX experiment. Another issue was the wide energy range of the white beam (1 - 50 keV). To solve these issues, the white beam from the bending magnet was sent through a double-bounce asymmetric-cut silicon monochromator as shown in Figure 3.1. This was used to select 15 keV X-rays from the white beam.

The asymmetric cut on both of the monochromator crystals expanded the beam from its initial 1.5 mm r.m.s. in the vertical direction by a factor of 8. The beam was now large enough to illuminate an entire diamond sample at once during a rocking curve measurement. Also, from the expansion of the beam, a reduction in the effective beam divergence (angular spread of beam photons at a particular energy) by the same factor was gained. The monochromator was oriented to the (3,3,1) reflection at 15 KeV. Silicon (3,3,1) was chosen because it gives near-perfect match to the dispersion of the diamond (2,2,0) planes in the sample. A third silicon crystal was aligned to match the same (3,3,1) crystal planes as the monochromator and a rocking curve measurement was taken to test the setup. The rocking curve measurement of the silicon crystal had a width of less than 10 μr, consistent with the Darwin width of 8 μr for silicon (3,3,1) at 15 KeV. The GlueX rocking curve requirement is 20μr, so this measurement showed that the experimental setup was adequate for diamond characterization.

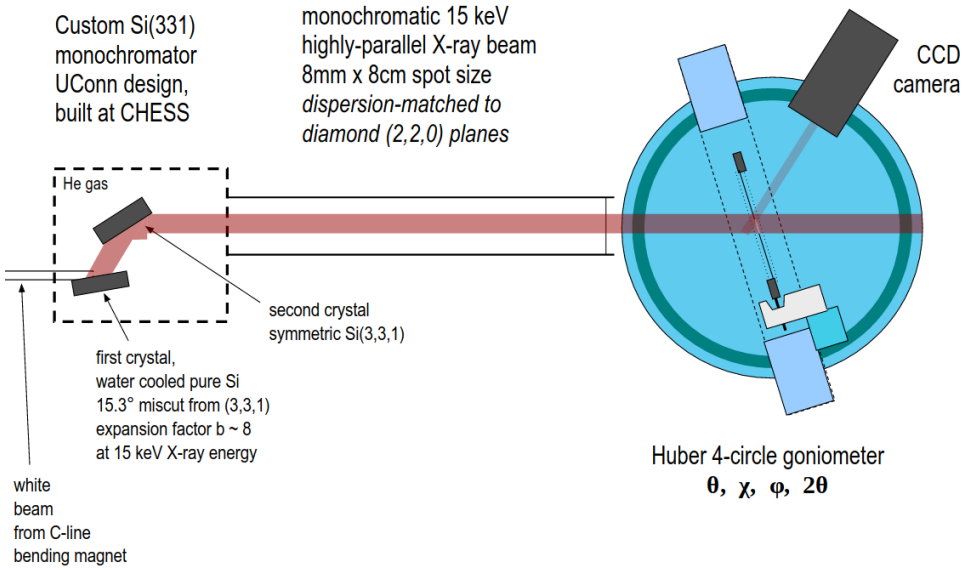

Figure 3.1: Illustration of beamline setup at the Cornell High Energy Synchrotron Source (CHESS). The goniometer angles are defined as follows: θ rotates the diamond target about an axis perpendicular to the page through the center of the blue disc, with a value of zero when the sample is perpendicular to the beam; ϕ rotates the target about an axis in the plane of the figure, indicated by the black shaft that passes through the white block supporting the target; χ rotates the target about an axis in the plane of the paper perpendicular to both the θ and the ϕ axis; and 2θ indicates the position of the CCD camera with respect to the beam direction.

During rocking curve measurements the diamond samples were aligned in the goniometer's center of rotation and the diamond was moved to a nominal position in angles θ, χ, and ϕ. A piece of fluorescing paper was installed in front of the CCD camera and viewed by a video camera which displayed outside of the hutch. Once a Bragg peak was found (indicated by a bright flash on the fluorescing paper), the fluorescent paper was removed and a rocking curve scan was completed. A rocking curve scan consists of a series of CCD camera images taken at a sequence of θ values spanning the full range over which an appreciable X-ray intensity is reflected from some region of the sample. For each value in θ an image of the X-ray intensity was taken by the CCD camera. Scans were typically done with 3.5 μr step size in θ. Each scan would typically have over 200 images which were processed in software. The intensity of each CCD pixel was histogrammed as a function of the Bragg angle (θ) and fit using a Gaussian distribution. Variations in the parameters of these fits (mean and

sigma), when plotted on a two-dimensional xy histogram, show the strain and deformations on the physical position of the diamond from which they were measured. The whole-crystal rocking curve is produced by weighting the mean xy histogram with a normalized Gaussian distribution centered on the diamond (to simulate what portion of the radiator is seen by the GlueX electron beam) and taking the sum of every pixel's intensity plotted as a function of the Bragg angle. This plot is then fitted with a Gaussian distribution and the sigma is reported as the figure-of-merit for the crystal. To generate the desired CB spectrum, the GlueX experiment requirement's stipulate that the whole-crystal rocking curve of a diamond radiator be no greater than 20 μr.

The two-dimensional histogram of the rocking curve mean for an ideal crystal would have uniform color, indicating little variation in θ over which the Bragg condition was met. A two-dimensional histogram of the sigmas for an ideal crystal would have a low average value (around 10μrad) and also be uniform in color. Most of the crystals studied were not perfect and show some level of deformation. It is possible to determine whether the broadening of rocking curve width was caused by uniform bending of the entire crystal or crystal lattice distortions. This was done by measuring the rocking curve of a diamond in at least two orientations, one with the crystal in the nominal (2,2,0) crystal orientation (the first orientation is arbitrarily set), and the other with the diamond rotated in ϕ by 180°. Measuring the same set of crystal planes in two different orientations allows for the separation between bulk curvature and other kinds of lattice distortions leading to changes in the d-spacing between the planes. When a crystal is physically bent, the two rocking curves will show similar structure, but they will be 180° out of phase with each other. However, when the deformation is in the d-spacing, the two rocking curves will be in phase. Knowing the type of deformation offers insight into how the manufacturing process, whether UV laser ablation or not, has affected the crystal and what steps may be taken to alleviate these strains in the future.

The diamond shown in Fig. 3.2 was thinned to 15 μm using a proprietary process developed by manufacturing firm Sinmat, Inc. (Gainsville, FL) that they call reactive chemical mechanical polishing (RCMP). The technique involves fixing the diamond to a slab and exposing the top surfaces to high pressure rotary grinding assisted with chemical slurries which aid to soften the top layer of the diamond. This technique is capable of producing flat and thin diamond radiators however, the rocking curve measurements taken at CHESS show the diamond was left with large mosaic spread and are unusable for GlueX. The deformations are believed to be a result of the large forces exerted on the diamond during the grinding process as well warping due to the crystal's inability to withstand intrinsic crystal strain at thicknesses less than 30 μm.

The measurements shown in Fig. 3.2 demonstrated the need for a technique that could differentially remove material so that a thick outer frame would remain to act as a support for the thin interior diamond membrane. The process also needed to remove the material in a way that did not deform the crystal lattice. It was from these initial measurements that it was decided to investigate UV laser ablation as a method for producing 20 μm diamond radiators for the GlueX experiment with a whole-crystal rocking curve on the order of 20 μrad.

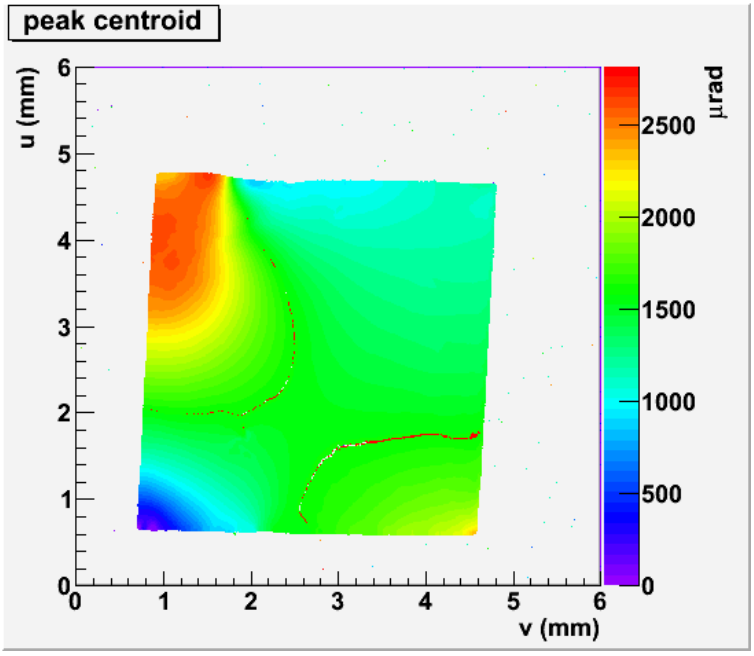

(a) 3.2a

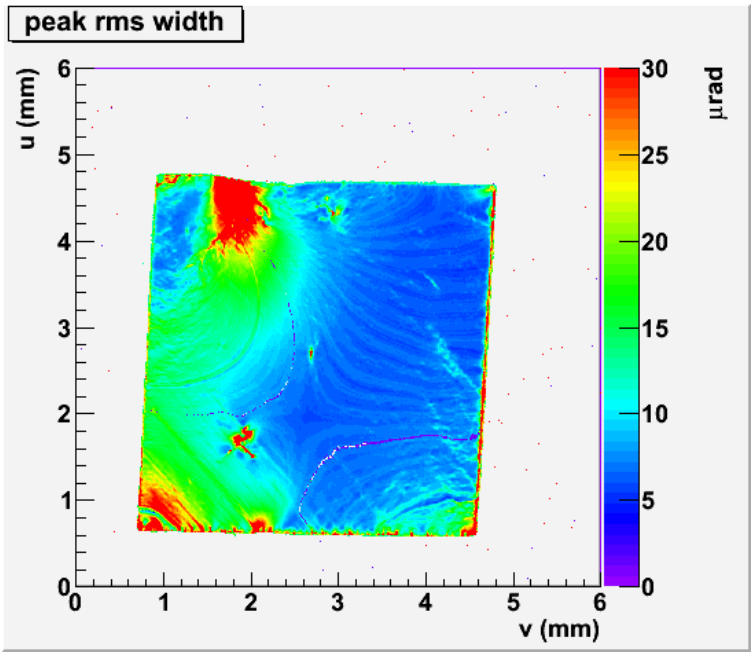

(b) 3.2b

Figure 3.2: Rocking curve measurements for 15 μm diamond thinned using Reactive Chemical Mechanical Polishing (RCMP) process. Panel a (upper) is a plot of the mean value at which the diamond met the Bragg condition. Panel b (lower) displays the r.m.s. of the Gaussian fit made to the pixel's intensity as a function of Bragg angle.

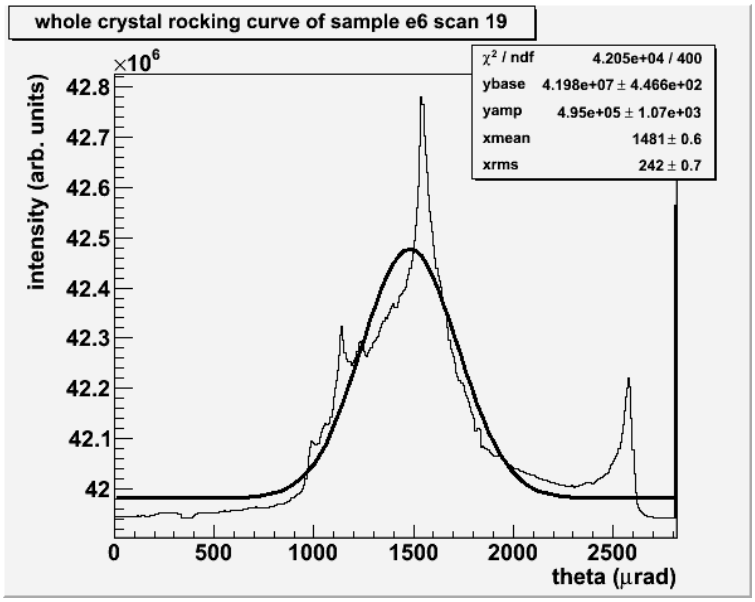

Figure 3.3: Whole-crystal rocking curve plot for 15 μm diamond thinned by RCMP technology. Notice the broad range in θ over which the diamond meets the Bragg condition. This particular diamond has a whole-crystal rocking curve with r.m.s. (sigma) of 242.2 μr, an order of magnitude too large for GlueX purposes.

3.1 Selection of Diamond Material for Laser Ablation

The first steps in producing these radiators was selecting a stock of diamond plates that were of appropriate size, initial thickness, and quality. Diamonds which did not meet the GlueX specifications before laser ablation would obviously not be suitable. Also, finding a supplier that could provide a continuous source of large area ($7 \times 7\ mm^2$) diamond plate at low cost was a concern as well. Some of the very first X-ray measurements taken were done to determine an appropriate vendor and product line that would match these requirements.

A variety of crystals from industrial supplier Element Six were purchased by the University of Connecticut research group so their rocking curves could be measured using the CHESS setup described above. These crystals ranged both in quality, overall thickness and price. Two sets of 300 μm thick diamonds were studied, the first being of "electronic grade" quality and the second, a much cheaper product known as "non-electronic grade". The first set of rocking curve measurements shown in Fig. 3.4 and Fig. 3.5 were conducted to measure any distinction in the rocking curve width between these two product grades. As is clear

from the rocking curve images, the electronic grade crystals are of very high quality. The peak r.m.s. width of the diamond is both locally very narrow and has very little variation across the entire surface of the diamond. The peak centroid plots are also very uniform, only showing some variation in the outer edges which are not exposed to much of the electron beam flux, making it less of a concern.

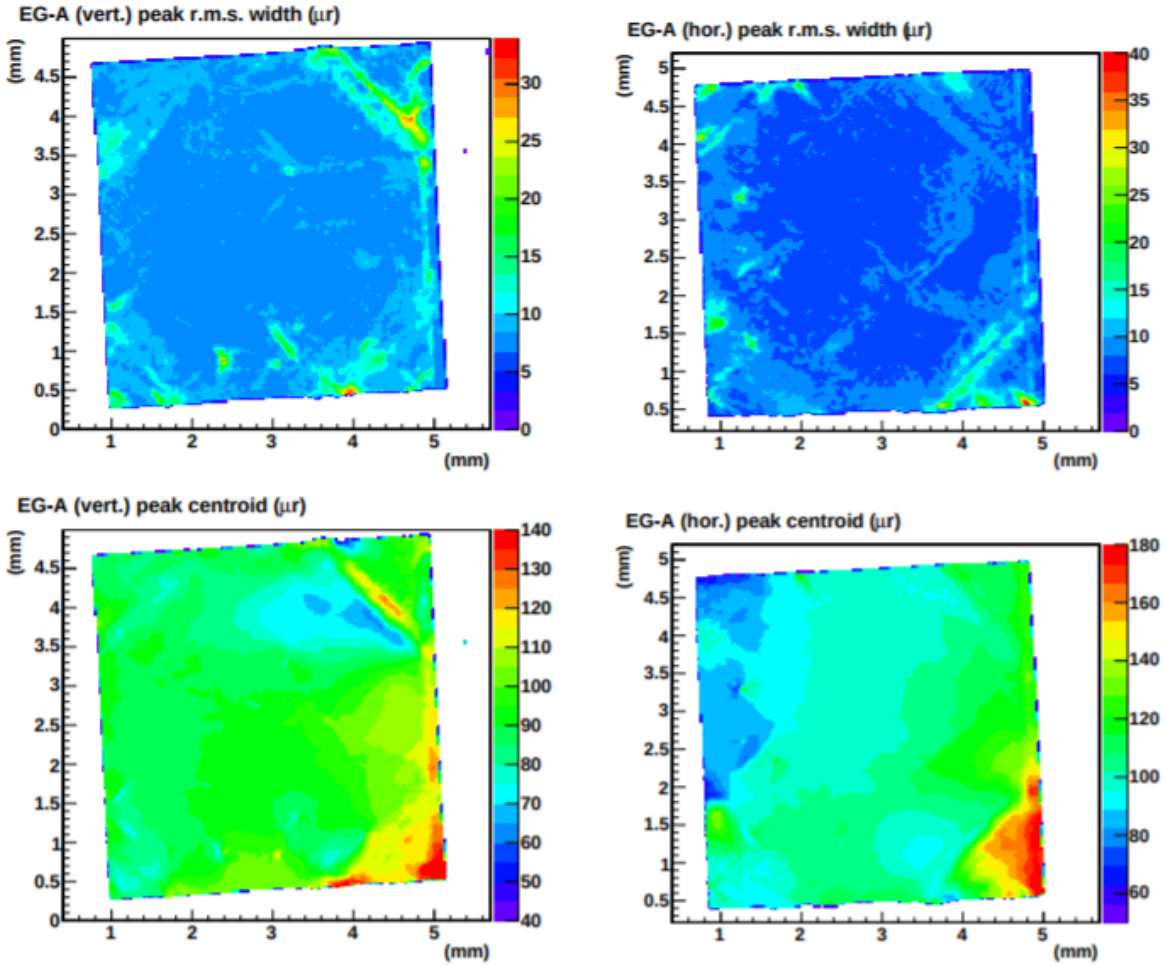

Figure 3.4: The top row shows plots of local rocking curve widths for an electron grade wafer in the vertical and horizontal scan orientations. The bottom row shows plots of the centroid of the local rocking curves. This diamond was 300 μm-thick and of very good quality.

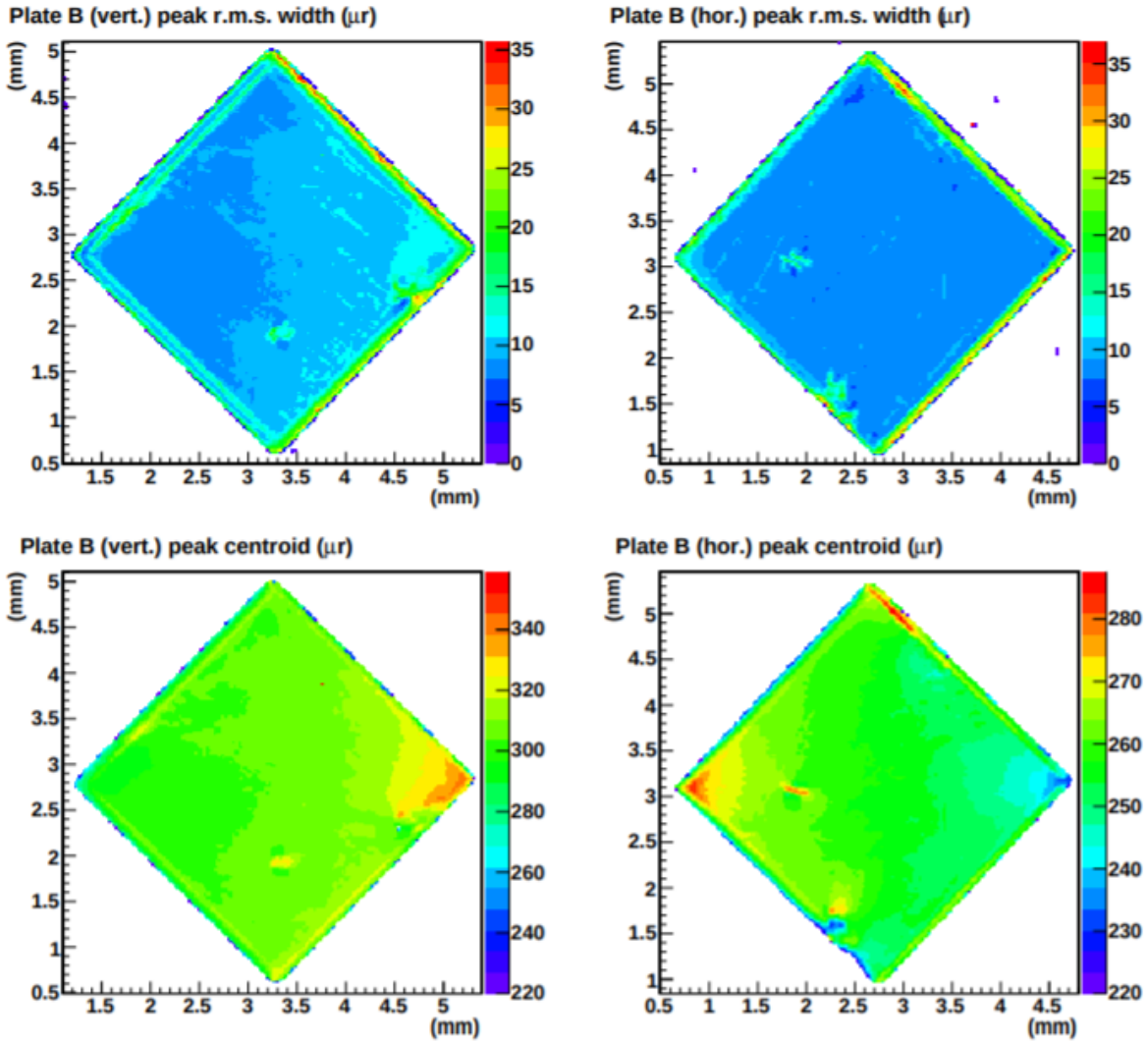

Figure 3.5: The top row show plots of local rocking curve width for the non-electron grade plate wafer, shown for the vertical and horizontal orientation scans. The bottom row show plots of the centroid of the local rocking curves examined in the vertical and horizontal scans. This thick, virgin sample clearly holds its normal to the scattering plane uniformly across its surface.

The significantly lower price of non-electronic grade single-crystal CVD diamond made it a preferred candidate for laser ablation. The rocking curve measurements in Fig. 3.5 indicate that these crystals are not only cheaper in price, but are also of comparable quality in terms of rocking curve width to the electronic grade crystals. These two factors are why non-

electronic grade CVD diamond was the material of choice for further radiator development studies using UV laser ablation.

3.2 Initial Results of Laser Ablated Diamond

Smaller area test samples were initially produced using the laser ablation facility at the University of Connecticut. The samples ranges in size, from $3 \times 3\ mm^2$ to $4.5 \times 4.5\ mm^2$ and various thicknesses, but were all the same non-electronic grade CVD material from Element Six. The smaller area allowed for the ablation of multiple diamond samples under varying conditions while minimizing sample cost. After many iterations, the first proof of concept radiator (U40) was laser ablated to a thickness of $40 \pm 2\ \mu$m. An image of the ablated sample is shown in Fig. 3.6.

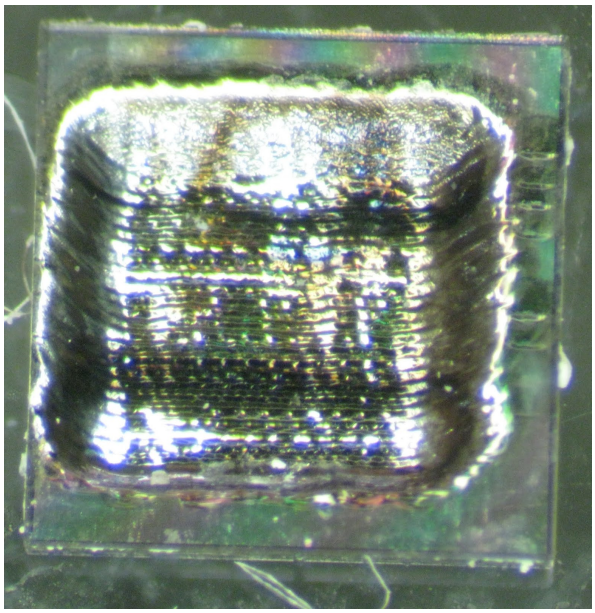

Figure 3.6: Photograph of diamond U40 after ablation. Notice the striations across the ablated surface from primitive raster pattern.

Rocking curve measurements were taken of the diamond U40 after laser ablation to measure the effect laser ablation had on the diamond's crystal lattice and are shown in Fig. 3.7a, Fig. 3.7b, and Fig. 3.7.

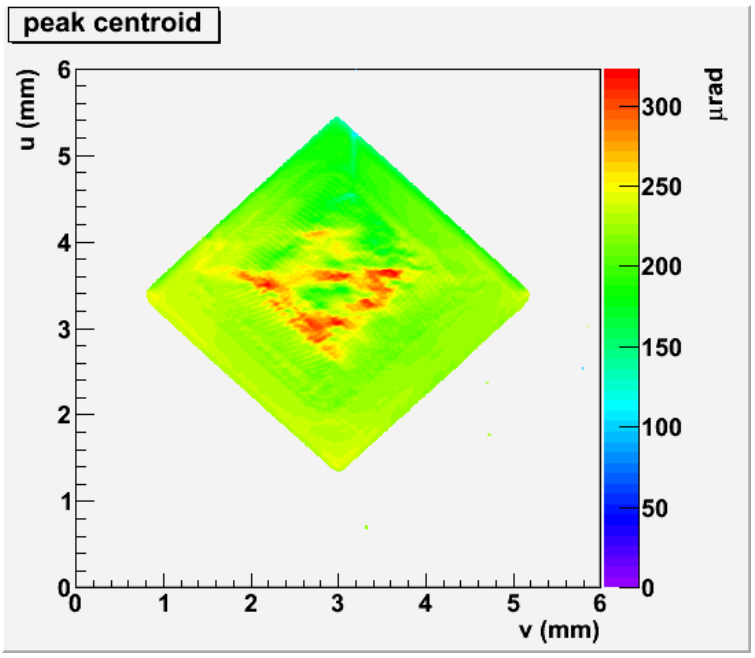

(a) 3.7a

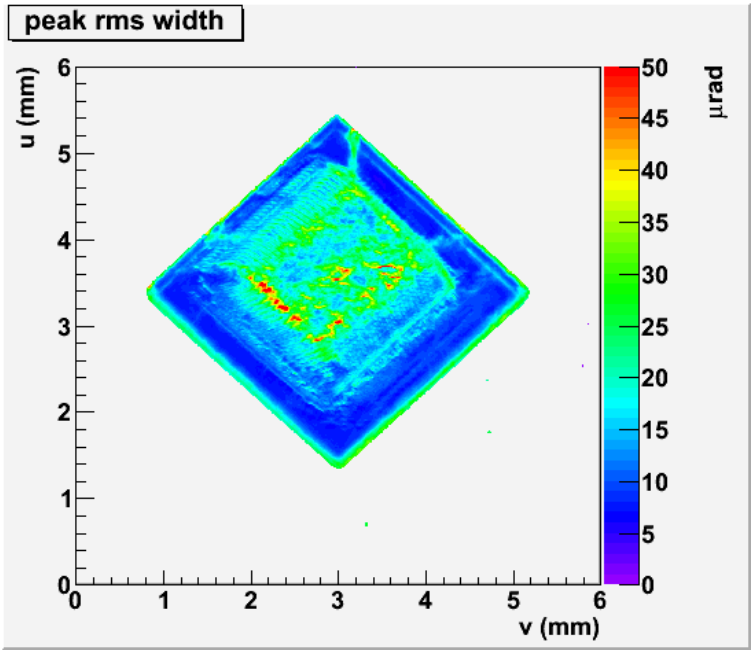

(b) 3.7b

Figure 3.7: Rocking curve measurements of 40 μm diamond U40 thinned using UV laser ablation. This was the first diamond differentially thinned to thicknesses close to 20 μm.

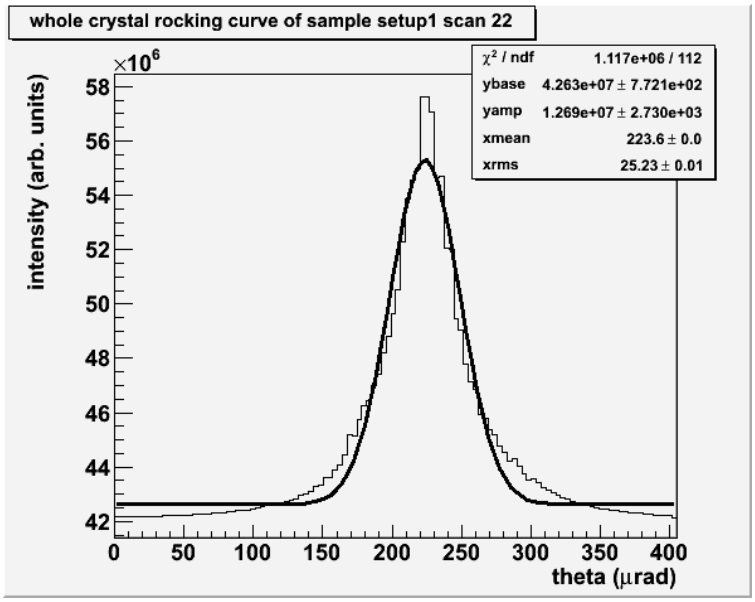

Figure 3.8: Whole-crystal rocking curve plot for diamond U40. The r.m.s. measures 25.33 $\pm$ 0.01 μm.

The peak centroid in Fig. 3.7a appears to show some local deformation in the central window, shown in red, but is overall very uniform. The framed region around the central window is completely uniform as expected. The sigma values shown in Fig. 3.7b also show some very localized non-uniformity in the central region. The whole-crystal rocking curve shown in Fig. 3.8 has a r.m.s. of 25.33 $\pm$ 0.01 μm. These measurements verified that UV laser ablation was capable of producing differentially thinned diamond radiators with central regions close to 20 μm while maintaining a whole-crystal rocking curve on the order of 20 μrad.

3.3 Large-Area Diamond Radiators

The next goal was to acquire large-area ($7 \times 7\ mm^2$) diamonds so that the ablation process could be extended to produce radiators of the correct size for the GlueX experiment. Non-electronic grade CVD diamond plates were purchased again from Element Six and measured at CHESS to make sure they had whole-crystal rocking curves well within the GlueX specification. Fig. 3.9 shows the mean and sigma rocking curve measurements for diamond JD70-2

which had dimensions of $7.08 \times 7.08 \times 1.208\ mm^3$. Both plots clearly show the pristine quality of these samples. Looking closely at Fig. 3.9b, some variation can be seen along the corners. This effect was seen in every large-area diamond studied and believed to be caused by growth boundaries created during the CVD crystal growth process. The whole-crystal rocking curve of this particular diamond was 10.71 ± 0.05 μrad as depicted in Fig. 3.10. All of the large-area samples obtained by Element Six had comparable whole-crystal rocking curves.

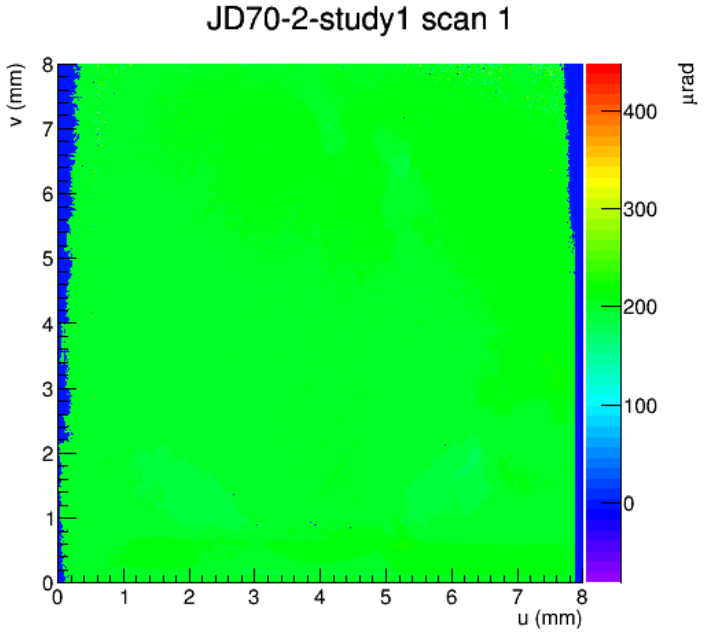

(a) 3.9a

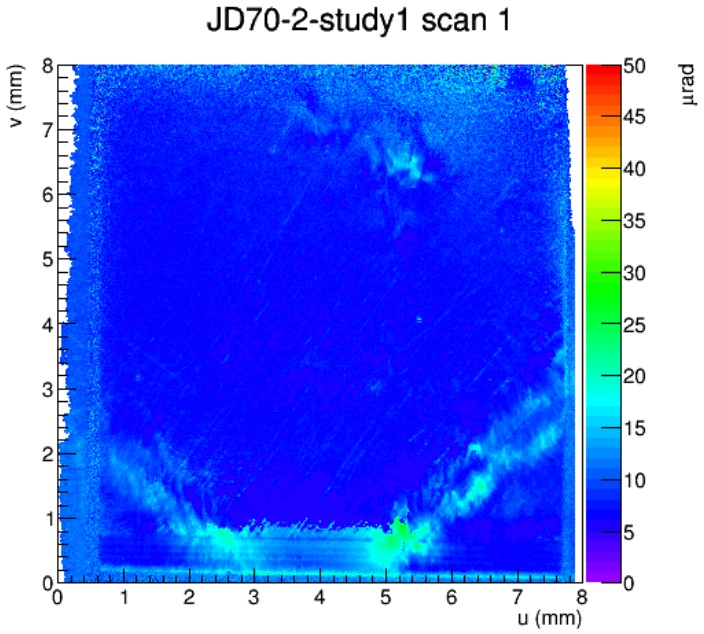

(b) 3.9b

Figure 3.9: Rocking curve measurements of 1208 ± 0.5 μm diamond JD70-2 purchased from Element Six. The very low variation across the diamond shows the high quality of the sample.

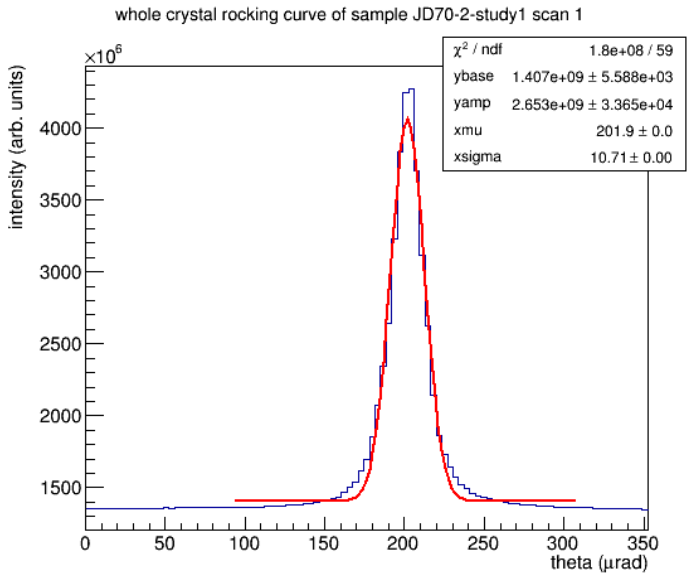

Figure 3.10: Whole-crystal rocking curve plot for diamond JD70-2.

While these crystals were of very qood quality and correct area, they were too thick to use as a starting point for laser ablation. Thinning a 20 μm central region in a diamond originally 1.208 mm thick would take upwards of 200 hours of continuous lasing. Ablating over such a long time frame would make it very difficult to maintain the required cut depth uniformity, and likely result in a final radiator with surface variations too large for GlueX. Two methods for thinning the diamond samples were explored. The first was a method of uniform thinning using vapor phase ion etching (VPIE) in collaboration with Sinmat Inc. who collaborated with us in many of these studies. A set of large-area samples were sent to Sinmat and etched using the VPIE technique. The diamonds were then returned to the University of Connecticut for study. Fig. 3.11 shows surface profile images of these diamonds that were taken at UConn using a Zygo surface profiling microscope. An attempt to UV laser ablate the diamond samples shown in Fig. 3.11a resulted in the cracking of the thin interior region. This occurred because the VPIE technique left surface variations as much as 20 μm deep. These pits and trenches made it impossible to reach the 20 μm required depth without cutting through the diamond. Clearly, VPIE resulted in thin diamonds which were not suitable for UV laser ablation.

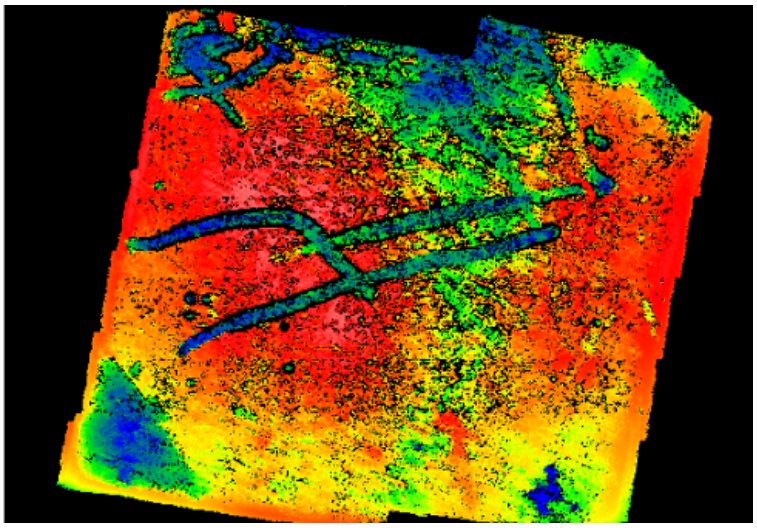

(a) 3.11a

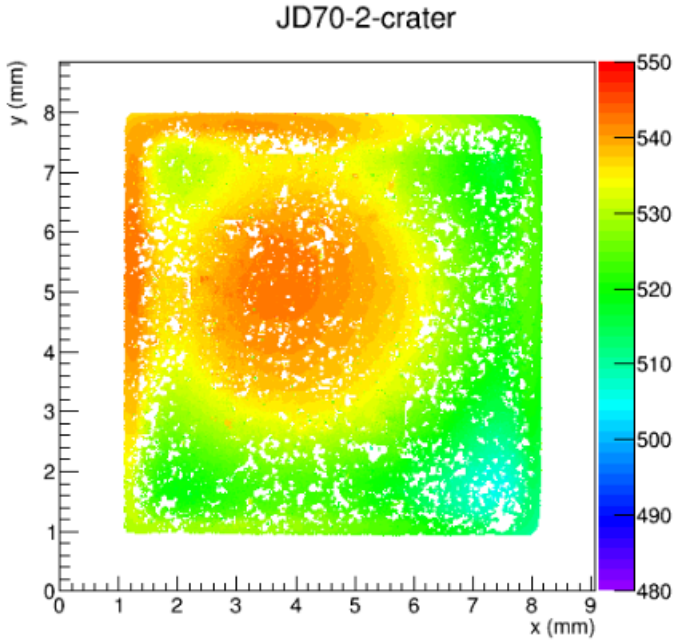

(b) 3.11b

Figure 3.11: Zygo images taken of two large-area diamond samples after thinning using vapour phase ion etching. Fig. 3.11a was the most damaged sample, and had 20 μm deep trenches cut along the surface as well as severe cracking along the edges. The sample JD70-2 shown in Fig. 3.11b appears to be in better condition, however there were pits across the entire surface, indicated by the voids in the image, reaching depths of up to 20 μm.

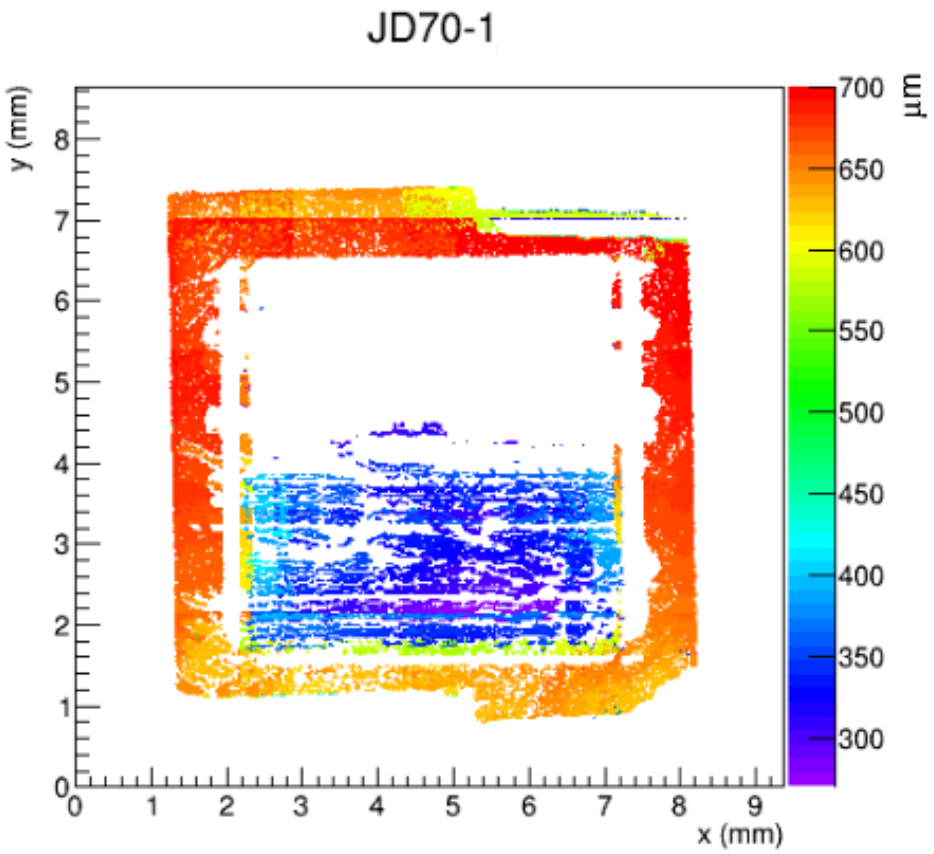

Figure 3.12: Zygo image of large-area diamond after an attempt to laser ablate the sample to 20 μm. The resulting cracked surface was a result of the deep pits made on the surface by the VPIE process.

A second sample of the large-area diamonds was sent to industrial diamond processing firm Applied Diamond, located in Wilmington, DE. Using their proprietary methods, a single diamond was "bread sliced" into three separate pieces. Each surface of the new pieces was polished using standard methods until they reached thicknesses ranging from 140 - 300 μm.

To ensure the process did not effect the crystal lattice, rocking curve measurements were taken of each sample again at CHESS. An example of one such diamond is shown in Fig. 3.13. The plots show the corner deformation that was intrinsic to every diamond from this lot, but very little variation from the original sample it was cut from. The whole-crystal rocking curve has a r.m.s. of less than 15 μrad and is shown in Fig. 3.14. The measurements taken at CHESS confirmed that the crystalline quality was maintained after the slicing procedure

which effectively tripled the number of diamonds available for use as radiators. It was for these reasons that the rest of the large-area thick diamonds were sent to Applied Diamond for slicing.

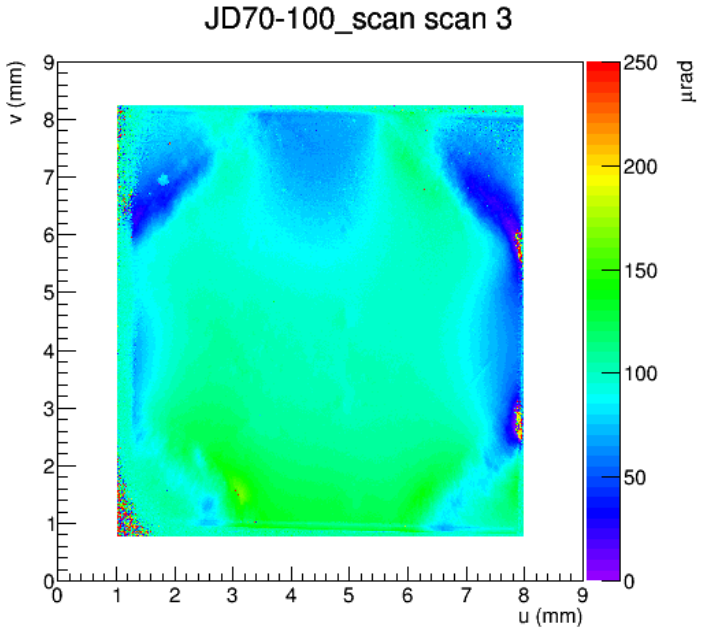

(a) 3.13a

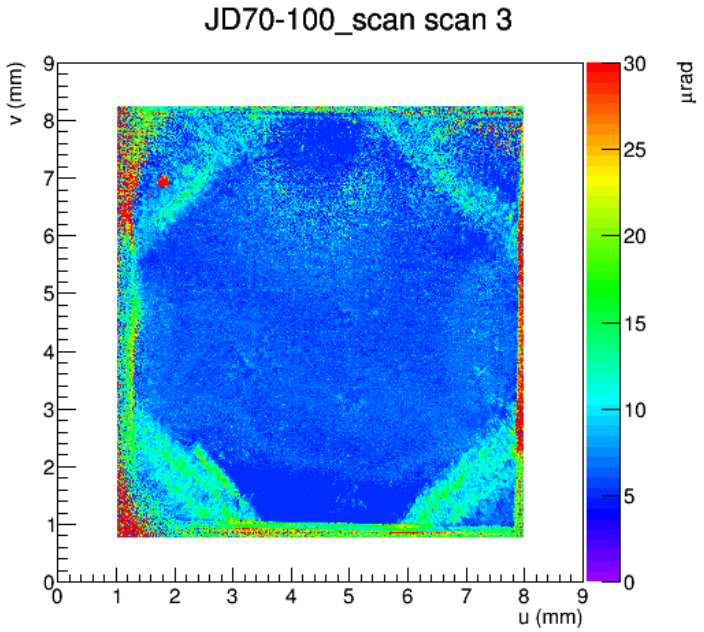

(b) 3.13b

Figure 3.13: Rocking curve measurements of large-area diamond sliced from thicker stock by Applied Diamond. The crystal quality has been maintained as can be seen by the low variation across the entire sample shown in Fig. 3.13a and Fig. 3.13b.

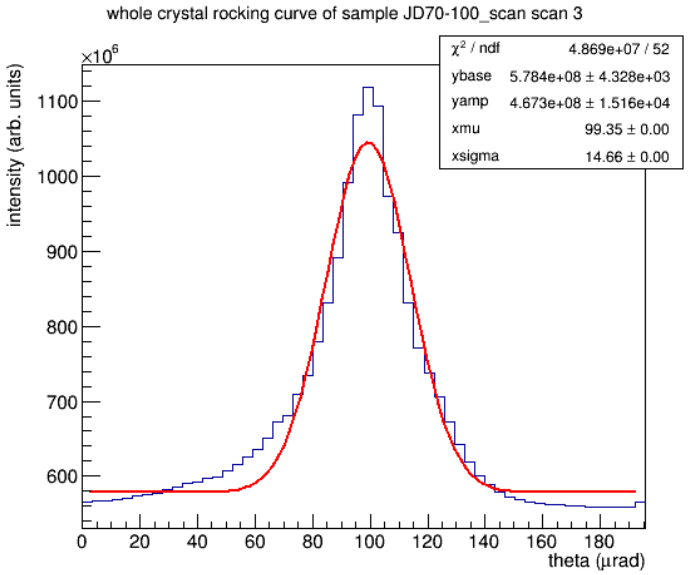

Figure 3.14: Whole-crystal rocking curve plot for diamond JD70-100 having an r.m.s. of 14.66 ± 0.0 μrad.

3.4 Results of the First 20 μm Large Area Diamond Radiators

Having over twenty large-area diamond plates in inventory was a necessity in the development of the UV laser ablation technique at the University of Connecticut. Many first attempts to ablate diamond to 20 μm resulted in the cracking of the thin central region. Each failure lead to more understanding of the diamond's response to ablation and overall refinement of the set up.

By the time these experiences culminated in the successful ablation of 20 μm diamond radiators, availability of beam time at CHESS for these measurements had declined, but a new opportunity had opened up at the Canadian Light Source to carry out these measurements there in collaboration with our colleagues at the University of Regina. The following samples were measured at the Canadian Light Source (CLS) in Saskatoon, SK Canada with a set up almost identical to that at CHESS.

After a number of unsuccessful attempts, the UV laser ablation setup at the University of Connecticut successfully processed diamond radiators to thicknesses of 20 μm. However,

it was found that the whole-crystal rocking curves of these radiators was orders of magnitude larger than the GlueX requirement. An example of one such measurement is shown in Fig. 3.20. The deformations in crystal lattice were believed to be a result of either residual non-diamond carbon bonded to the surface or micro-cracks along the steep walls which join the thick frame to the thin central region. Both of these issues might be relieved by removing material from the ablated surface. It was for this reason that a set of diamonds was ablated to thicknesses of roughly 35 - 38 μms and sent to Applied Diamond to be etched to the final 20 μm thickness.

The first diamond radiator processed in this way was laser ablated to a central thickness of 38 $\pm$ 0.5 μm using the UV laser ablation set up described in the previous section. A Zygo measurement of the thickness profile of the crystal is shown in Fig. 3.15 and displays the thick outer frame (in red) surrounding the thinned interior region (blue). The white surrounding the central region was sloped and unable to be measured by the instrument. The white voids within the central region indicate other areas where the Zygo interferometer saw insufficient reflected light intensity, presumably due to the slope of the surface. While these areas appear to be empty, they are not in fact holes in the diamond.

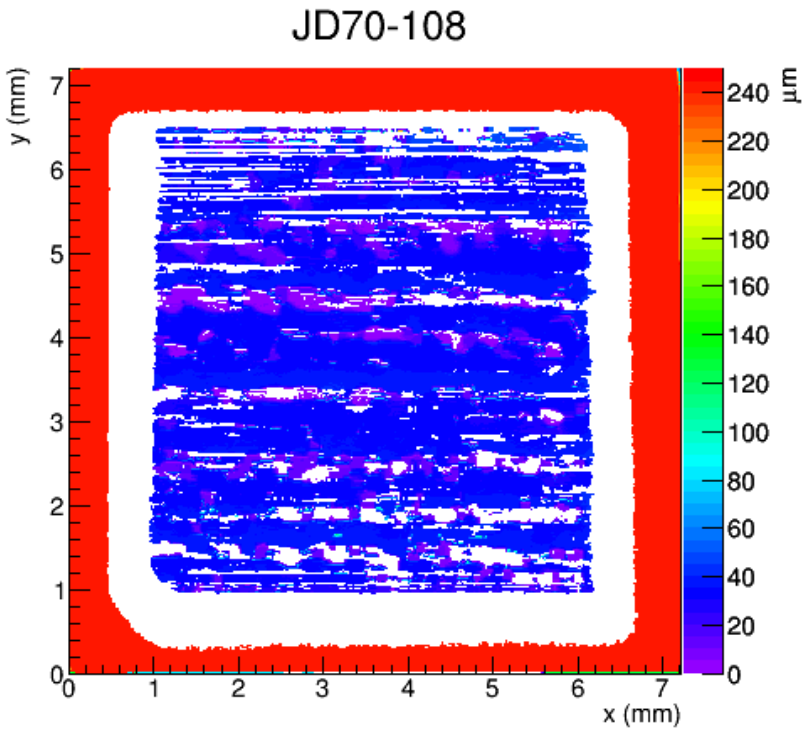

Figure 3.15: Zygo image of diamond JD70-108 after laser ablation. The central region of this diamond has an average thickness of 38 ± 0.5 μm.

Slices were made through the mid-point of the diamond thickness profile along the horizontal and vertical directions (Fig. 3.16a and Fig. 3.17a respectively) and the central zones were fit to a constant value. The average thickness of the diamond was taken as this value. The surface variation of these projections was measured by histogramming the values of the central regions and can be seen in Fig. 3.16b and Fig. 3.17b for the horizontal and vertical axis respectively. The histograms were fit to a Gaussian distribution and the sigma values are reported as the figure of merit for surface variation. Due to multiple scattering of the bremsstrahlung electron through the radiator, GlueX requires diamond radiators to have surface variations with an r.m.s. of less than 5 μm. The diamonds are ablated in a serpentine raster pattern where the laser is swept across the surface horizontally from edge-to-edge. This process results in a cut surface that is expected to be smoother along the horizontal axis versus the vertical. The measurements shown in Fig. 3.16b and Fig. 3.17b confirm this, but the r.m.s. along both axes of this ablated diamond meet the GlueX requirement.

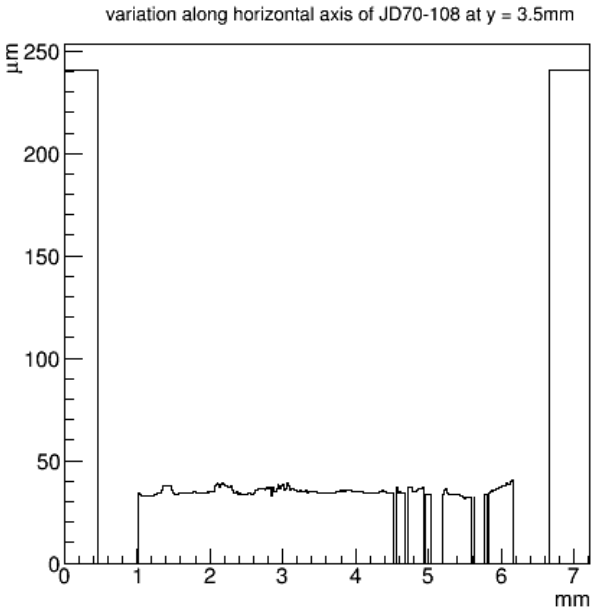

(a) 3.16a

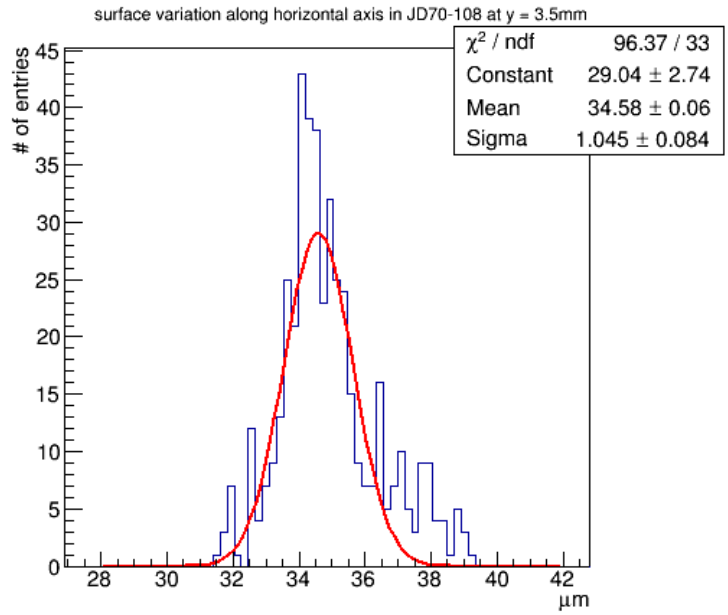

(b) 3.16b

Figure 3.16: Panel a (upper) shows the cross sectional cuts along the horizontal axis of the thickness profile for diamond sample JD70-108. Panel b (lower) shows the histogram of the central region from the above plot which show the total surface variation. Each histogram was fitted with a Gaussian distribution and the sigma value was quoted as the figure of merit for the diamond's surface roughness. After the ablation process, the diamond had surface variations of 1.0 $\pm$ 0.1 μm in the horizontal direction (along the direction the laser was swept.

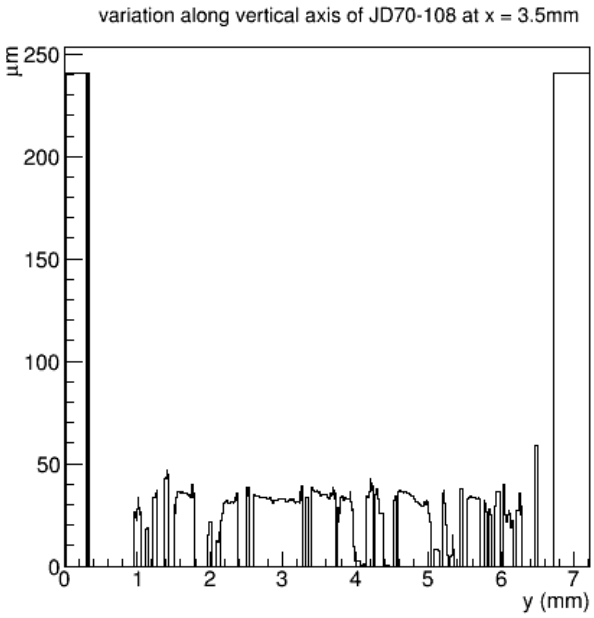

(a) 3.17a

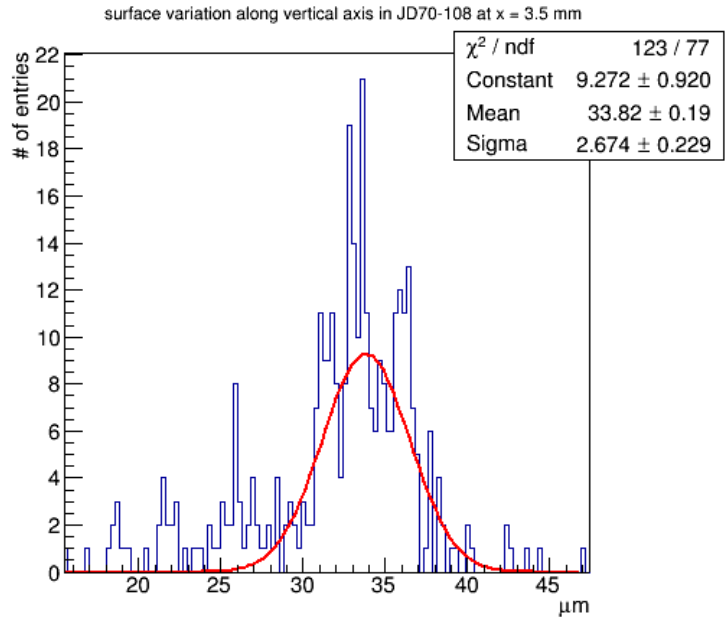

(b) 3.17b

Figure 3.17: Panel a (upper) shows the cross sectional cuts along the vertical axis of the thickness profile for diamond sample JD70-108. Panel b (lower) shows the histogram of the central region from the above plot which show the total surface variation. The histogram was fitted with a Gaussian distribution and the sigma value was quoted as the figure of merit for the diamond's surface roughness. After the ablation process, the diamond had surface variations of 2.7 $\pm$ 0.2 μm in the vertical.

Diamond JD70-108 was sent to Applied Diamond where the central region was etched to an average total thickness of 18 $\pm$ 0.5 μm. The diamond was processed using a mask, such that the sloped walls and outer frame of the crystal were not etched. X-ray rocking curve measurements were taken at CLS and are shown in Fig. 3.18. The rocking curve measurements show large amount of strain in the corners of the central region in the diamond. The concentration of strain in these "pockets" suggest that the entire thinned window is bending such that the edges of the thinned region exhibit the most strain.

The whole-crystal rocking curve of JD70-108 shown in Fig. 3.20 has a sigma of roughly 160 μrad, which is eight times the GlueX requirement. This indicated that the etching process had made little improvement on the diamond's whole-crystal rocking curve. During visual inspection of the crystal's back surface, a curvature was apparent. The diamond was imaged using the Zygo white-light interferometer and the results are shown in Fig. 3.21. It is clear from these images that the thin central region was curved, which agreed with the rocking curve results from CLS.

It was considered that a major source of strain observed in JD70-108 was found in the side walls of the ablated diamond which were masked during the etching process. During ablation, this portion of the diamond was cut indirectly by the tails of the focused laser pulses. These tails may not have had enough energy to ablate the material, instead removing material through a graphitization process resulting in crystal damage within the diamond. Such damage could lead to an imbalance of forces on the thick diamond frame, ultimately resulting in the bending of the entire crystal. Etching the entire surface uniformly may alleviate these stresses.

A second large-area diamond, JD70-104, was ablated to a thickness of 38 $\pm$ 0.5 μm and etched by Applied Diamond over the entire surface to a final thickness of 17 $\pm$ 0.5 μm. A Zygo image was taken of the diamond after the ablation and etching process and is shown in Fig. 3.22. The slices along the horizontal and vertical axis and their average surface

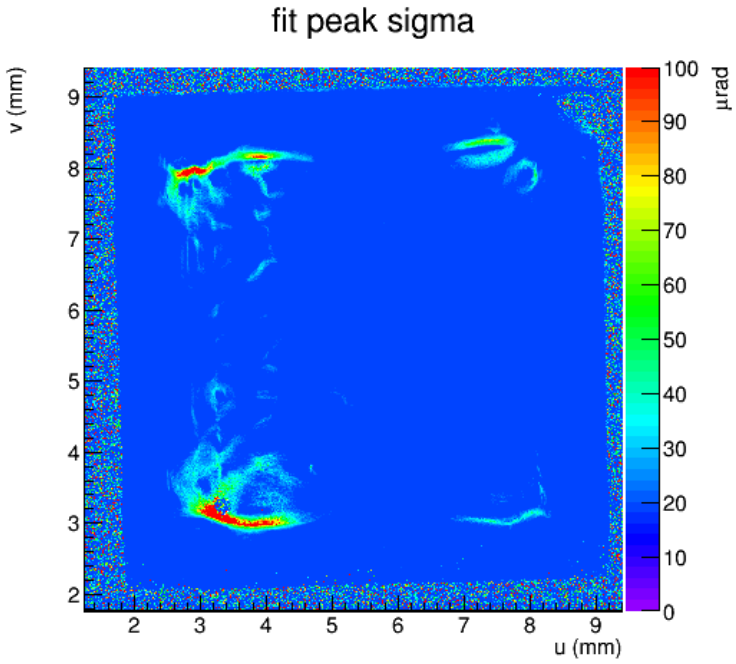

(a) 3.18a

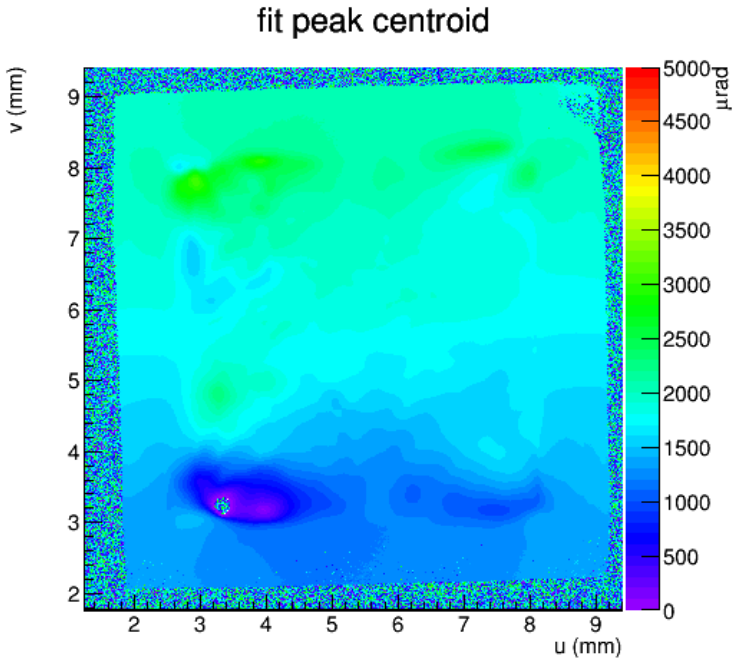

(b) 3.18b

Figure 3.18: Rocking curve measurements of 18 ± 0.5 μm diamond JD70-108 thinned using UV laser ablation and etched by Applied Diamond. This was the first diamond to be UV laser ablated and later etched by Applied Diamond.

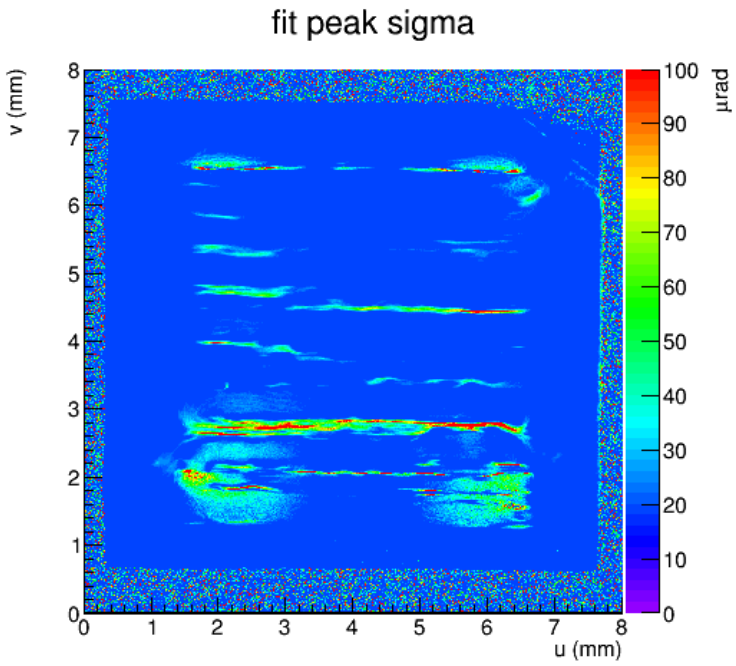

(a) 3.19a

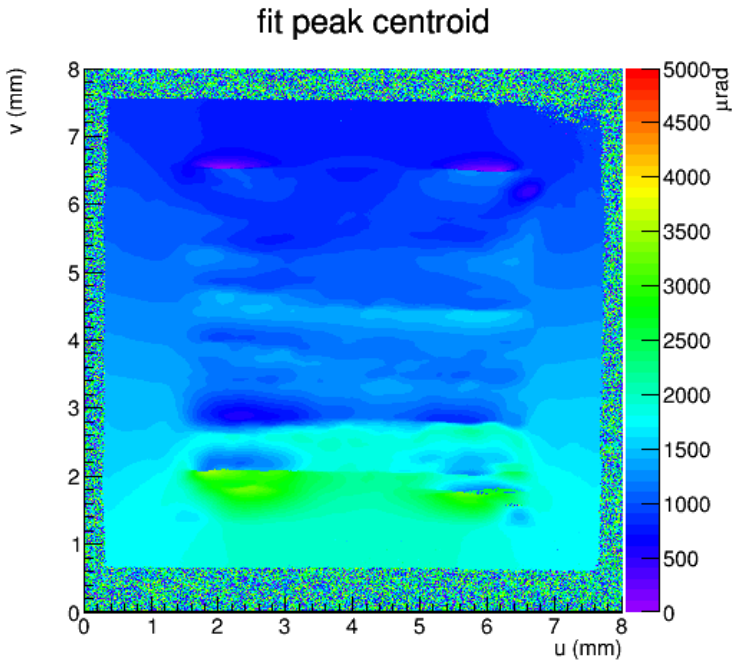

(b) 3.19b

Figure 3.19: Rocking curve measurements of 18 $\pm$ 0.5 μm diamond JD70-108 thinned using UV laser ablation and etched by Applied Diamond after being rotated in ϕ by 180° in the X-ray goniometer. This was the first diamond to be UV laser ablated and later etched by Applied Diamond.

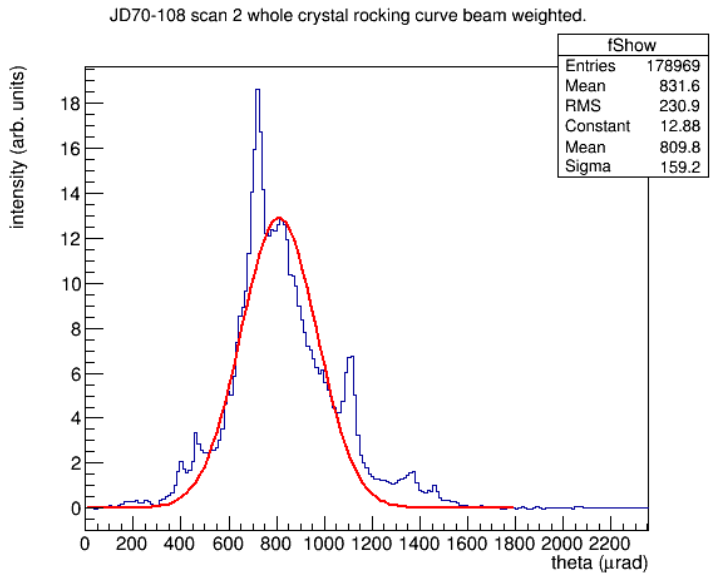

Figure 3.20: Whole-crystal rocking curve of diamond JD70-108. The r.m.s. is clearly above the GlueX requirement.

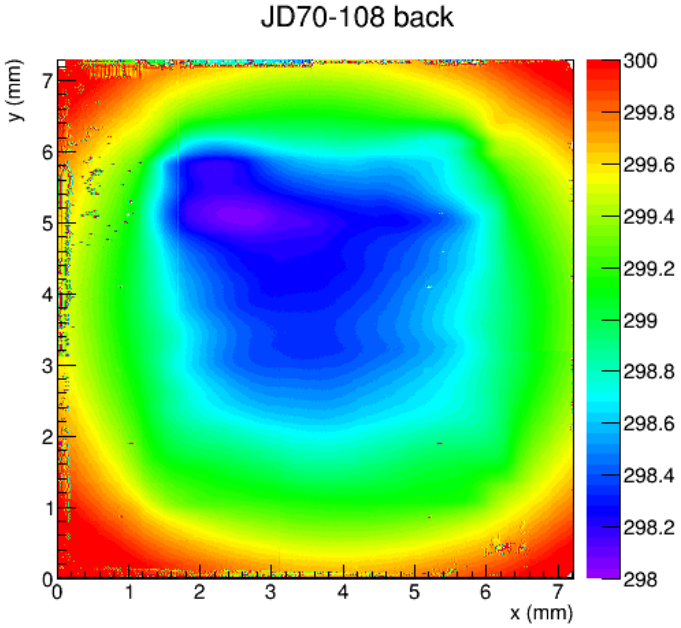

Figure 3.21: Zygo image of the back surface of JD70-108. Note the large amount of deflection present in the center of the crystal.

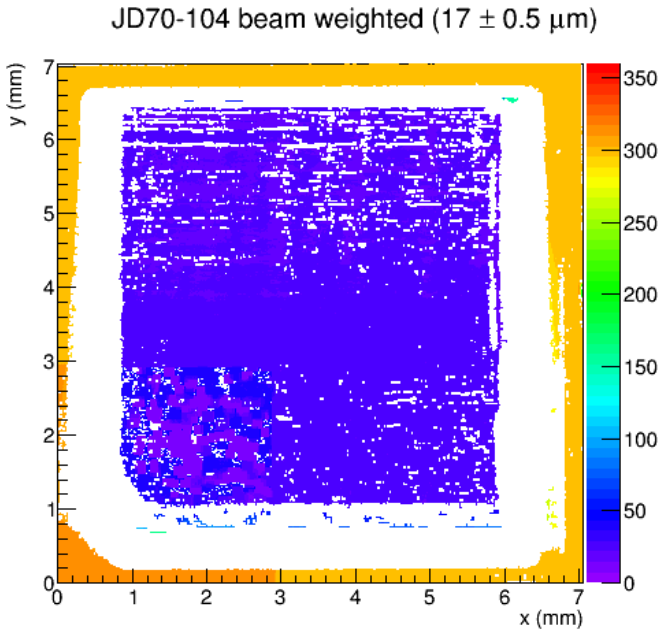

Figure 3.22: Zygo image of large-area diamond sample JD70-104 which was laser ablated to have a central thickness of 35 ± 0.5 μm and then etched to a final thickness of 17 ± 0.5 μm by Applied Diamond.

variations are shown as well. As in the case of diamond JD70-108, the ablation process left the crystal with thickness variation less than the GlueX requirement.

The diamond's whole-crystal rocking curve was measured at CLS and is presented in Fig. 3.27. The results show the same pockets of strain as before with JD70-108, however, the magnitude of these deformations was considerably lower. Etching uniformly across the ablated surface of the diamond appeared to reduce the strain present in the crystal. The sigma plots (Fig. 3.25a and Fig. 3.26a) show bands on the thick diamond frame that have locally broad rocking curves. This is surprising because the purpose of the frame was to keep the diamond rigid. If the frame is bending, as the data show, then it is not able to support the thin diamond in a uniform, flat geometry.

In summary, producing 20 μmm thin diamond radiators of adequate area and planarity is a very challenging task. The following description summarizes the state of the art at the time this thesis was written. UV laser ablation of diamond was conducted using an excimer laser operating at 193 nm. A large-area 7.06 × 7.06 × 0.26 mm^3 CVD diamond was held

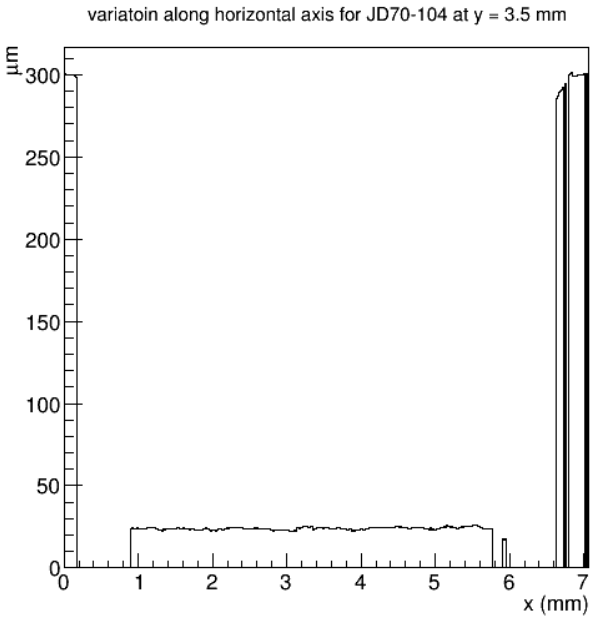

(a) 3.23a

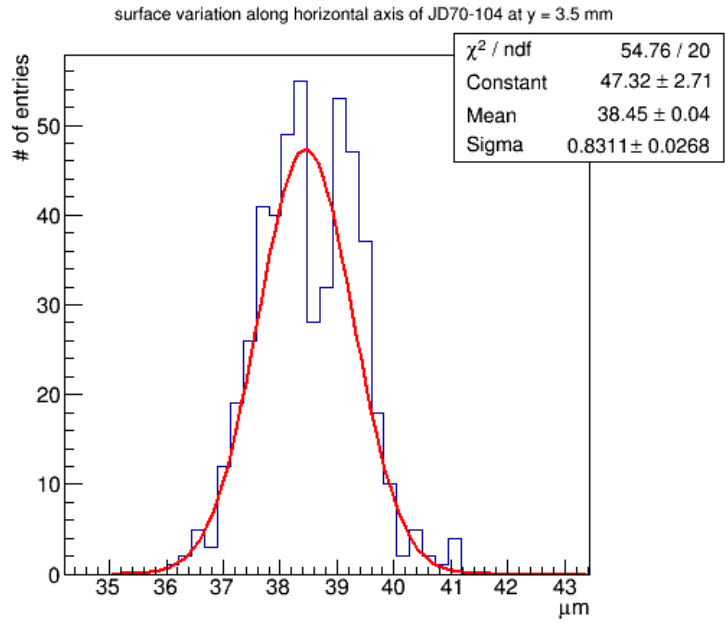

(b) 3.23b

Figure 3.23: Top: Cross sectional cuts along the horizontal axis after JD70-104 was etched by Applied Diamond to an average thickness of 17 ± 0.5 μm. Panel a (top) shows a histogram of the central region from the above plot. The histogram was fitted with a Gaussian distribution and the sigma value was quoted as the figure of merit for the diamond's surface roughness. After the etching process, the diamond had surface variations of 0.83 ± 0.03 μm in the horizontal direction. There was a small increase in surface roughness after the etching process.

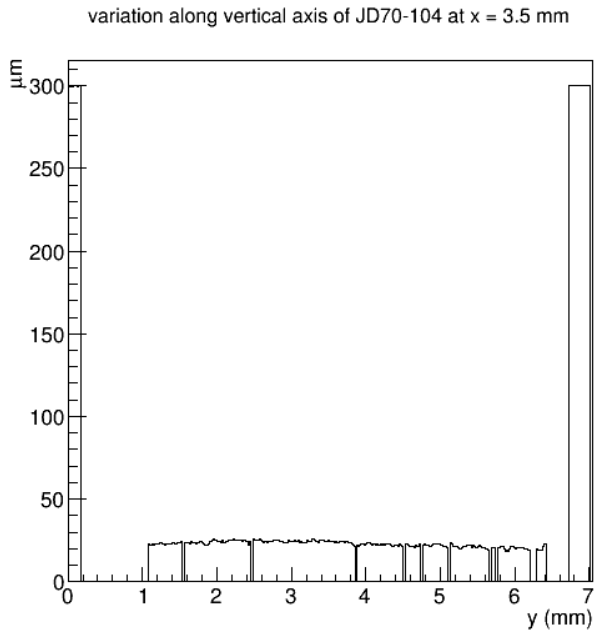

(a) 3.24a

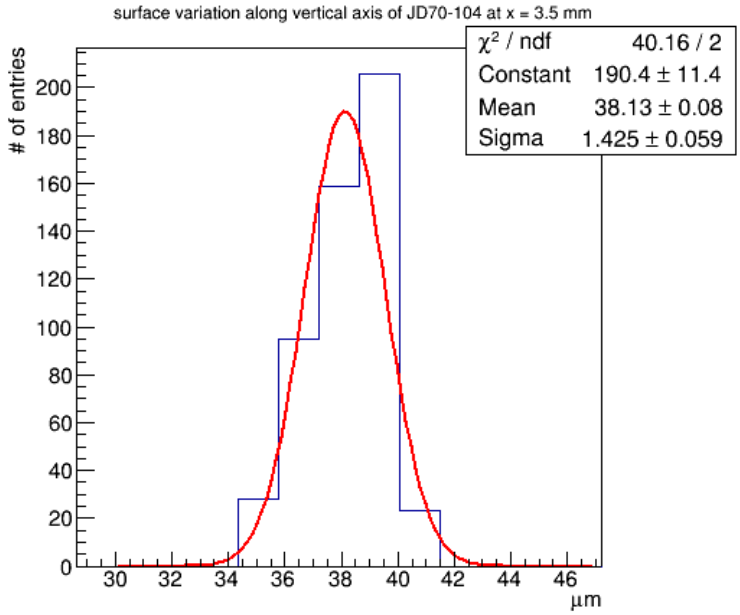

(b) 3.24b

Figure 3.24: Top: Cross sectional cuts along the vertical axis after JD70-104 was etched by Applied Diamond to an average thickness of 17 ± 0.5 μm. Panel b (bottom) shows a histogram of the central region from the above plot. The histogram was fitted with a Gaussian distribution and the sigma value quoted as the figure of merit for the diamond's surface roughness. After the etching process, the diamond had surface variations of 1.43 ± 0.06 μm in the vertical. There was a small increase in surface roughness after the etching process.

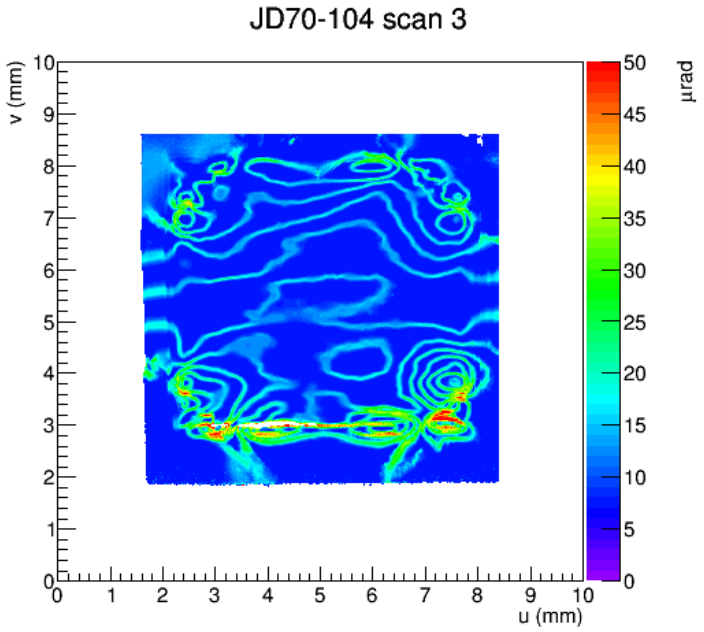

(a) 3.25a

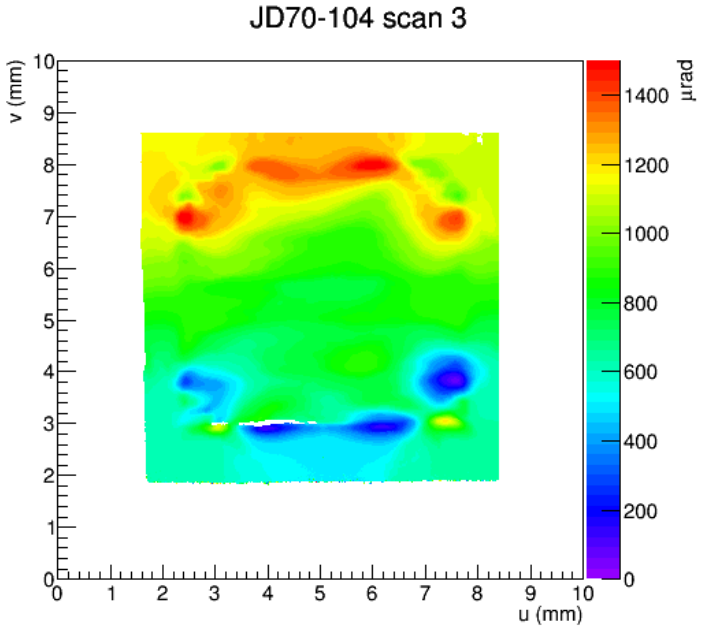

(b) 3.25b

Figure 3.25: Rocking curve measurements of diamond JD70-104 showing the variations in parameters sigma (top) and mean (bottom). This diamond was first laser ablated to a central thickness of 35 μm and then etched to a final thickness of 17 $\pm$ 0.5 μm.

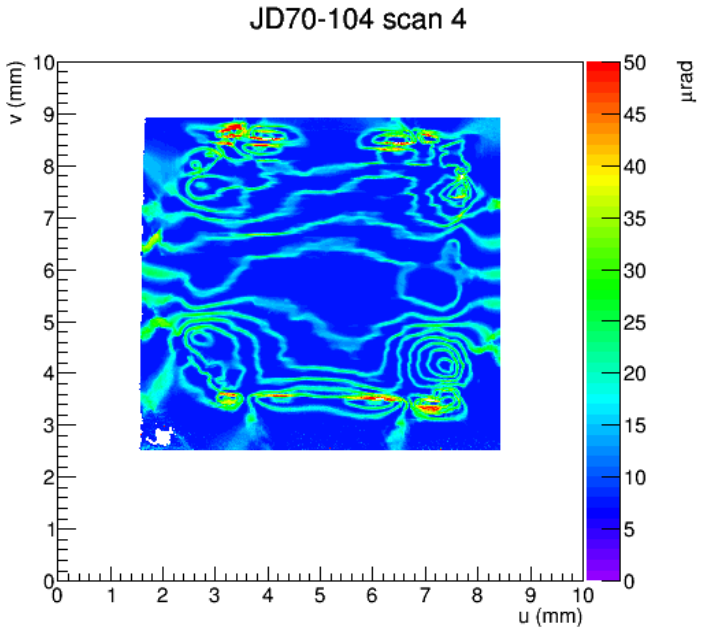

(a) 3.26a

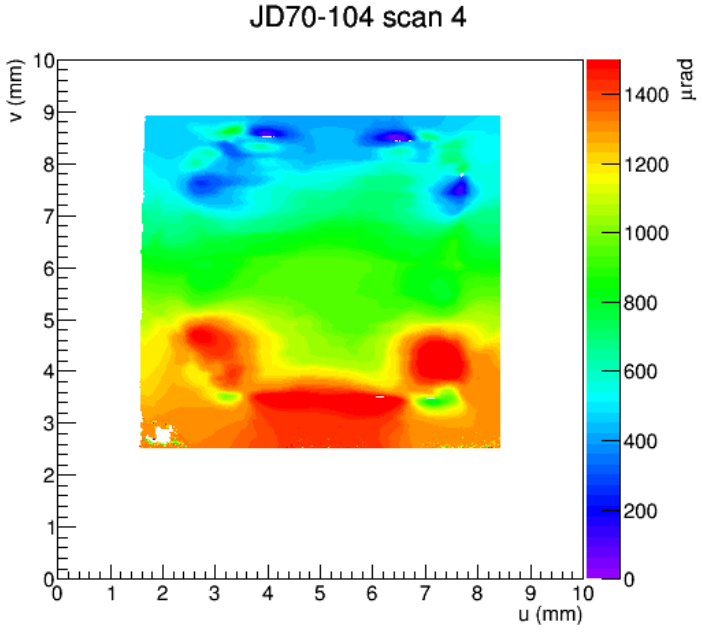

(b) 3.26b

Figure 3.26: Rocking curve measurements of diamond JD70-104 showing the variations in parameters sigma (top) and mean (bottom) after rotation in ϕ 180°. This diamond was first laser ablated to a central thickness of 35 μm and then etched to a final thickness of 17 $\pm$ 0.5 μm.

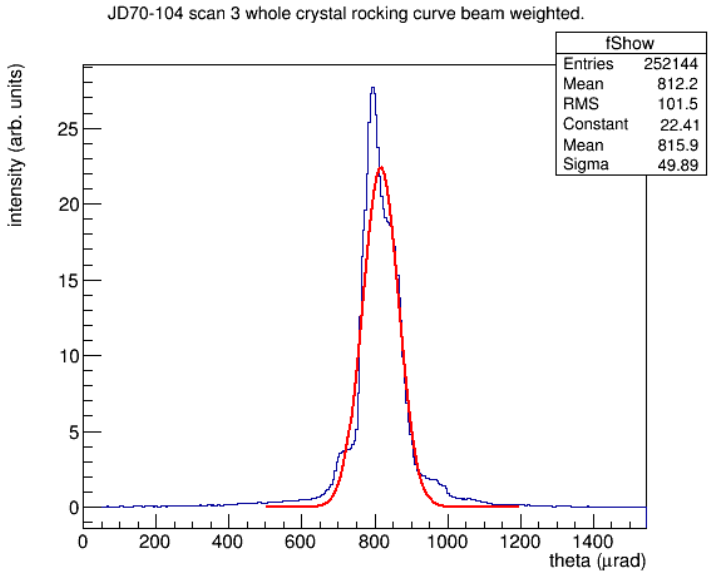

Figure 3.27: Whole-crystal rocking curve plot for diamond JD70-104. The r.m.s. measures 49.9 ± 0.05 μrad. The first large area diamond thinned using laser ablation to have a whole-crystal rocking curve close to the GlueX requirement.

under vacuum and a sequence of laser pulses were rastered over its surface until a 6.2 × 6.2 mm^2 rectangle of thickness 38 ± 0.5 μm was achieved. The ablation rate in diamond was measured as a function of laser energy and used to control the rate of material removed for the sample studied. Zygo white-light interferometry measurements show the total surface variation of the ablated region met the GlueX specifications and had a r.m.s. less than 2 μm. The quality of crystal surface and ability to thin diamond differentially make it a viable method for thin diamond radiator production. Rocking curve measurements reveal both the bulk and internal structure of the diamond radiator. Our studies showed that the ablation process does not appreciably affect the internal structure of the diamond, but it does leave behind large-scale strain patterns that contribute significantly to the whole-crystal rocking curve width. In particular, the stress along the corner edges of the sample suggest the thin diamond membrane is buckling due to some strain in the crystal. The presence of broad rocking curve widths in the diamond frame is also a potential source of strain. It is unclear why the frame is not able to maintain planarity, but it may be alleviated by increasing its width. The rocking curve peak position measurements indicate the bending of the crystal is

the largest contribution to the rocking curve width. In the beset sample produced so far, the whole-crystal rocking curve width is within a factor of 2.5 of the GlueX specification. It is likely that with a slightly wider outer frame the method of UV laser ablation would produce diamond radiators that would meet all of the requirements of the GlueX experiment.

CHAPTER 4

Performance of Diamond Radiators

A set of the diamond radiators were thinned by the author using the laser ablation technique described in the previous chapter, and installed in the GlueX Hall D goniometer as shown in Fig. 4.1. The mount was designed by the author based on Monte Carlo simulations, with the aim to minimize the background radiation produced by the CEBAF electron beam in the mounting material. The *dog ear* of each diamond was epoxied (Loctite 29840 3888 Thermally Conductive Epoxy Adhesive) to an aluminum tab for easy installation/removal. The radiators were installed in the goniometer and GlueX began taking data in the fall of 2014 to commission the newly constructed and installed detectors. Once the detectors were properly commissioned, physics quality data could be taken. However, during the spring 2015 run a quench in the solenoid resulted in only 3 hours of usable data generated during the entire run period. Unfortunately, none of these data were taken while a laser ablated diamond was installed as the radiator. Instead, a 50 μm radiator was used (J1a50) which had a very narrow whole-crystal rocking curve. Before the quench, the plan was to take initial data with the slightly thicker radiator with the best rocking curve available, and then introduce the laser ablated crystals as the run progressed. This second step did not occur during this particular run period.

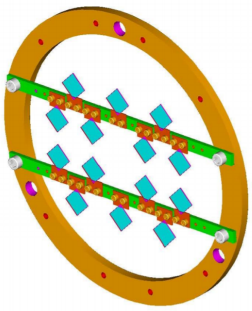

(a) 4.1a

(b) 4.1b

Figure 4.1: Left: CAD rendering of aluminum ring machined to hold diamond radiators in the GlueX goniometer. Right: Picture of actual diamond radiators mounted in the GlueX goniometer.

4.1 Analysis of $\gamma p \to \pi^+\pi^- p$

4.1.1 Introduction

The final project the author contributed to was the analysis of the neutral ρ vector meson via the dominant decay channel:

$$\gamma p \to \pi^+\pi^- p \tag{4.1}$$

The analysis was carried out using the 26 billion physics triggers collected during the GlueX spring 2016 run period. The diamond radiators were mounted in the GlueX goniometer and aligned using a method developed by Ken Livingston [21]. Data was taken with the radiator in two orientations, parallel (PARA) and perpendicular (PERP), which correspond to the direction of the photon's linear polarization with respect to the experimental floor.

Due to unforeseen complications, the only radiator used during this period was a 50 μm (uniform thickness) single-crystal HPHT-1a diamond called J1a50. This radiator, although twice the thickness of the GlueX specification, had a very narrow whole-crystal rocking curve and thus, low mosaic spread. It was for these reasons that the collaboration decided to use this radiator during the initial run period, so that the crucial commissioning data would be taken under conditions that are as simple as possible to analyze. A subsequent run with a thinner radiator was planned to study the polarization of the photon beam created using diamond JD70-104, which was the highest-quality diamond radiator produced using the laser ablation method described throughout this thesis, but this did not happen in 2016. While the lack of these commissioning data with thin radiators is unfortunate, the analysis described below can be easily applied to the data collected from the thin diamond radiators, once they become available.

4.1.2 Angular Distribution of ρ Vector Meson Decay

The azimuthal dependence of the cross section of π^+ and π^- mesons produced via photoproduction using a linearly polarized photon beam is given by:

$$\sigma = \sigma_0(1 - P_\gamma A \cos 2(\phi_{\pi^+} - \phi_\gamma^{lin})) \tag{4.2}$$

where σ_0 is the unpolarized cross section, A is the linearly polarized beam asymmetry, and ϕ_{π^+} is the azimuthal angle of the ρ production plane defined by the final-state π^+ [22]. Extending this to the PARA and PERP orientations detailed above, the yields are given by:

$$Y_\parallel \propto N_\parallel(1 - P_\parallel A \cos 2\phi) \tag{4.3}$$

$$Y_\perp \propto N_\perp(1 + P_\perp A \cos 2\phi) \tag{4.4}$$

A visual representation of the photon beam polarization plane, the ρ decay plane and the ϕ angle between them is shown in Fig.

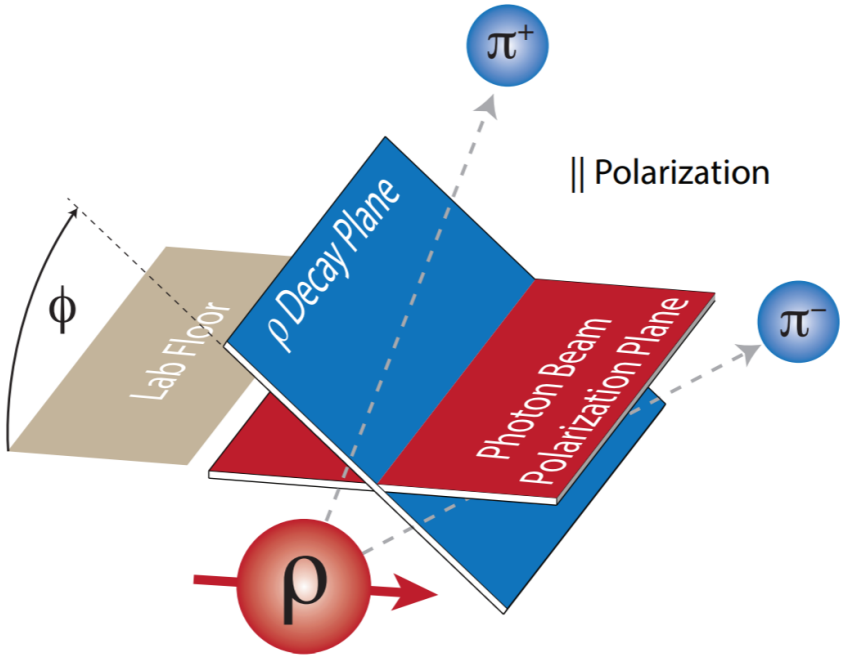

Figure 4.2: Illustration of the ρ decaying into π^+ π^-. The photon beam is in the PARA orientation, where the electric field vector is parallel to the floor of the experimental hall. The angle ϕ is the difference between the polarization plane and the decay plane.

The two orientations (PARA and PERP) of the photon beam are orthogonal to each other, which causes cancellation of any ϕ-dependent instrumental acceptance through a measurement of the yield asymmetry as follows [22]:

$$\frac{Y_\perp - F_R Y_\parallel}{Y_\perp + F_R Y_\parallel} = \frac{(P_\perp + P_\parallel) A \cos 2\phi_p}{2 + (P_\perp - P_\parallel) A \cos 2\phi_p} \tag{4.5}$$

where $F_R = N_\perp / N_\parallel$ is the ratio of the integrated photon flux between PERP ($N_\perp$) and PARA ($N_\parallel$). Using this method, the product of the beam asymmetry (A) and the polarization ($P_\perp or P_\parallel$) can be extracted from a fit to measured decay angular distributions [22]. The following sections detail the techniques used to extract a clean ρ signal and a discussion of the results including the measurement of spin density matrix elements (SDMEs) aided by Monte Carlo (MC) acceptance corrected simulations.

4.1.3 Event Selection

The GlueX collaboration has an extensive software package for the analysis of physics data collected from each detector. This package includes a particle reconstruction component which, based on very loose restrictions, sorts through the data and builds what are called event hypotheses. An event hypothesis is a possible sequence of particle interactions and decays that explain what caused the signals recorded by the detector when a particular trigger fired. This decay channel restricts, for example, the number and sign of charged particles for the events of interest. These events are stored in structured data files called ROOT trees which are later analyzed over by what is called a DSelector. The DSelector is where higher-level cuts (such as missing-mass squared) are applied, custom histograms are filled and any other calculation specific to the analysis is performed. The following section describes the series of cuts placed on the event hypotheses data for the reaction shown in Eq. 4.1.

The large set of data recorded during the spring 2016 production run was first reduced by running it through the event reconstruction library. In the analysis described here, all

retained event hypotheses were required to contain two positively charged reconstructed tracks and one negative (π^+, π^- and proton). It also was required that there be one tagged beam photon so that a single unique combination could be made. A kinematic fit was used to fit the reconstructed tracks to a common vertex, incorporating the four-momentum of the reconstructed final state particles as constraints. The kinematic fit was required only to converge at this stage of the analysis.

As previously discussed, the electron beam comes in 4 ns RF bunches from CEBAF. A requirement in the reconstruction restricted events to fall within a time window $|t_{event} - t_{RF}| <= 6.5 \times \tau)$ where τ is the beam period (4.008 ns for this data set) and t_{RF} is the time from the accelerator clock (also known as the RF time). This may appear to be a large time window, however, the length was used in a later analysis step to perform accidental subtraction. A further constraint was made on the *missing mass* which is restricted to the range of ± 0.1 GeV. Due to the GlueX detector's excellent timing resolution, cuts can be made for each candidate, the π^+, π^-, and proton as seen in Fig. 4.3, Fig. 4.4, and Fig. 4.5.

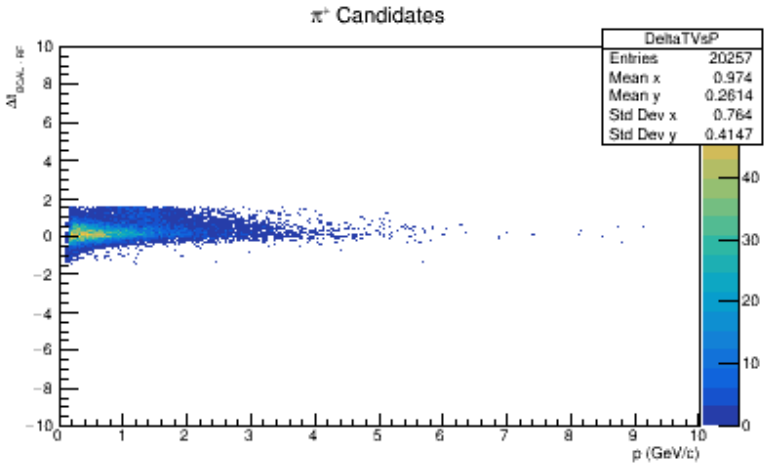

(a) 4.3a

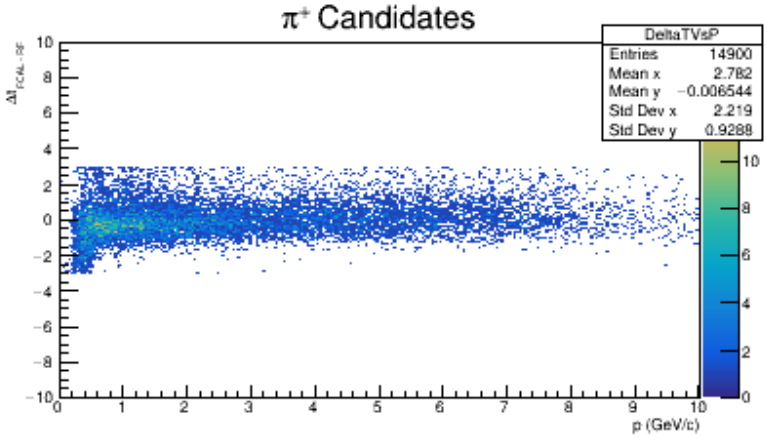

(b) 4.3b

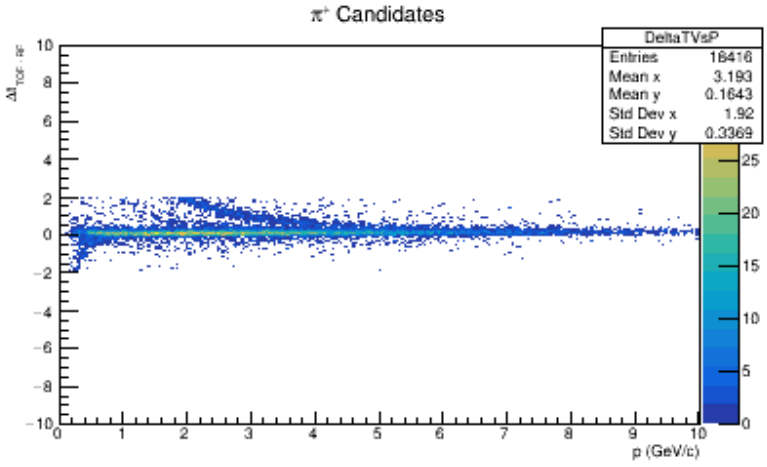

(c) 4.3b

Figure 4.3: π^+ Δt cuts in the BCAL, FCAL, and TOF. Panel a shows the BCAL cuts events with $\Delta t \leq |1.5|$. Panel b shows the FCAL cuts events with $\Delta t \leq |3.0|$. Panel c shows the BCAL cuts events with $\Delta t \leq |2.0|$

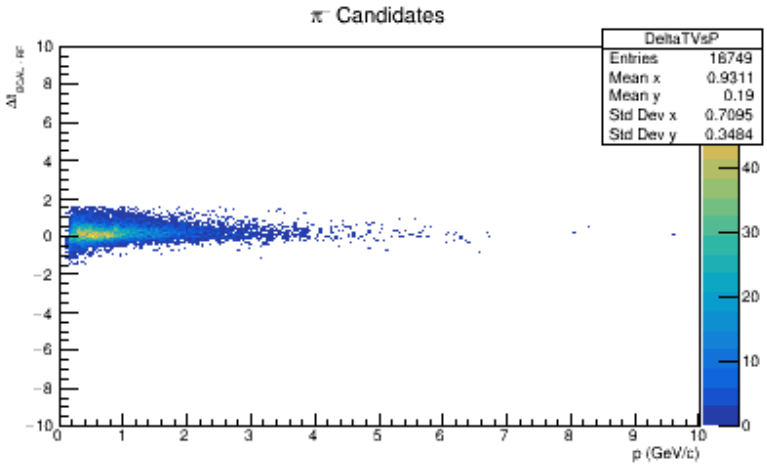

(a) 4.4a

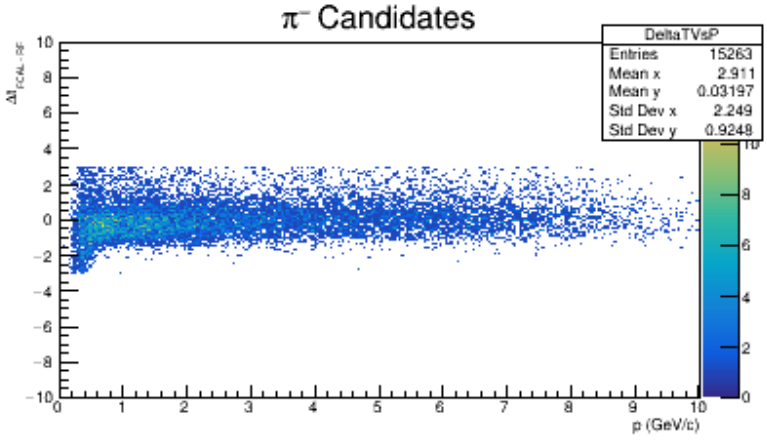

(b) 4.4b

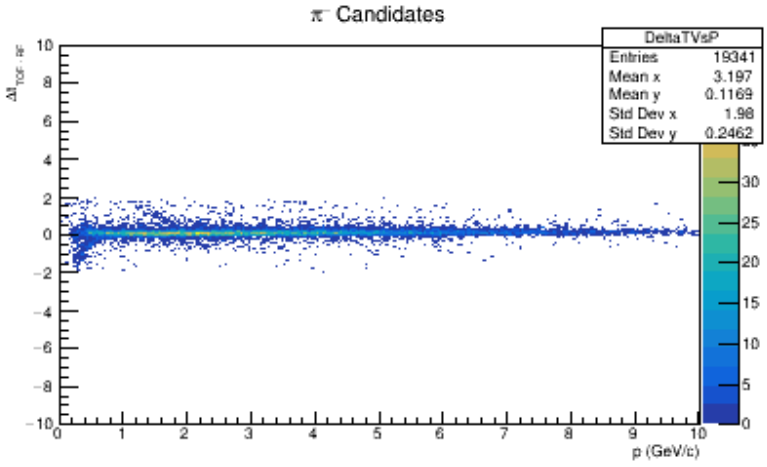

(c) 4.4b

Figure 4.4: π^- Δt cuts in the BCAL, FCAL, and TOF. Panel a shows the BCAL cuts events with $\Delta t \leq |1.5|$. Panel b shows the FCAL cuts events with $\Delta t \leq |3.0|$. Panel c shows the BCAL cuts events with $\Delta t \leq |2.0|$

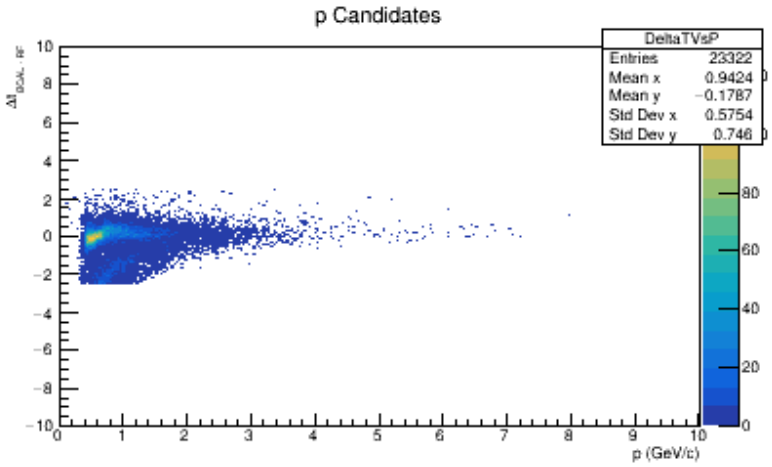

(a) 4.5a

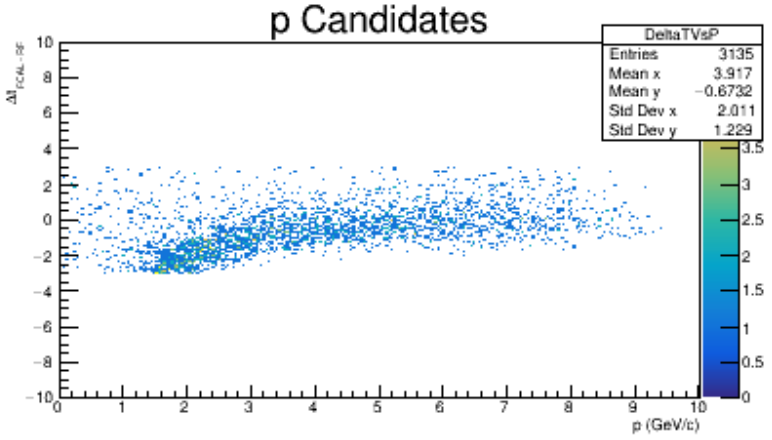

(b) 4.5b

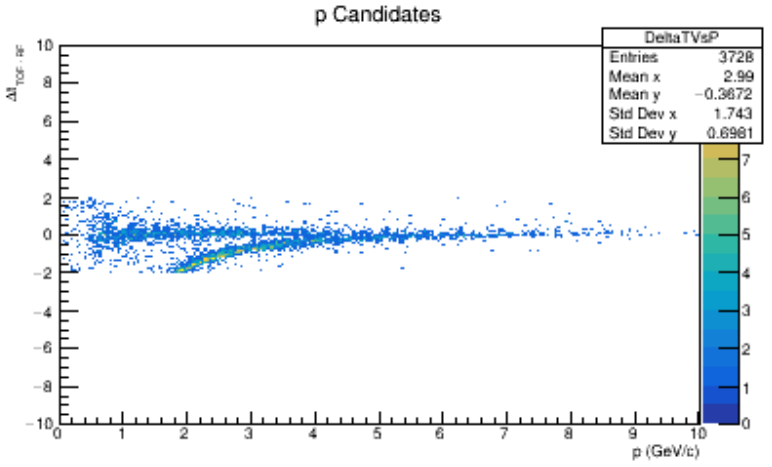

(c) 4.5b

Figure 4.5: Proton Δt cuts in the BCAL, FCAL, and TOF. Panel a shows the BCAL cuts events with $\Delta t \leq |1.5|$. Panel b shows the FCAL cuts events with $\Delta t \leq |3.0|$. Panel c shows the BCAL cuts events with $\Delta t \leq |2.0|$

The plots shown in Fig. 4.3, Fig. 4.4, and Fig. 4.5 display the difference between the time the event was measured for the detector and the RF time. The desired events should have been measured by the TOF, BCAL and FCAL within a certain time window. Placing a width on this window reduces the background events considerably.

Tighter cuts were applied during the DSelector process. This step takes less time to run over the post reconstruction data and so can be used to finely tune the analysis. The cuts used for the analysis discussed in this chapter include the following:

- Missing mass squared: $\pm 0.02\ (GeV/c^2)^2$
- Photon beam energy: $8.4 - 9\ GeV$
- $0.6\ GeV/c^2 \leq$ Invariant mass of $(\pi^+ + \pi^-) \leq 0.88\ GeV/c^2$
- dE/dX Cut on CDC to remove recoil protons
- Particle identification (PID) for TOF, BCAL and FCAL
- Momentum transfer $0.02 < |t| < 0.08\ (GeV/c)^2$
- Vertex reconstruction limited to target region 50 cm $< Z <$ 80 cm

Fig. 4.6a shows the distribution of the missing mass squared (MM^2) for the $\gamma p \to \pi^+\pi^- p$ decay channel. The yellow region contains the events which have $|MM^2| < 0.02\ (GeV/c^2)^2$. Events outside this range are vetoed and are not used in the analysis. The photon beam region was selected to include the coherent peak so that a high average linear polarization would be obtained. The invariant mass of the ρ meson was constructed from the combination of the $\pi^+\pi^-$ invariant masses. Limiting this sum to the specified range helps to reduce misidentified particles with higher/lower masses. The invariant mass plot is shown in Fig. 4.6b has the typical line shape, mean and width associate with the ρ vector meson. Events within the yellow region of the invariant mass were also kept. Fig. 4.6c and Fig. 4.6d show the regions of selected events for the position of the reconstructed vertex (in the z axis) and δt.

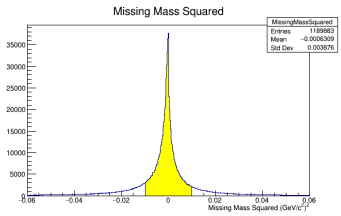

(a) 4.6a

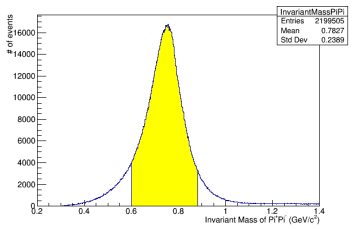

(b) 4.6b

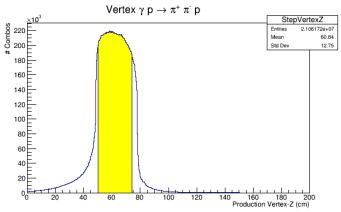

(c) 4.6c

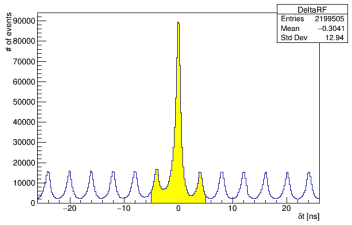

(d) 4.6d

Figure 4.6: Fig. 4.6a: Plot of the missing mass squared for the decay channel $\gamma p \to \pi^+\pi^- p$. The region shaded in yellow is the range over which events are kept. Fig. 4.6b: Sum of the $\pi^+\pi^-$ invariant masses after event selection. Events contained within the yellow region were kept for the analysis. The plot has the typical line shape, mean and width associated with the ρ vector meson. Fig.4.6c: Position of reconstructed vertex (z axis). Events within the shaded region are located within the target region and are kept for the analysis. Fig. 4.6d: Beam bunch period, shaded region includes photons used in this analysis. Accidental subtraction was performed using the additional beam bunches.

4.1.4 CB Polarization and Beam Asymmetry Measurements

Following the procedure detailed in the previous section, the product of the beam asymmetry (A) and beam polarization ($P_\perp$ or $P_\parallel$) can be extracted from the azimuthal dependence of the yield in photoproduction for the photoproduction of the ρ vector meson with linearly polarized photon beam and an unpolarized target. The event selection discussed above was implemented on the most stable subset of spring 2016 GlueX data, which contained a total of 11 billion physics triggers for both the PARA and PERP orientations.

The reaction $\gamma p \to \pi^+\pi^- p$ was studied in the helicity reference frame, where the ρ is at rest and the z direction is opposite to the direction of the recoil proton. Another way to consider this is that the z direction is in the direction of flight of the vector meson (ρ) in the overall center of mass frame. The y direction is chosen to be normal to the production

plane which is defined by the cross product of the incident photon's three-momentum vector ($\mathbf{k}$) and the ρ three-momentum ($\mathbf{q}$). The x direction is then the cross product between the y and z direction. The decay angles θ and ϕ are the polar and azimuthal angles determined by the direction of the π^+ decay product in the two-body decay ($\pi^+\pi^-$) and denoted by the unit vector $\boldsymbol{\pi}$. The described coordinate system and angle definitions are given by Eq. 4.6 and Eq. 4.7 respectively [23].

$$\mathbf{z} = \frac{\mathbf{k}}{|\mathbf{k}|}, \qquad \mathbf{y} = \frac{\mathbf{k} \times \mathbf{q}}{|\mathbf{k} \times \mathbf{q}}, \qquad \mathbf{x} = \frac{(\mathbf{k} \times \mathbf{q}) \times \mathbf{k}}{|(\mathbf{k} \times \mathbf{q}) \times \mathbf{k}|} \tag{4.6}$$

$$\cos\theta = \boldsymbol{\pi} \cdot \mathbf{z}, \qquad \frac{\mathbf{y} \cdot (\mathbf{z} \times \boldsymbol{\pi})}{|\mathbf{x} \times \boldsymbol{\pi}|}, \qquad \sin\phi = -\frac{\mathbf{x} \cdot (\mathbf{z} \times \boldsymbol{\pi})}{|\mathbf{z} \times \boldsymbol{\pi}|} \tag{4.7}$$

As shown in Fig. 4.2, the difference in angle between the ρ production plane and the plane of the electric field vector of the incoming beam photon is denoted by ϕ. These angular distributions were measured for both the PARA and PERP orientations and examples are shown in Fig. 4.7a and 4.7b for the same energy bin.

The distributions were fit using the form shown in Eq. 4.8, where the sign of the product PA is expected to change between the two radiator orientations.

$$1 + PA\cos 2\phi \tag{4.8}$$

The angular distribution for each energy bin was measured and fit using Eq. 4.8 and the parameter PA was plotted as a function of photon energy, shown in Fig. 4.8.

The data collected during the PARA and PERP orientations were used with Eq. 4.5 to extract the asymmetry as a function of photon beam energy and is shown in Fig. 4.9. The distributions shown in Fig. 4.8 and 4.9 clearly show the that the installed radiator is producing a clean CB enhancement around 9 GeV and its first harmonic around 10.5 GeV. It is the hope that using thinner radiators such as JD70-104, will result in stronger peaks due to the reduction in the size of the photon collimator made possible by reduced multiple scattering in the radiator.

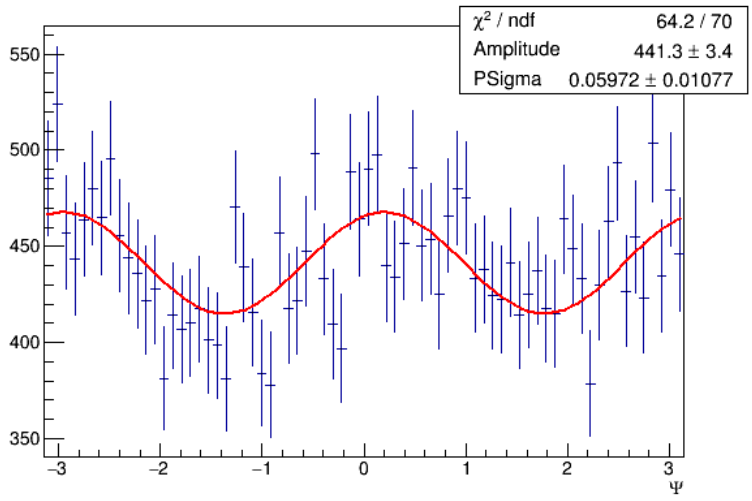

(a) 4.7a

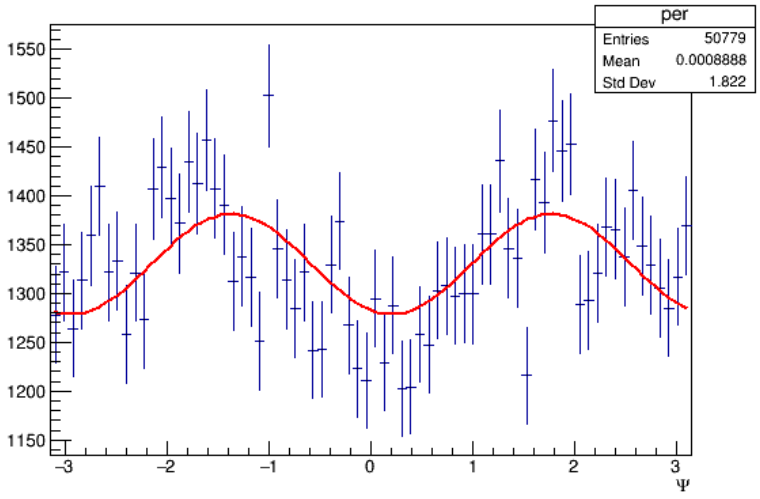

(b) 4.7b

Figure 4.7: Panel a shows the distribution of the ϕ angle between the polarization and production planes for the PARA orientation of the diamond radiator. Panel b shows distribution of the $\Delta\phi$ angle between the polarization and production planes for the PERP orientation of the diamond radiator.

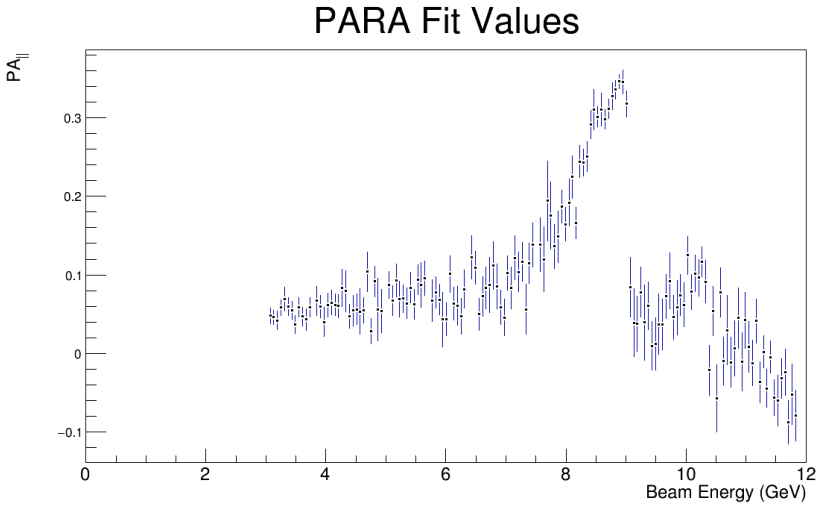

(a) 4.8a

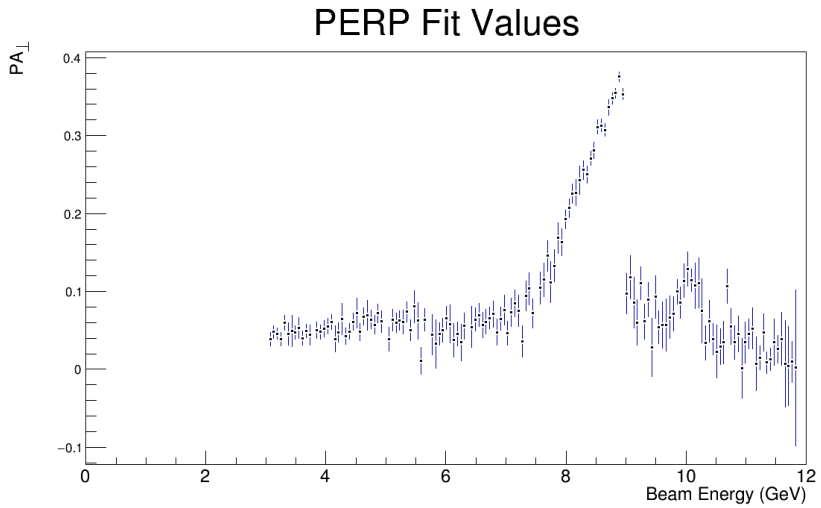

(b) 4.8b

Figure 4.8: Panel a shows PA as a function of photon beam energy measured using the spring 2016 GlueX data set for the diamond in the PARA orientation. Panel b shows PA as a function of photon beam energy measured using the spring 2016 GlueX data set for the diamond in the PERP orientation.

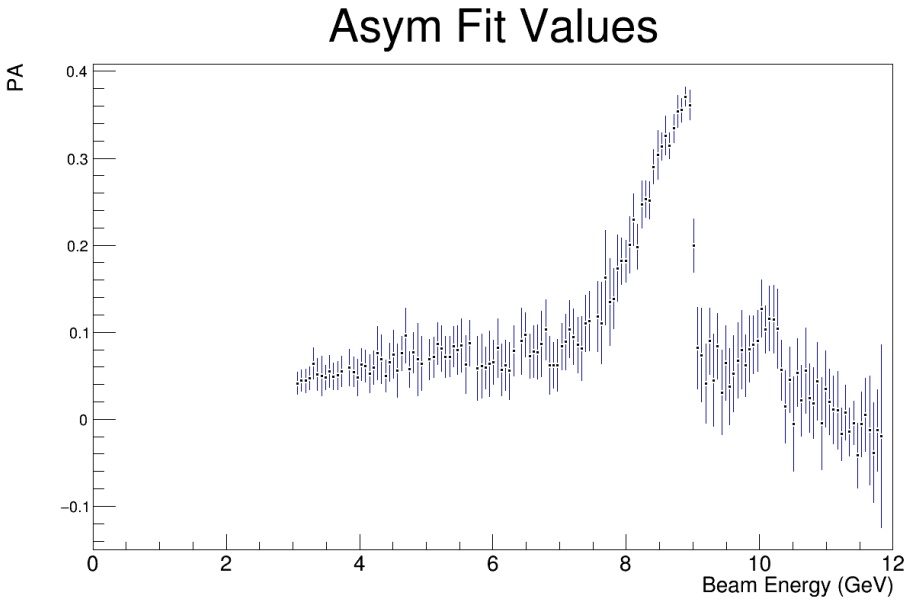

Figure 4.9: Average asymmetry extracted from angular distributions in both PARA and PERP orientations using the form shown in Eq. 4.5.

4.1.5 Extraction of Spin-density Matrix Elements

Introduction

The motivation for developing the laser ablation technique was to create a coherent bremsstrahlung radiator that could be used to produce a 9 GeV photon beam with a high degree of linear polarization. The strict experimental requirements placed on the thickness and mosaic spread were derived from principles of QCD theory so that gluonic excitations could be observed. While the GlueX experiment is still in its early years of physics data taking and not ready to begin the search for exotic mesons, there are some interesting physical observables that can be measured which are strict tests of the quality of the photon beam. The final section of this thesis is devoted to the measurement of the photo-produced ρ vector meson's spin-density matrix elements (SDMEs) at 8.4-9 GeV. A brief theoretical discussion follows.

During vector meson photoproduction it is possible, even with an unpolarized photon beam, for the vector meson to be polarized. The vector meson spin-state is described by its density matrix, whose elements contain information on the decay distribution, $W(\cos\theta, \phi)$,

which contains information about the underlying production mechanism of vector meson. The SDMEs are measured through the decay distributions such as those already shown for the ρ vector meson.

Production Amplitudes

The density matrix for the initial photon beam, $\rho(\gamma)$ can be connected to the density matrix of the product vector meson, $\rho(V)$ through the characterization of the photoproduction reaction by an amplitude T. They can be written in terms of each other [23].

$$\rho(V) = T\rho(\gamma)T^{\dagger}. \tag{4.9}$$

In the center-of-mass frame helicity representation this can be written as

$$\rho_{\lambda_V \lambda'_v}(V) = \frac{1}{\mathcal{N}} \sum_{\lambda'_N \lambda_\gamma \lambda_N \lambda'_\gamma} T_{\lambda_V \lambda'_N \lambda_\gamma \lambda_N} \rho'_{\lambda_\gamma \lambda_\gamma} T^{\dagger}_{\lambda'_V \lambda'_N \lambda'_\gamma \lambda_N}, \tag{4.10}$$

where the λ_x represents the helicity of the incoming (N) and outgoing (N') nucleon, the photon (γ,γ'), and the vector meson (V,V') [24]. A normalization factor is given by the term $\mathcal{N}$ as

$$\mathcal{N} = \frac{1}{2} \sum_{\lambda_V \lambda'_N \lambda_\gamma} |T_{\lambda_V \lambda'_N \lambda_\gamma \lambda_N}|^2, \tag{4.11}$$

which can be related to the unpolarized differential cross section as

$$\frac{d\sigma}{d\Omega} = \frac{1}{2} \left(\frac{2\pi}{k} \right)^2 \mathcal{N}. \tag{4.12}$$

where k is the momentum of the photon in the center of mass.

Measuring the differential cross section and the density matrix elements of the vector meson photoproduction yields information regarding the production processes. The elements of the ρ vector meson density matrix can be accessed through the decay angular distributions of the daughter products, $\pi^+\pi^-$ [23].

Spin-density Matrix Elements

The photon polarization vector $\mathbf{P}_\gamma$ for linearly polarized photons can be written in a frame where the photon direction is alond the z axis, as

$$\mathbf{P}_\gamma = P_\gamma(-\cos 2\Phi, -\sin 2\Phi, 0) \tag{4.13}$$

where P_γ is the degree of linear polarization (between 0 and 1), and where Φ is the azimuthal angle of the photon plarization place in the chosen reference frame [24]. Circularly polarized photons can be written as

$$\boldsymbol{P_\gamma} = P_\gamma(0, 0, \pm 1) \tag{4.14}$$

where as before, P_γ is the degree of circular polarization and the ± 1 corresponds to the helicity of the photon, $\lambda_\gamma = +1$ or $\lambda_\gamma = -1$. Considering the three components of the photon polarization the vector meson density matrix can be written as the sum

$$\rho(V) = \rho_V^0 + \sum_{\alpha=1}^{3} P_\gamma^\alpha \rho^\alpha, \tag{4.15}$$

where, based on the photon polarization, the ρ^α form a decomposition of the total density matrix [24]. These ρ^α are related to the amplitudes, T, as

$$\rho^0_{\lambda_V \lambda'_V}(V) = \frac{1}{2\mathcal{N}} \sum_{\lambda_V \lambda'_N, \lambda_\gamma \lambda_N} T_{\lambda_V \lambda'_N, \lambda_\gamma \lambda_N} T^*_{\lambda'_V \lambda'_N, \lambda_\gamma \lambda'_N} \tag{4.16}$$

$$\rho^1_{\lambda_V \lambda'_V}(V) = \frac{1}{2\mathcal{N}} \sum_{\lambda_V \lambda'_N, \lambda_\gamma \lambda_N} T_{\lambda_V \lambda'_N, -\lambda_\gamma \lambda_N} T^*_{\lambda'_V \lambda'_N, \lambda_\gamma \lambda'_N} \tag{4.17}$$

$$\rho^2_{\lambda_V \lambda'_V}(V) = \frac{i}{2\mathcal{N}} \sum_{\lambda_V \lambda'_N, \lambda_\gamma \lambda_N} \lambda_\gamma T_{\lambda_V \lambda'_N, \lambda_\gamma \lambda_N} T_{\lambda'_V \lambda'_N, \lambda_\gamma \lambda'_N} \tag{4.18}$$

$$\rho^3_{\lambda_V \lambda'_V}(V) = \frac{1}{2\mathcal{N}} \sum_{\lambda_V \lambda'_N, \lambda_\gamma \lambda_N} \lambda_\gamma T_{\lambda_V \lambda'_N, \lambda_\gamma \lambda_N} T_{\lambda'_V \lambda'_N, \lambda_\gamma \lambda'_N} \tag{4.19}$$

It is possible to reduce the number of independent spin-density matrix elements by utilizing their symmetry properties and considering the fact that the density matrices are Hermitian [24]. These spin-density matrices can be expressed in terms of 17 real numbers, 11 of which

are measurable [23]. The 17 real numbers are as follows.

$$\rho^0 = \begin{pmatrix} \frac{1}{2}(1-\rho^0_{00}) & Re\rho^0_{10} + iIm\rho^0_{10} & Re\rho^0_{1-1} \\ & \rho^0_{00} & -(Re\rho^0_{10} - iIm\rho^0_{10}) \\ & & \frac{1}{2}(1-\rho^0_{00}) \end{pmatrix} \tag{4.20}$$

$$\rho^1 = \begin{pmatrix} \rho^1_{11} & Re\rho^1_{10} + iIm\rho^1_{10} & Re\rho^1_{1-1} \\ & \rho^1_{00} & -(Re\rho^1_{10} - iIm\rho^1_{10}) \\ & & \rho^1_{11} \end{pmatrix} \tag{4.21}$$

$$\rho^2 = \begin{pmatrix} \rho^2_{11} & Re\rho^2_{10} + iIm\rho^2_{10} & iIm\rho^2_{1-1} \\ & 0 & Re\rho^2_{10} - iIm\rho^2_{10} \\ & & -\rho^2_{11} \end{pmatrix} \tag{4.22}$$

$$\rho^3 = \begin{pmatrix} \rho^3_{11} & Re\rho^3_{10} + iIm\rho^3_{10} & iIm\rho^3_{1-1} \\ & 0 & Re\rho^3_{10} - iIm\rho^3_{10} \\ & & -\rho^3_{11} \end{pmatrix} \tag{4.23}$$

The lower half of of the matrices are completed by the hermitian conjugates. The trace of ρ^0 is 1, so that $\rho^0_{11} = \frac{1}{2}(1-\rho^0_{00})$. There are three cases for which we can measure three different sets of the SDMEs. For unpolarized photon beams, three of the four real values describing the ρ^0 SDMEs can be measured. In the case of circularly polarized photons, the same three ρ^0_{00} SDMEs can be measured plus two of the four real values from the ρ^3 SDMEs. Finally, with linearly polarized photons, the same ρ^0 elements are accessible, however four of the five real elements of the ρ^1 SDMEs and two of the four from ρ^2 are also measurable [23].

Decay Distributions of Vector Mesons

The decay angular distribution for photoproduced vector mesons can be expressed in terms of the same SDMEs, ρ^α_{ij} described in the previous section. The sum is written as,

$$W_h(\cos\theta, \phi) = W^0_h(\cos\theta, \phi) + \sum_{\alpha=1}^{3} P^\alpha_\gamma W^\alpha_h(\cos\theta, \phi), \tag{4.24}$$

where P_γ^α is the polarization vector of the photon given by Eq. 4.13 and Eq. 4.14. or hadronic decays of the ρ vector meson ($\rho^0 \to \pi^+\pi^-$) the W_h^α are given as

$$W_h^0(\cos\theta,\phi,\rho^0) = \frac{3}{4\pi}\Big[\frac{1}{2}(1-\rho_{00}^0) + \frac{1}{2}(3\rho_{00}^0-1)\cos^2\theta - \sqrt{2}Re\rho_{10}^0\sin 2\theta\cos\phi - \rho_{1-1}^0\sin^2\theta\cos 2\phi\Big] \tag{4.25}$$

$$W_h^1(\cos\theta,\phi,\rho^1) = \frac{3}{4\pi}\Big[\rho_{11}^1\sin^2\theta + \rho_{00}^1\cos^2\theta - \sqrt{2}Re\rho_{10}^1\sin 2\theta\cos\phi - \rho_{1-1}^1\sin^2\theta\cos 2\phi\Big] \tag{4.26}$$

$$W_h^2(\cos\theta,\phi,\rho^2) = \frac{3}{4\pi}\Big[\sqrt{2}Im\rho_{10}^2\sin 2\theta\sin\phi + Im\rho_{1-1}^2\sin^2\theta\sin 2\phi\Big] \tag{4.27}$$

$$W_h^3(\cos\theta,\phi,\rho^3) = \frac{3}{4\pi}\Big[\sqrt{2}Im\rho_{10}^3\sin 2\theta\sin 2\theta\sin\phi + Im\rho_{1-1}^3\sin^2\theta\sin 2\phi\Big] \tag{4.28}$$

As stated previously, the angles θ and ϕ denote the direction of the $\boldsymbol{\pi}$ in the helicity system. Although, the results are true for any system that can be reached by a rotation.

Decay Distributions for Polarized Photon Beams

For a linearly polarized photon beam the following SDMEs can be measured: ρ_{00}^0, $\rho_{1,-1}^0$, $Re\rho_{01}^0$, ρ_{00}^1, ρ_{11}^1, ρ_{1-1}^1, $Re\rho_{10}^1$, $Im\rho_{1-1}^2$ and $Im\rho_{10}^2$. Eq. 4.24 becomes

$$W^L(\cos\theta,\phi,\Phi) = W_h^0(\cos\theta,\phi) - P_\gamma\cos 2\Phi W_h^1(\cos,\phi) - P_\gamma\sin 2\Phi W_h^2(\cos\theta,\phi) \tag{4.29}$$

Eq. 4.29 can be expanded in terms of the SDMEs for hadronic decays of vector mesons.

$$\begin{aligned} W^L(\cos\theta,\phi,\Phi) = \frac{3}{4\pi}\Big[&\frac{1}{2}(1-\rho_{00}^0) + \frac{1}{2}(3\rho_{00}^0-1)\cos^2\theta - \sqrt{2}Re\rho_{10}^0\sin 2\theta\cos\phi - \rho_{1-1}^0\sin^2\theta\cos 2\phi \\ &- P_\gamma\cos 2\Phi(\rho_{11}^1\sin^2\theta + \rho_{00}^1\cos\theta - \sqrt{2}Re\rho_{10}^1\sin 2\theta\cos\phi - \rho_{1-1}^1\sin^2\theta\cos 2\phi) \\ &- P_\gamma\sin 2\Phi(\sqrt{2}Im\rho_{10}^2\sin 2\theta\sin\phi + Im\rho_{1-1}^2\sin^2\theta\sin 2\theta)\Big] \end{aligned} \tag{4.30}$$

where P_γ is the linear polarization of the incident photon and Φ is the angle between the polarization vector of the photon and the (x,y) production plane.

There is information about the natural and unnatural parity exchange that can be learned by measuring these SDMEs using linearly polarized photons. At sufficiently high energiees, the ρ^{α} density matrix elements can be written as the sum of the natural and unnatural contributions, such as for the ρ^0

$$\rho^0 = \rho^{0(N)} + \rho^{0(U)}, \rho^{0\binom{N}{U}}_{\lambda\lambda'} = \sum_{\lambda_\gamma \lambda_N \lambda_{N'}} T^{\binom{N}{U})}_{\lambda\lambda_{N'},\lambda_\gamma\lambda_N} T^{\binom{N}{U}*}_{\lambda'\lambda_{N'},\lambda_\gamma\lambda_N} \tag{4.31}$$

which leads to the following equations

$$\rho^0 = \rho^{0(N)} + \rho^{0(U)}, \qquad \rho^{0\binom{N}{U}}_{\gamma\gamma'} = \frac{1}{2}(\rho^0_{\gamma\gamma'} \mp (-1)^\gamma \rho^1_{-\gamma\gamma'}), \tag{4.32}$$

$$\rho^1 = \rho^{1(N)} + \rho^{1(U)}, \qquad \rho^{1\binom{N}{U}}_{\gamma\gamma'} = \frac{1}{2}(\rho^1_{\gamma\gamma'} \mp (-1)^\gamma \rho^0_{-\gamma\gamma'}), \tag{4.33}$$

$$\rho^2 = \rho^{2(N)} + \rho^{2(U)}, \qquad \rho^{2\binom{N}{U}}_{\gamma\gamma'} = \frac{1}{2}(\rho^2_{\gamma\gamma'} \mp (-1)^\gamma \rho^3_{-\gamma\gamma'}), \tag{4.34}$$

$$\rho^3 = \rho^{3(N)} + \rho^{3(U)}, \qquad \rho^{3\binom{N}{U}}_{\gamma\gamma'} = \frac{1}{2}(\rho^3_{-\gamma\gamma'} \pm i(-1)^\gamma \rho^2_{-\gamma\gamma'}). \tag{4.35}$$

The parity asymmetry P_σ in the σ^N and σ^U of the total cross section is defined as,

$$P_\sigma = \frac{\sigma^N - \sigma^U}{\sigma^N + \sigma^U} = 2\rho^1_{1-1} - \rho^1_{00} \tag{4.36}$$

and the beam polarization asymmetry Σ is defined as,

$$\Sigma = \frac{\sigma^{\parallel} - \sigma^{\perp}}{\sigma^{\parallel} + \sigma^{\perp}} = \frac{\rho^1_{11} + \rho^1_{1-1}}{\rho^0_{11} + \rho^0_{1-1}} \tag{4.37}$$

Vector meson photoproduction is predicted to be a diffractive process by the helicity conservation model (HCM). HCM also predicts that the ρ matrices are invariant with respect to the photon energy and angle of production. It also states that ρ^0 and ρ^3 are diagonal and ρ^1 and ρ^2 are anti-diagonal. If only natural parity exchange is assumed, then the density

matrices should have the following values

$$\rho^0 = \begin{bmatrix} \frac{1}{2} & 0 & 0 \\ 0 & 0 & 0 \\ 0 & 0 & \frac{1}{2} \end{bmatrix} \qquad \rho^1 = \begin{bmatrix} 0 & 0 & \frac{1}{2} \\ 0 & 0 & 0 \\ \frac{1}{2} & 0 & 0 \end{bmatrix} \tag{4.38}$$

$$\rho^2 = \begin{bmatrix} 0 & 0 & -\frac{1}{2} \\ 0 & 0 & 0 \\ \frac{1}{2} & 0 & 0 \end{bmatrix} \qquad \rho^3 = \begin{bmatrix} \frac{1}{2} & 0 & 0 \\ 0 & 0 & 0 \\ 0 & 0 & -\frac{1}{2} \end{bmatrix} \tag{4.39}$$

The SDMEs of the ρ vector meson photoproduced at 9 GeV by a linearly polarized photon were studied by the author. Based on the discussion above, there are expected values for these SDMEs if helicity is conserved and if there is only natural parity exchange. The extraction of these values was completed with a set of tools whose operation is explained in the following section.

Monte Carlo and AmpTools

Physics events are simulated using a process called Monte Carlo simulation. This involves generating events based on a given set of assumptions for the cross section and decay dynamics and simulating the final state interactions with the GlueX detector. A generator was written to create events with two pions and a proton in the final state. An analysis framework created at Indiana University called AmpTools was used for the analysis of the SDMEs. Although originally designed for amplitude analysis, AmpTools is also capable of generating simulated data based on given physics amplitudes. AmpTools represents the multi-particle intensity distribution observed in a detector in terms of a sum over elementary physics amplitudes,

$$I(\Omega) = \sum_{\alpha} |\sum_{\beta} V_{\alpha\beta} A_{\alpha\beta}(\Omega)|^2 \tag{4.40}$$

where Ω is the kinematics from the 4-vectors. The sum over β is a coherent sum over different quantum pathways called "partial waves" that lead to the same final state. $V_{\alpha\beta}$ are

the production amplitudes (complex fit parameters) and $A_{\alpha\beta}$ are known theoretical partial wave amplitudes of the decay products. Experimental observables can be related to the intensity through

$$\int I(\Omega)\eta(\Omega)d\Omega = N_{predicted} \tag{4.41}$$

$\eta(\Omega)$ being the detector acceptance. The number of degrees of freedom involved in this amplitude analysis is considerable. This is solved by using a Maximum Likelihood Method (ML) in which the "likelihood" is constructed as the combined probability for detection all the events seen and getting the detected count of events assuming a random sample governed by the unknown production amplitudes $V_{\alpha,\beta}$. A model of the ρ meson photoproduction intensity was created with the form,

$$I(\Omega) = A_{norm} \cdot PS \cdot BW \cdot W(\cos\theta, \phi, \Phi) \exp^{At} \tag{4.42}$$

where A_{norm} is the normalization factor, PS and BW are the phase-space factor and Breit-Wigner respectively, $W(\cos\theta, \phi, \Phi)$ is the angular dependence derived in the previous section and $\exp^{At}$ is the t-dependence. The AmpTools framework includes classes for each of these factors. The Breit-Wigner class in AmpTools required user input for the mass and width of the vector meson (0.775 GeV and 0.0008 GeV), the orbital angular momentum ($l = 1$) and the decay products ($\pi^+\pi^-$) of the resonance. The W angular distributions are also a provided class within the AmpTools framework. The simulation completed by the author assumed s-channel helicity conservation from linearly polarized photons. The input values for the independent SDMEs of the W angular distribution were all zero except for ρ^1_{1-1} and $Im\rho^2_{1-1}$ which, as shown in Eq. 4.39 are set to $\frac{1}{2}$ and $-\frac{1}{2}$ respectively. Finally, the t-dependence was set to match the value reported by SLAC. The photon beam in this simulation was generated with zero polarization.

Using AmpTools, 1 million events were generated within the photon beam energy range of $7.5 - 9.5$ GeV. The generated four-vectors were then passed through a detailed physics simulation of the GlueX detector called hdgeant3. Each generated event was passed through

the various GlueX detectors to simulate their response. The resolution of each detector is also taken into consideration as the results from the previous step are "smeared" (mcsmear) to model these resolutions and efficiencies.

The simulated data were then passed through the same event selection as described above for real data. An example of the invariant mass and angular distributions for the simulated ρ vector meson decay channel is shown below in Fig. 4.10 and Fig. 4.11 respectively.

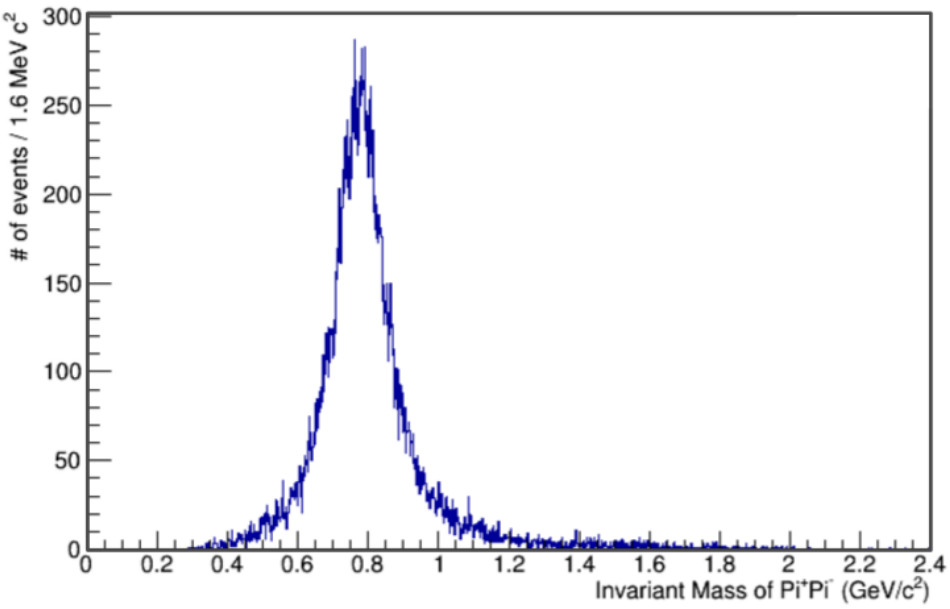

Figure 4.10: Invariant mass of acceptance corrected ρ mesons reconstructed using the same event selection as GlueX data.

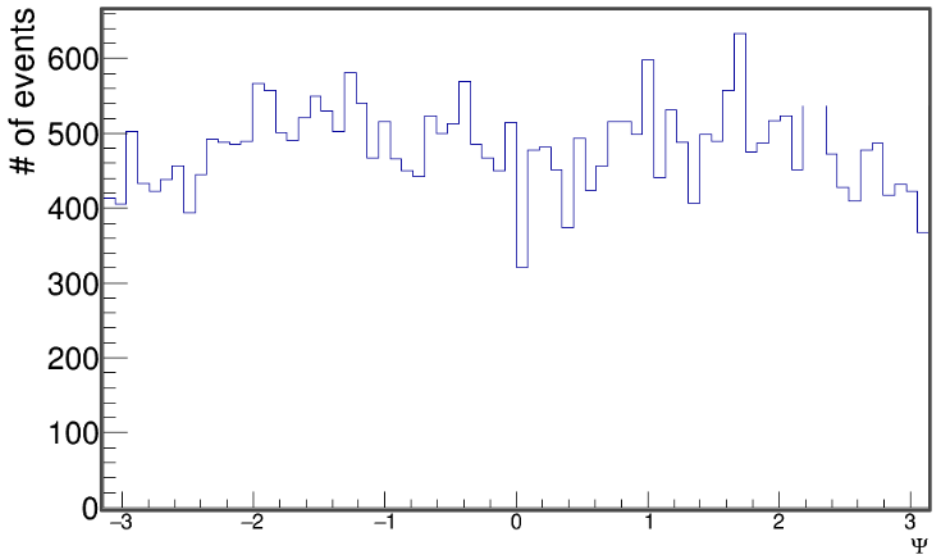

Figure 4.11: Ψ angular distribution of acceptance corrected Monte Carlo simulated data. The distribution is flat because the simulation was performed with an unpolarized beam.

Extraction of SDMEs

The process of extracting SDMEs from the spring 2016 data set for the decay channel $\gamma p \to \pi^+\pi^- p$ using the AmpTools framework involves the use of three sets of data. The first is the actual data set after the event selection has been completed. This contains the angular distributions from which the SDMEs can be extracted. The second file is a set of Monte Carlo data which has a flat (unpolarized beam) angular distribution and that has gone through the hdgeant3 and mcsmear step, but not are not subjected to any cuts. The last file is the same as the second, except that is has also passed through the full analysis, the same filter as the real data. The general idea is that the simulated data has a flat angular distribution which contains no physics, but can be fit to the real data using the form Eq. 4.30 from which the SDME parameters can be extracted. Comparing the simulated data that were passed through both the detector and the event selection process to the uncut simulated events accounts for detector acceptance which is inherent in the real data. The SDMEs were found using the method described above and are displayed below in Fig. 4.12.

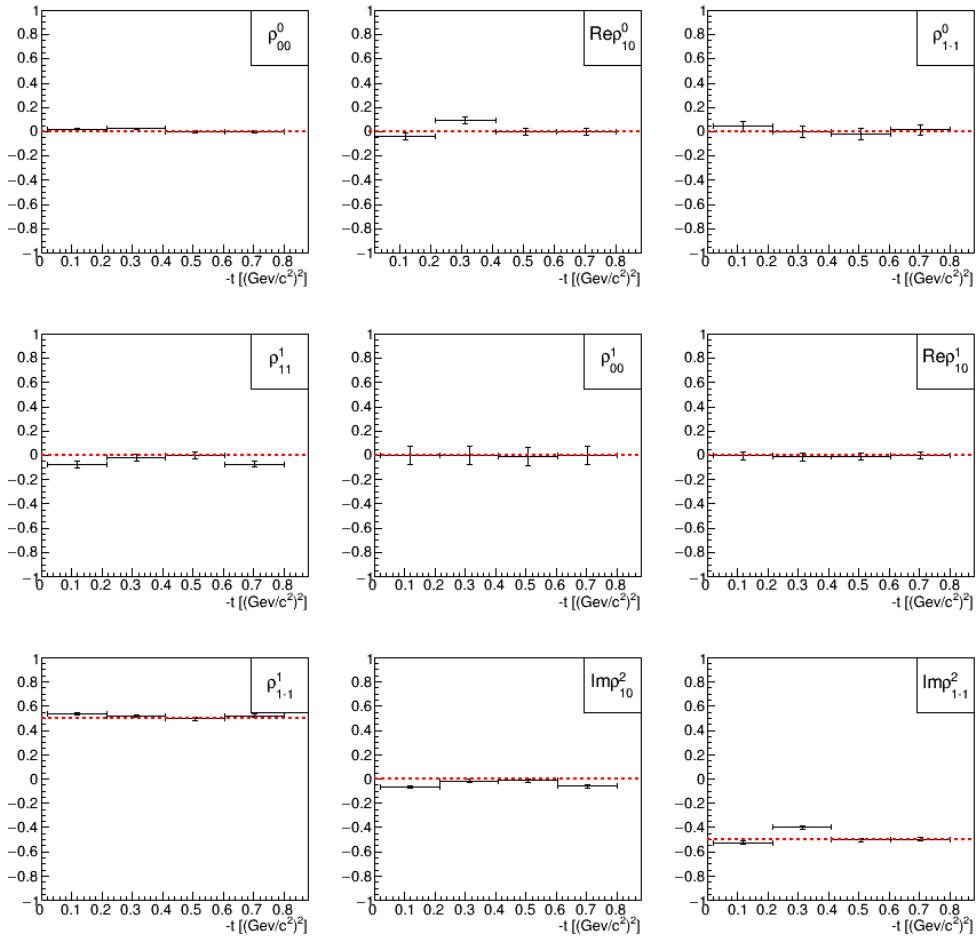

Figure 4.12: Spin-density matrix elements (SDMEs) measured using the AmpTools framework. Red dotted lines represent model predictions. The error bars represent the statistical and systematic uncertainties added in quadrature.

The SDMEs shown in Fig. 4.12 agree fairly well with the s-channel helicity conservation model for s $\rightarrow \infty$. In the model, the only non-zero elements should be the ρ^1_{1-1} and the $Im\rho^2_{1-1}$ with values of ± 0.5 respectively. The SDMEs measured using the GlueX Fall 2016 data and the AmpTools framework are in agreement with the model predictions which also suggests natural parity exchange, as predicted.

4.2 Concluding Remarks

This analysis presents initial findings for the GlueX experiment using a 50 μm diamond radiator. As the experiment continues not only will GlueX produce larger data sets (higher statistics), but it will test the effectiveness of 20 μm diamond radiators produced at the University of Connecticut using the methods described in this thesis. Once these data are available, the same analysis of the $\gamma p \to \pi^+\pi^- p$ should be conducted and the results compared.

Appendices

APPENDIX A

Ablation Procedures

A complete description of the procedures followed to produce a single 20 μm diamond radiator for the GlueX experiment is detailed below. It is assumed that the user is familiar with the Lambda Physik EMG 101 MSC excimer laser and has received proper safety training. The laser is currently set up to operate at 193 nm and appropriate safety glasses should be worn at all times while the laser's high voltage is turned on. The laser's standard operating procedures (S.O.P.) should be carefully read before attempting to use the laser as well. As indicated in the S.O.P., the plastic shielding must be in place whenever the laser is in use.

The laser manual has detailed descriptions of how to properly clean and align the laser optics which is essential for reaching peak power output with this laser. While optics cleaning is only required after extended use, the laser alignment should be checked whenever a large decline in laser energy output is noticed.

A.1 Operating the Laser Ablation Facility

A.1.1 Starting and Filling the Laser

The laser must be turned on and will need to warm up for at least 10 minutes before use. This allows the thyratron to reach the appropriate operating temperature. Once the laser's "Warm Up Timer" interlock has elapsed, the laser is ready for use. During this time, it is common to refill the laser with a new mixture of halogen, noble, and buffer gas. To complete this task, the roughing pump is turned on by engaging the switch on the laser head labeled "VACUUM PUMP" to the "ON" position. The butterfly-valve located on the laser head exhaust port should be opened slightly so that the needle of the rough pressure gauge (which monitors the laser head pressure between 0 and 4,000 mbar) moves slowly towards zero. Once the gauge's needle has passed the 1,000 mbar mark, the valve can be completely

opened. This is done to prevent high concentrations of fluorine gas from exiting the laser head and possibly burning the charcoal-halogen filter installed on the roughing pump.

Once the fine pressure gauge (located on the laser head above the rough pressure gauge) reads zero mbar, the vacuum pump can be turned off and the butterfly-valve closed. The laser should be filled with lasing gas quickly to prevent air from entering the system through small leaks in the laser head. The halogen gas (5% fluorine in helium balance) should enter the laser first by pressing the red button labeled "HALOGEN GASES" until the fine pressure gauge needle reads 200 mbar. Next, the blue button on the laser head should be pressed, allowing the noble gas to enter (argon) until the fine pressure gauge reads 500 mbar. Finally, the buffer gas (helium) is introduced by pressing the yellow button on the laser head until the rough pressure gauge reads 2,100 mbar. The laser is now filled with new lasing medium and is ready for use. After extended periods of non-use, the laser may require multiple fill/flush cycles before reaching maximum energy output.

A.1.2 Passivation

If the laser has been disassembled or not used for a very long time, the system will require passivation. Passivation is the process of introducing halogen gas so that it can react with the laser cavity interior until it is inert to the halogen. Passivation is accomplished by filling the laser the same way as described above with 200 mbar of halogen, but no noble gas is used. Instead, the laser is filled to a final pressure of 2,000 mbar with helium gas. The laser high voltage is then set between 22,000 - 26,000 volts and allowed to fire at a repetition rate of 3 Hz. The laser should produce a solid red light from its aperture and should have a lifetime of at least 8 hours before a noticeable drop in the intensity of the red light. In the beginning, the red light will diminish as the halogen gas is reacting with the contaminants like oxygen and water vapor absorbed on the walls of the laser cavity and can no longer act as a lasing medium. When this occurs, the high voltage should be turned off and the laser refilled with a fresh passivation gas mixture. After a complete rebuild, the EMG 101 MSC

excimer laser typically requires 10-15 refills before it is ready for use. After cleaning and aligning the laser optics and a fresh gas refill, the laser should be able to produce UV pulses with energies between 80-120 mJ. Using the GP2000 cryogenic gas purifier, it is possible to run on a single fill for multiple passes over a 7 x 7 mm^2 diamond sample. Once the laser is producing energies in this range, an ablation run can be started.

A.1.3 Starting the GP2000 Cryogenic Gas Purifier

The GP2000 cryogenic gas purifier is the next system to set up before an ablation run can begin. After turning the GP2000 unit on (the green "ON" button) all valves connecting it to the laser head must first be closed. This is done before the addition of liquid nitrogen to prevent the lasing medium from condensing and collecting in the GP2000's cold trap. The top lid is then removed and approximately 7 liters of liquid nitrogen is slowly poured in. Once full, the lid is replaced and the temperature is monitored (on the front panel) until 80 Kelvin is reached. Only then can the valves be opened and the GP2000 circulating pump be turned on. The GP2000 should be allowed to run for at least 15 minutes before starting an ablation run so that it can filter the fresh gas in the laser cavity. The GP2000 will require periodic refills with liquid nitrogen over the course of an ablation run.

The next step in the sequence is to turn on the power supplies to the various peripherals including the xyz motors and controllers, the laser chilling unit, the ablation chamber vacuum flow controller, the high voltage triggering unit, and the beam stop power supply. This is done by a network controlled power switch called a net booter. It is accessed via a RS232 serial connection controlled by the Hyperterminal application found on the ablation station's desktop computer. The icon labeled "xyz stage" is opened and entering the command "ps 1" turns the net booter on and "ps 0" turns it off, which should be done when everything is being shut down.

A.1.4 Finding the XY Origin

The origin of the xy sample scanning motors is set to the position where the laser beam spot is centered on the bottom left corner of the diamond sample while held in the aluminum mount in the ablation chamber. This coordinate is found by placing a sacrificial diamond target in the mount and pulsing on it several times with the laser. The result is a dimple in the diamond target whose offset from the bottom-left corner gives the offset from the present motor position to the proper xy origin. This offset is best measured using the Zygo interferometer microscope. Since the diamond is held at a 45° angle, the thickness of the diamond must be considered when finding the y origin. These values are then used, in combination with the current position of the dial indicators to construct an origin to which all x and y values are relative.

A.1.5 Mounting the Diamond in the Ablation Chamber

Once all proper measurements have been taken of the diamond to be ablated, it can be mounted in the ablation chamber. The aluminum slide shown in the previous section must be cleaned thoroughly with ethanol before mounting a diamond sample. It is important to remove any debris that may have gotten stuck along the ridges where the diamond registers. Once the mount is clean, place the diamond so that its bottom-left corner sits squarely in the crotch of the mount and apply a small amount of thermal compound to the top-right corner to keep it in place and to ensure a good thermal contact between the diamond and the mount. Then, gently place the aluminum slide (and newly mounted diamond) onto the ablation chamber pedestal, making sure it is fully seated. The ablation chamber is now ready to be sealed with the plexi-glass lid using the (8) 4-40 machine-head screws. With the lid tightened securely against the o-ring, the roughing pump can now be turned on and the pressure monitored using the digital pressure gauge. The vacuum flow monitor should already be turned on. It's voltage level should read 0.8 V. The roughing pump should be

allowed at least 30 minutes to reach a steady-state pressure which can be varied by adjusting the mechanical needle valve attached to the ablation chamber. The average variation of the chamber pressure should not exceed $\pm 10\%$ of the initial pressure over the period of 8 hours (or the time required to complete a full run). The chamber should be allowed to reach a final pressure of approximately 600 mbar before the set up is ready for ablation.

A.2 Ablation Software

There are three sets of software packages used to control the ablation facility. The first is written in LabView (called *AblationStation.vi*). This LabView Virtual Instrument (VI) orchestrates the movements of the translation stages, the triggering of the laser, the readout of the energy meters and many other functions. It is based on a state-machine design and is described in detail in the following sub-sections. The second program runs in parallel with LabView and controls the actual triggering sequence of the laser. As discussed previously, custom raster patterns are created which allow the user to differentially ablate the diamond radiator to arbitrary shapes and surface profiles. This program is called *pulser.c*. The third software package used is called ablator (ablator.C, ablate.py) and uses Zygo white-light interferometry images to create the raster patterns used by the pulser.c program. A complete example of the functionality of the LabView code, its communication sequence with the pulser.c program, and how to create a set of raster files to laser ablate a diamond to 20 μm are discussed below.

A.2.1 Ablation Station.vi Software

With the laser chiller running and power to the xyz motor stages turned on, the LabView application can now be opened. The "Ablation Station.vi" file is located on the ablation station computer's desktop in a folder labeled "Ablation Station". Once opened, there are

numerous settings requiring input from the user. Figure A.1 is a screen shot of the Ablation Station.vi front panel. A description is given for each user input in Table A.1.

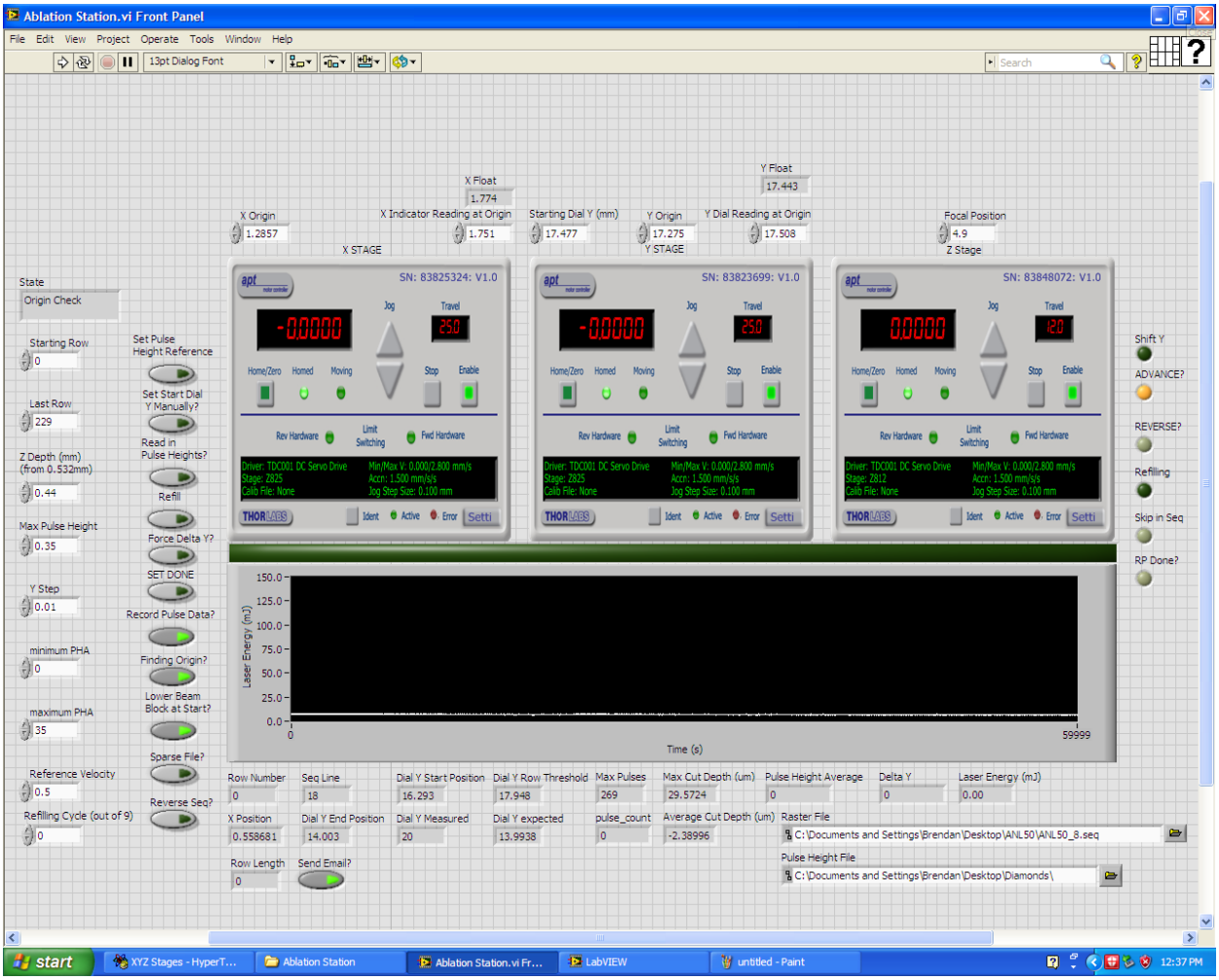

Figure A.1: Screen shot of the Ablation Station.vi front panel.

Table A.1: User inputs for Ablation Station.vi LabView software.

Field Name	Description
Starting Row	The seq file's row number to start on (typically 0)
Last Row	he seq file's row number to end on
Z Depth	depth of diamond surface with respect to reference diamond
Max Pulse Height	pulse height average corresponding with a full y step
Y Step	step size (mm) of y motor (typically 0.01 mm)
Minimum PHA	minimum pulse height value before setting alarm
Maximum PHA	maximum pulse height value before setting alarm
Reference Velocity	velocity of x motor (typically $3\frac{mm}{s}$)
Refilling Cycle	number of rows to execute for refilling cycle to complete
X Origin	motor reading (mm) at x origin
X Indicator Reading at Origin	digital dial indicator reading (mm) at x origin
Starting Dial Y	dial indicator reading of the first ablation row
Y Origin	motor reading (mm) at y origin
Y Dial Reading at Origin	dial indicator reading (mm) at y origin
Focal Position	position of z motor, sets beam spot (typically 4.9 mm)
Raster File	seq file to read xyz values from
Pulse Height File	ile to read in pulse height values from

Table A.2: User switches to set before running Ablation Station.vi software (True = bright green, False = dark green).

Field Name	Description
Set Pulse Height	Reset the pulse height reference value
Set Start Dial Y	Set y dial indicator value to begin
Read in Pulse Heights	Read in pulse height values from file
Refill	Begin the automated refilling sequence
Force Delta Y	Hard set the delta y value after each row
Set Done	For debugging, set the GPIO "DONE" pin to HI
Record Pulse Data	Save pulse data from ADC to file
Finding Origin	Set when initially trying to set motor origin
Lower Beam Block	Lowers beam block at the beginning of a run
Sparse File	Delta y is set to "Y Step" value
Reverse Seq	If true, motors run from top-to-bottom
Send Email	Sends email to specified users once completed

A.3 Procedures for Creating Raster Files

The thinning of a diamond sample to 20 μm requires the use of the ablation software described in earlier sections. The section below lists all of the steps required to take a virgin diamond target and create a sequence of raster files that will bring it to the desired target shape. In this example, diamond JD70-104 was used.

A.3.1 Creating a Proper Target

The first step in creating a series of raster files to be used in the ablation of the diamond sample JD70-104 was to measure its length, width and thickness. The length and width are measured using a digital vernier caliper and the average thickness was measured at the center-point of the diamond using a sub-micron digital micrometer. The ablate.py must be altered so that these dimensions are properly reflected. In the ablate.py code, the "part_size" variable was set to the lengths of diamond JD70-104 (it is assumed that the diamonds are square). The thickness measured is used to assign values to the two-component array named "thick", where the first parameter is the average thickness of the virgin diamond and the second parameter is the desired end thickness of the radiator after ablation. The variable "frame_width" defines the amount of material that should be left untouched on the outer edge of the diamond, which is referred to as the "frame". There is a second keep-out-zone in the bottom-left corner of the diamond. This corner is where the diamond will be mounted (via thermal epoxy) to the goniometer in the GlueX beamline and is kept for structural stability. The "dog-ear" is defined by the line $y = mx + b$, where m is the slope with value of negative one, and b is the y intercept set by the variable "dogear_intercept".

Each diamond has its own unique shape and surface profile that must be taken into consideration when constructing raster files. If the top and bottom surfaces of the diamond sample are not parallel to each other, a uniform raster pattern will in fact cut a hole in a corner of the thin membrane. To correct for this, each corner of the diamond is measured

using a sub-micron digital micrometer. The back surface of the diamond is then imaged using the Zygo interferometer. The image is then flipped along the y and z axis so that its orientation is such that the viewer is looking down through the diamond to the bottom surface. The resulting two dimensional histogram (a Map2D object in the language of ablator.C) is then shifted in z so that the height of each corner corresponds to the value measured by the micrometer subtracted from a constant (typically 300 μm). An example of these images is shown below for diamond JD70-104 in Figure A.2 and is referred to as the Map2D "back surface".

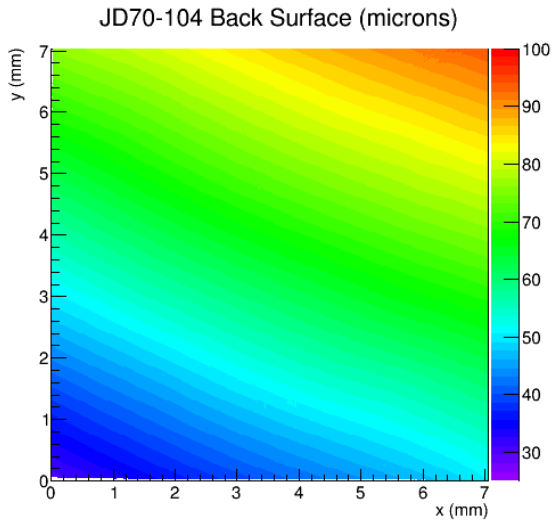

Figure A.2: Zygo image of diamond JD70-104 back surface. The z axis scale is in μm.

The back surface of JD70-104 clearly shows surface variations over a range of over 70 μm. If a uniform raster pattern were applied to this diamond, the region in the lower left corner would reach zero before the desired average thickness of 20 μm was reached. Calling the ablate::make() method in the ablate.py module creates two models of the diamond radiator that are useful. The first is called the "virgin" Map2D which has the dimensions supplied by the user and a uniform thickness (and perfectly flat top surface). The second is called the "target" and is an ideal representation of what the diamond radiator should look like as a final product. The outer frame has the same height (z value in μm) as the constant from which the four corner measurements were subtracted (typically 300 μm). The target has a

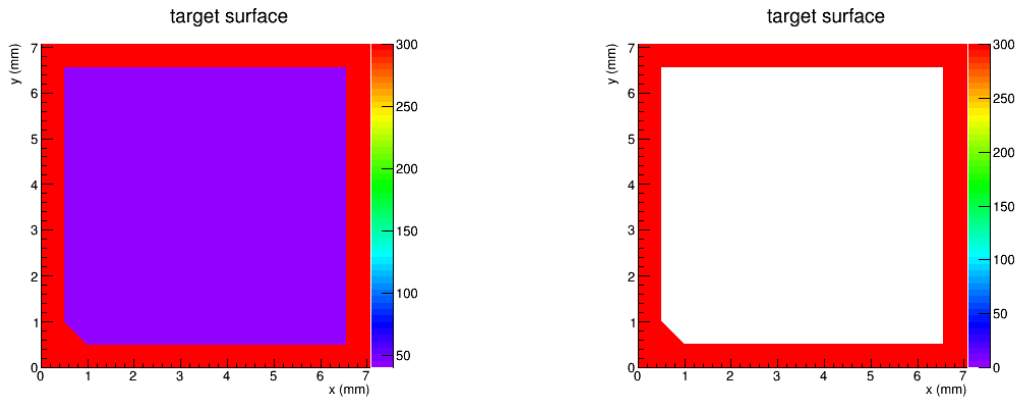

(a) A.3a (b) A.3b

Figure A.3: Target generated by ablate::make() method before and after applying the ZeroSuppress() method.

thin interior region with the predefined geometry and uniform thickness, and perfectly sharp walls at the interface between the two regions. It is up to the user to create a more realistic representation using this target model as a starting point.

The first step in this process removing the unrealistic thin interior automatically generated by the ablate.py software. This is accomplished through the use of ROOT's ZeroSuppress() method which changes the contents of any bin that is less than the ZeroSuppress argument. Below is an example of the python command line and the code that should be executed to perform the task detailed above.

>>>targ.ZeroSuppress(20)

Figure A.3 shows an example of the target after the above method was executed. The final goal is to create a target with a uniform outer frame and thin interior region which has the surface variations of the Map2D shown in Figure A.2. The following command structure removes the frame outline from the back-surface Map2D, shifts it upward by the desired final thickness of the interior region (20 μm) and then copies the result into the empty interior region of the target Map2D.

>>>back.Mask(target,-1)

>>>back.Shift(0,0,20)

>>>target.Fill(back)

The resulting target shown in Fig. A.4a has a 0.5 mm wide outer frame of 300 μm thickness, a dog ear which intercepts the y axis at y = 1.5 mm and a thin interior region which when subtracted from the original back surface Map2D shown in Figure A.2, results in a flat membrane 20 μm thick.

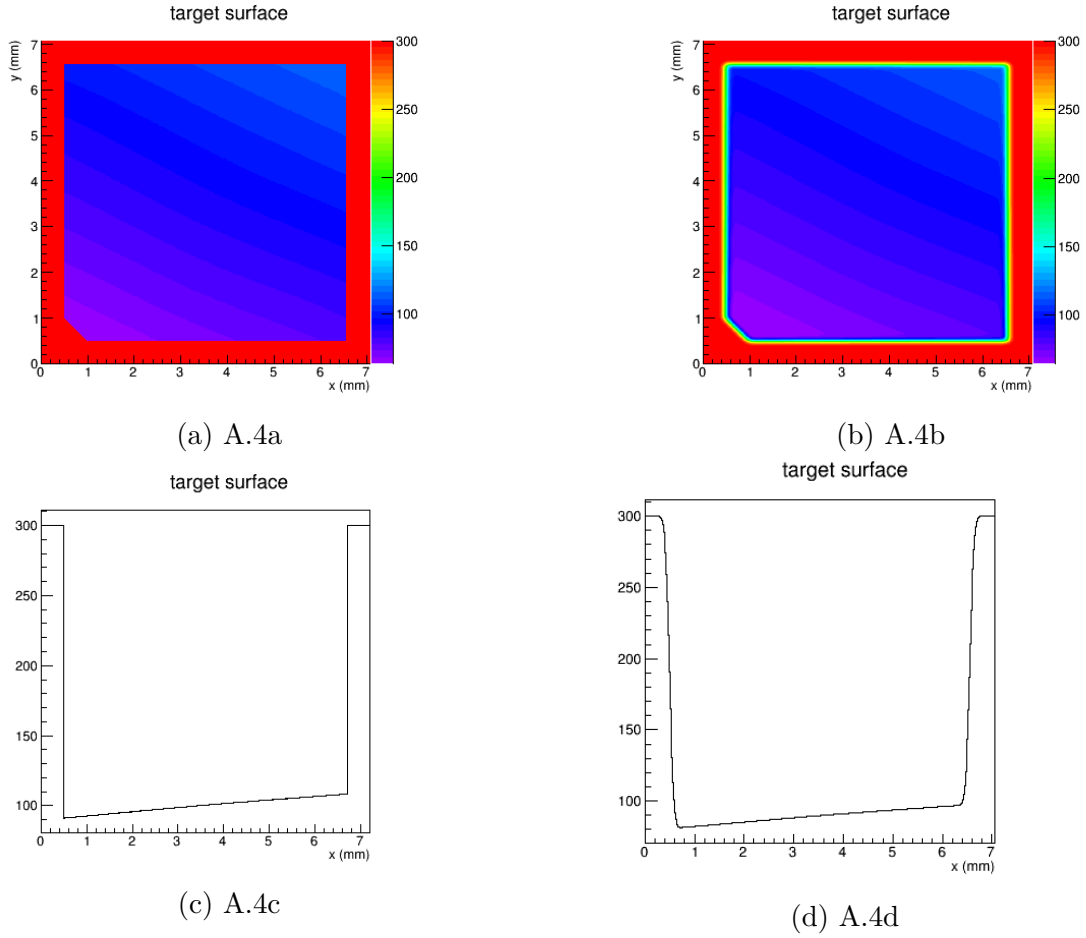

(a) A.4a

(b) A.4b

(c) A.4c

(d) A.4d

Figure A.4: Panel a (upper left) shows the target model created in the python module ablate.py. Panel b (upper right) shows the same model after a smoothing algorithm was applied. Panel c (bottom left) shows a cross section through the mid point of the y axis of the target shown in panel a. Panel d (lower right) shows a cross section through the mid point of the y axis of the smoothed target shown in panel b.

This is still not representative of what the ablation facility is capable of producing. The sharp transitions from the outer frame to the thin interior region require smoothing. This is done by the use of the ablator::smooth() method which convolutes the target map with a two dimensional Gaussian smearing function modeled after the laser's beam spot. An example

of its implementation in the python command line is shown below which, when executed, creates an object "ts" that is the smoothed version of target.

>>>ts = ablate.abl.smooth(target)

Creating an appropriate target Map2D to represent the final diamond radiator is the most crucial step in the production of the raster files. This target will be referenced throughout the lifetime of the diamond sample as new programs are made. It should be saved in a ROOT file and carefully scrutinized over before using.

A.3.2 Creating a Discretized, Detrenched, Ablation Program

The target Map2D created in the previous section can now be used to create what is called a "program" in the ablate.py software. To accomplish this, the ablate::mill() method is called which uses the convolution method described in the earlier section to solve for a series of laser pulses that will transform the virgin diamond to the final target. As mentioned earlier, the energy of the initial pulses in a long train have higher energy and must be accounted for using the ablator::detrench() method. Finally, the program-detrenched Map2D must then be discretized using the ablate::discretize() method to account for the real-world constraint that the laser can only fire a discrete number of pulses. The initial ablate::mill() method solves the convolution exactly, which includes non-integer numbers of laser pulses. The ablate::discretize algorithm replaces floating point number of pulses in the program map with integer numbers which minimizes the distortion of the final diamond surface relative to the target Map2D. The creation of a program-detrenched-integer Map2D (pdi) is achieved through the following sequence of commands.

>>>p = ablate.abl.mill(virgin, target)

>>>pd = ablate.abl.detrench(p)

>>>pdi = ablate.abl.discretize(pd)

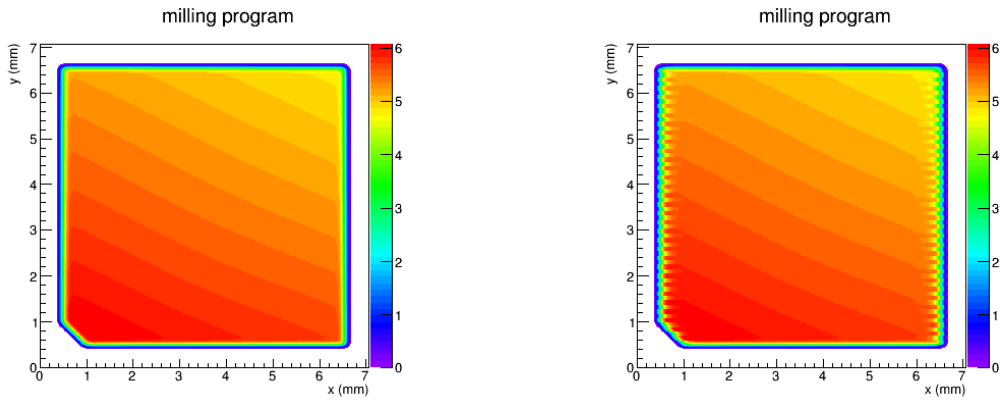

(a) A.5a (b) A.5b

Figure A.5: Panel a shows the raster program (number of pulses per raster spot) created after after the ablate.abl.mill method is invoked. Panel b shows the raster program after ablate.abl.detrench is applied to the Map2D shown in panel a. Notice the irregular patter along the left and right edges that results from the detrench algorithm.

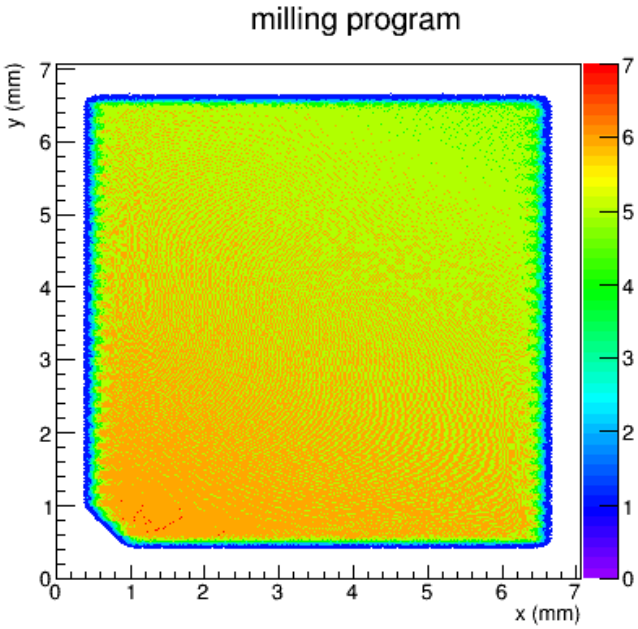

Figure A.6: Program-Detrench-Integer created using the ablator::discretize() method applied to the program-detrench Map2D. Each pixel represents a raster position on the face of the diamond, to which a variable number of laser pulses is applied.

The final step in turning the program-detrenched-integer shown in Figure A.6 into usable raster files is to call the ablator::rasterize() method.

>>>ablate.abl.rasterize(pdi, “JD70-104”)

This transforms the program shown above into a series of laser pulses laid out in rows separated by 10 μm. The program is split into many raster files with the "JD70-104" file name, each one of which has either zero or one pulse per raster position. After all of the program files have been fed to pulser.c and executed by Ablation Station.vi, the virgin target diamond will be cut into a shape closely resembling the target Map2D.

BIBLIOGRAPHY

[1] R.N. Cahn and G. Goldhaber. The experimental foundations of particle physics. 1989.

[2] Gunnar S. Bali, Bram Bolder, Norbert Eicker, Thomas Lippert, Boris Orth, Peer Ueberholz, Klaus Schilling, and Thorsten Struckmann. Static potentials and glueball masses from qcd simulations with wilson sea quarks. *Phys. Rev. D*, 62:054503, Jul 2000.

[3] Jozef J. Dudek, Robert G. Edwards, Michael J. Peardon, David G. Richards, and Christopher E. Thomas. Highly excited and exotic meson spectrum from dynamical lattice qcd. *Phys. Rev. Lett.*, 103:262001, Dec 2009.

[4] Y. Nambu. Univ. of chicago report no. 70-70. 1970.

[5] Bernard et al. Exotic mesons in quenched lattice qcd. *Phys. Rev. D*, 56:7039–7051, Dec 1997.

[6] N. Isgur. *Phys. Rev. Lett.*, 54, 1985.

[7] P. Lacock et al. *Phys. Lett. B*, 401, 1997.

[8] Richard T. Jones. Intense beams of polarized and nearly monochromatic photons from coherent bremsstrahlung. Talk given at the Summer 1997 Hall D Workshop, 1997.

[9] GlueX Collaboration. *Hall D GlueX Technical Construction Report*, May 2015. Technical note GlueX-doc-2511-v4 available at `http://argus.phys.uregina.ca/gluex/DocDB/0025/002511/004/tcr.pdf`.

[10] M. Dugger, B. G. Ritchie, N. Sparks, K. Moriya, R. J. Tucker, R. J. Lee, B. N. Thorpe, T. Hodges, F. J. Barbosa, N. Sandoval, and R. T. Jones. Design and construction of a high-energy photon polarimeter. *ArXiv e-prints*, March 2017.

[11] L. Pentchev et al. Studies with cathode drift chambers for the gluex experiment at jefferson lab. *Nuclear Instruments and Methods in Physics Research Section A: Accelerators, Spectrometers, Detectors and Associated Equipment*, 845:281 – 284, 2017. Proceedings of the Vienna Conference on Instrumentation 2016.

[12] Elton S. Smith. Development of silicon photomultipliers and their applications to gluex calorimetry. *AIP Conference Proceedings*, 1753(1):070006, 2016.

[13] Berdnikov et al. Use of cluster counting technique for particle identification in a drift chamber with the cathode strip readout. *Instruments and Experimental Techniques*, 58(4):473–477, 2015.

[14] J. Stevens et al. The gluex dirc project. *Journal of Instrumentation*, 11(07):C07010, 2016.

[15] A.P. Malshe et al. A review of techniques for polishing and planarizing chemicallyvapor-deposited (cvd) diamond lms and substrates. *Diamond and Related Materials*, 8(7):1198:1213, 1998.

[16] et al. G. Yang. Rocking curve imaging for diamond radiator crystal selection. *Diam. Relat. Mater.*, page 4, 2010.

[17] John Smedley, Jen Bohon, Qiong Wu, and Triveni Rao. Laser patterning of diamond. part i. characterization of surface morphology. *Journal of Applied Physics*, 105(12):123107, 2009.

[18] Ralph Delmdahl and Rainer Ptzel. Excimer laser technology trends. *Journal of Physics D: Applied Physics*, 47(3):034004, 2014.

[19] Professor Dr. Gerd Marowsky Dr. Dirk Basting. *Excimer Laser Technology*, chapter Principles of Excimer Lasers. Springer, 2005.

[20] `https://github.com/WiringPi`.

[21] Ken Livingston. The stonehenge technique. a method for aligning coherent bremsstrahlung radiators. *Nuclear Instruments and Methods in Physics Research Section A: Accelerators, Spectrometers, Detectors and Associated Equipment*, 603(3):205 – 213, 2009.

[22] GlueX Collaboration et al. Measurement of the beam asymmetry Σ for π^0 and η photoproduction on the proton at $E\_\gamma = 9$ GeV. *ArXiv e-prints*, January 2017.

[23] K. Schilling, P. Seyboth, and Guenter E. Wolf. On the Analysis of Vector Meson Production by Polarized Photons. *Nucl. Phys.*, B15:397–412, 1970. [Erratum: Nucl. Phys.B18,332(1970)].

[24] Curtis A. Meyer. A review of asymmetry measurements in vector meson photoproduction experiments. GlueX-doc-3076, 2016.